

**POLITECNICO DI MILANO**

**Scuola di Ingegneria Industriale e dell'Informazione**

**Corso di Laurea in Ingegneria Chimica**



**New frontiers of cyclodextrin-based nanosponges:  
from synthesis to physical investigation**

**Relatore: Prof. Carlo PUNTA, Politecnico di Milano**

**Correlatore: Ing. Lucio MELONE, Politecnico di Milano**

**Tesi di Laurea Magistrale di:**

**Fabio Toraldo**

**Matricola 787371**

**Anno Accademico 2013 – 2014**



<b>Chapter 1 – Cyclodextrin based nanosponges</b> .....	20
1.1. Introduction.....	20
1.2. Application of nanosponges .....	21
<u>1.2.1. Nanosponges for drug delivery</u> .....	21
<u>1.2.2. Nanosponges as carriers for biocatalysts and in the delivery and release of enzymes, proteins, vaccines and antibodies</u> .....	22
<u>1.2.3. Other applications of Nanosponges</u> .....	23
1.3. Methods of analysis of cyclodextrin-based nanosponges .....	23
<b>Chapter 2 - Cyclodextrins</b> .....	25
2.1. Cyclodextrins .....	25
2.2. History .....	25
<u>2.2.1. The discovery period, 1891 to the mids 1930s</u> .....	25
<u>2.2.2. The exploratory period, mid 1930s to 1970</u> .....	26
<u>2.2.3. The widespread application and production period, 1970 to present</u> .....	27
2.3. Properties of cyclodextrins.....	28
<u>2.3.1. Chemical structure of CyDs</u> .....	28
<u>2.3.2. CD inclusion complex formation</u> .....	29
<u>2.3.3. Safety and biocompatibility of cyclodextrin</u> .....	30
<u>2.3.4. Regulatory status of cyclodextrins</u> .....	30
2.4. NMR studies of cyclodextrins.....	31
<u>2.4.1. <sup>1</sup>H NMR Spectra of Cyclodextrins</u> .....	33
<b>Chapter 3 – Rheological analysis of CDNS</b> .....	34
3.1. Synthesis process of CDNS.....	34
<u>3.1.2. Synthesis of cyclodextrin-based nanosponges</u> .....	37

<b>3.2. Swelling</b> .....	39
<b>3.3. Direct evidence of gel-sol transition in cyclodextrin-based hydrogel as revealed by FTIR-ATR spectroscopy</b> .....	40
<u>3.3.1. Materials and methods</u> .....	41
<u>3.3.2. B FTIR-ATR measurements</u> .....	42
<u>3.3.3. Results and discussion</u> .....	42
<u>3.3.4. Conclusions</u> .....	50
<b>3.4. Glass-like dynamics of new cross-linked polymeric systems: Behavior of the Boson peak</b> ....	52
<u>3.4.1. Materials and methods</u> .....	53
<u>3.4.2. Raman scattering measurements</u> .....	53
<u>3.4.3. Results</u> .....	54
<u>3.4.4. Discussion</u> .....	56
<u>3.4.5. Conclusions</u> .....	60
<b>Chapter 4 – Paramagnetic Cyclodextrin based nanosponges</b> .....	61
<b>4.1. Aims of the chapter</b> .....	61
<b>4.2. Radical TEMPO</b> .....	62
<b>4.3. Cathode Material for rechargeable lithium batteries</b> .....	64
<u>4.3.1. Requirements for electrochemical performance</u> .....	64
<u>4.3.2. Nitroxy radical as cathode material</u> .....	66
<b>4.4. MR contrast agent</b> .....	68
<u>4.4.1. Magnetic Resonance Imaging</u> .....	68
<u>4.4.2. Nitroxyl radicals as MR/EPR contrast agent</u> .....	69
<b>4.5. ROS Scavenger</b> .....	74
<u>4.5.1. Reactive Oxygen Species</u> .....	74
<u>4.5.2. Cyclodextrins as anti-oxidant molecules</u> .....	76

<b>4.6. Synthesis of fully organic paramagnetic CD (pmCD) bearing persistent nitroxyl radical</b> .....	77
<b>4.7. Synthesis of CDNS through TEMPO anhydride</b> .....	78
<u>4.7.1. TEMPO anhydride</u> .....	79
<u>4.7.1.1. Synthesis TEMPO anhydride</u> .....	80
<u>4.7.2. Synthesis random grafted TEMPO cyclodextrin based nanosponge</u> .....	80
<b>4.8. Synthesis paramagnetic cyclodextrin through click reaction</b> .....	81
<u>4.8.1. First approach: Monofunctionalization of CD with nitroxyl radical</u> .....	82
<u>4.8.1.1. First approach: Mono 6 - (p-tolysulfonyl) -6-deoxy <math>\beta</math>Cyclodextrins CD1</u> .....	83
<u>4.8.1.1.1. Synthesis Mono 6 – (p-tolysulfonyl) -6-deoxy <math>\beta</math>Cyclodextrins</u> .....	84
<u>4.8.1.2. First approach: Mono 6-azido-6-deoxy- <math>\beta</math>Cyclodextrins CD2</u> .....	86
<u>4.8.1.2.1. Synthesis Mono 6-azido-6-deoxy- <math>\beta</math>Cyclodextrins</u> .....	86
<u>4.8.1.3. First approach: Propargil – TEMPO</u> .....	88
<u>4.8.1.3.1. Synthesis Propargil-Tempo</u> .....	88
<u>4.8.1.4. First approach: Mono-6-Tempo-6-Deoxy <math>\beta</math>cyclodextrin CD3</u> .....	89
<u>4.8.1.4.1. Synthesis Mono 6 Tempo 6 deoxy <math>\beta</math>Cyclodextrins</u> .....	90
<u>4.8.2. Mono 6 Tempo 6 deoxy <math>\beta</math>Cyclodextrins – based nanosponges</u> .....	94
<u>4.8.2.1. Synthesis Mono 6 Tempo 6 deoxy <math>\beta</math>Cyclodextrins – based nanosponges with PMA</u> ..	94
<u>4.8.2.2. Synthesis Mono 6 Tempo 6 deoxy <math>\beta</math>Cyclodextrins – based nanosponges with EDTA</u> ..	95
<u>4.8.3. Second approach: Hepta functionalization of <math>\beta</math>CD with nitroxyl radical</u> .....	96
<u>4.8.3.1. Second approach: Hepta 6 (iodo) 6 deoxy <math>\beta</math> cyclodextrin CD4</u> .....	97
<u>4.8.3.1.1. Synthesis Hepta 6 deoxy 6 iodo <math>\beta</math>Cyclodextrins</u> .....	98
<u>4.8.3.2. Second approach: Hepta 6 (azido) 6 deoxy <math>\beta</math> cyclodextrin CD5</u> .....	100
<u>4.8.3.2.1. Synthesis of Hepta 6 (azido) 6 deoxy <math>\beta</math> cyclodextrin</u> .....	101
<u>4.8.3.3. Second approach: Hepta 6 (TEMPO) 6 deoxy <math>\beta</math> cyclodextrin CD6</u> .....	103
<u>4.8.3.3.1. Synthesis of Hepta 6 (TEMPO) 6 deoxy <math>\beta</math> cyclodextrin</u> .....	103
<u>4.8.4. Synthesis Hepta 6 Tempo 6 deoxy <math>\beta</math>Cyclodextrins – based nanosponges with PMA</u> .....	106

<b>4.9. Paramagnetic analysis</b> .....	107
<u>4.9.1. Magnetization for the spin 1/2 system</u> .....	108
<u>4.9.2. Brillouin function</u> .....	110
<u>4.9.3. Calculation of M vs B/T</u> .....	112
<u>4.9.4. Random grafted TEMPO cyclodextrin based nanosponge</u> .....	114
<u>4.9.5. Magnetic measurements of Mono – 6 – (TEMPO) – 6 (deoxy) – <math>\beta</math> cyclodextrin</u> .....	116
<u>4.9.6. Magnetic measurements of Hepta – 6 – (TEMPO) – 6 (deoxy) – <math>\beta</math> cyclodextrin</u> .....	118
<b>4.10. EPR Measurement</b> .....	120
<u>4.10.1. Random grafted TEMPO cyclodextrin based nanosponge</u> .....	121
<u>4.10.2. Mono 6 Tempo 6 deoxy <math>\beta</math>Cyclodextrins – based nanosponges with PMA</u> .....	121
<u>4.10.3. Mono 6 Tempo 6 deoxy <math>\beta</math>Cyclodextrins – based nanosponges with EDTA</u> .....	122
<u>4.10.4. Hepta – 6 – (TEMPO) – 6 – deoxy <math>\beta</math>Cyclodextrins</u> .....	123
<b>Chapter 5 - Conclusions</b> .....	124
Bibliography.....	126

# Image index

Figure 1: Molecular structure of cyclodextrin carbonate nanosponges .....	24
Figure 2: Chemical structure of $\alpha$ -, $\beta$ - and $\gamma$ -CD.....	25
Figure 3: Morphology of CDs .....	28
Figure 4: Schematic representation of CD inclusion complex formation .....	29
Figure 5: $^1\text{H}$ NMR spectra (400 MHz) of CD at 298 K: (a) in $\text{D}_2\text{O}$ and (b) in $\text{DMSO-d}_6$ .....	33
Figura 6: Hydrolysis of generic anhydride .....	34
Figura 7: Regeneration of generic anhydride .....	35
Figure 8: Reaction anhydride - alcohol .....	36
Figure 9: (a) Scheme of formation of ester groups between two adjacent cyclodextrins. (b) Model of the covalent network of b-CDPMA1n nanosponges. ....	37
Figure 10: Schematic representation of the network of non-covalent interactions among different nanosponge molecules in the gel phase.....	38
Figure 11: Photographs of samples of $\beta$ -CDEDTA14 hydrogel obtained as increasing the weight ratios $\text{H}_2\text{O}/\beta$ -CDEDTA14. Note: a suitable dye (Rhodamine B) was added to the water solvent in order to better visualize the phase changes of the system. The hydration level is reported above each vial. ....	43
Figure 12: Experimental FTIR-ATR spectra in the O-H stretching region for $\beta$ -CDEDTA14 (a) and $\beta$ -CDEDTA110 (b) hydrogels at $h = 2.7$ (black closed squares) and $h = 16.4$ (red open circles). (c) Experimental FTIRATR spectra in the HOH bending region for $\beta$ -CDEDTA18 hydrogel at $h = 2.7$ (black closed squares), $h = 11.8$ (red open circles) and $h = 20.2$ (green closed up triangles). ....	43
Figure 13: Examples of fitting results of O-H stretching profile for $\beta$ -CDEDTA16 hydrogel at $h = 4.3$ (a) and $\beta$ -CDEDTA18 hydrogel at $h=20.2$ (b). The experimental data (empty squares) are reported	

together with the best-fit (grey line), the deconvolution components (indicated in the individual subpanels) and the residual (blue lines) .....	45
Figure 14: Percentage intensities $I_i$ of the different spectral contributions to the O-H stretching band as a function of the hydration level $h$ for (a) $\beta$ -CDEDTA14, (b) $\beta$ -CDEDTA16, (c) $\beta$ -CDEDTA18, and (d) $\beta$ -CDEDTA110 hydrogel. $I_1$ : closed squares, $I_2$ : closed circle, $I_3$ : closed up triangles; , $I_4$ : closed down triangles. For each plot, the inset reports the evolution of the corresponding peak wavenumbers: $\omega_1$ : open squares, $\omega_2$ : open circles, $\omega_3$ : open up triangles, $\omega_4$ : open down triangles.....	46
Figure 15: Percentage intensities $I_1+I_2$ (closed squares) and $I_3+I_4$ (open circles) of the spectral contributions to the O-H stretching band, as a function of the hydration $h$ , for (a) $\beta$ -CDEDTA14, (b) $\beta$ -CDEDTA16, (c) $\beta$ -CDEDTA18, and (d) $\beta$ -CDEDTA110 hydrogel. The vertical lines indicates the value.....	47
Figure 16: Photographs of different phase behaviour for $\beta$ -CDEDTA1n hydrogels as increasing the level of hydration $h$ . Note: a suitable dye (Rhodamine B) was added to the water solvent in order to better visualize the phase changes of the system.....	48
Figure 17: Crossover hydration level $h_{cross}$ estimated for nanosponges hydrogels as a function of the parameter $n$ .....	48
Figure 18: Percentage intensities $I_1+I_2$ reported as a function of the molar ratio $n$ for different values of hydrations $h$ , as indicated in the panel. ....	50
Figure 19: Cross-polarized (HV) Raman intensity $I_{Raman HV}$ of $\alpha$ -CDEDTA110 nanosponge in the wave number region between $+200\text{ cm}^{-1}$ and $-200\text{ cm}^{-1}$ . ....	54
Figure 20: Reduced Raman spectra of $\alpha$ -CDEDTA1n nanosponges ( $n = 2, 6, 10$ ) in the energy range $0-200\text{ cm}^{-1}$ ; the arrow indicates the evolution of the BP peak frequency. (Inset) Typical example of the best fitting results for $\alpha$ -CDEDTA16: the experimental data (red circles) are shown together with the total fitting curve and the different components (QE, quasi-elastic; BP, boson peak). ....	55
Figure 21: Reduced Raman spectra of $\alpha$ -CDEDTA1n nanosponges ( $n = 2, 6, 10$ ) after subtraction of QE contribution in the energy range $0-200\text{ cm}^{-1}$ .....	56



Figure 22: Reduced Raman spectra of $\alpha$ -CDEDTA1n nanosponges (n = 2, 6, 10) after subtraction of QE contribution in the energy range 0–200 cm <sup>-1</sup> .....	57
Figure 23: Evolution of $\omega$ BP as a function of the molar ratio n for different types of EDTA nanosponges: $\alpha$ -CDEDTA1n (blue left triangles) and $\gamma$ -CDEDTA1n (pink hexagons).....	59
Figure 24: Schematic picture representing the effect of increasing of the parameter n on the structural properties of CDNS polymer network. ....	59
Figure 25: Redox reaction of nitroxide radical.....	63
Figure 26: The redox voltage and specific capacity of typical inorganic and organic electrode materials for rechargeable lithium batteries. The structure of some organic can be found in Table 9 .....	65
Figure 27: PTMA: poly(2,2,6,6-tetramethylpiperidine-1-oxyl-4-yl methacrylate).....	66
Figure 28: a) Typical charge/discharge curves and (b) cycling and rate performance of PTMA as the cathode material for a rechargeable lithium battery. Copyright © 2006 Elsevier. (c) The electron transfer process in a radical polymer electrode. ....	67
Figure 29: Comparison of pharmacokinetic/redox images (slice 1) of three nitroxide contrast agents by SPGR MRI. Sixty serial images of Tempol (A), 3CP (3-carbamoyl-2,2,5,5-tetramethylpyrrolidine-1-Oxyl) (B), and 3CxP(3-carboxy-2,2,5,5,5-tetramethylpyrrolidine-1-oxyl) (C) were obtained during 20 minutes of continuous imaging. Slice 1, normal and tumor tissue area. Enhanced image intensity (%) against preinjection image by T1-weighted MRI (green). D, for T2 mapping, spin echo images were obtained using a MSME sequence with eight echo trains and 15-ms echo times. ....	70
Figure 30: Lomustine (CCNU) and its nitroxyl labelled analogue (SLENU). ....	71
Figure 31: MRI signal dynamic of SLENU in the brain after intravenous injection in mice .....	72
Figure 32: Pulsed EPR imaging of nitroxide in mice. (A) The first pulsed EPR image of nitroxide distribution in mouse. (B) Pulsed EPR image of Oxo63 injected into the same mouse after N-PDT signal disappeared. ....	73

Figure 33: Electron structures of common reactive oxygen species. Each structure is provided with its name and.....	74
Figure 34: The glucopyranose ring.....	77
Figure 35: Synthesis scheme for CDNS through TEMPO anhydride .....	78
Figure 36: Synthesis scheme for functionalization of CD through ClcI Reaction .....	81
Figure 37: Synthesis scheme for Monofunctionalized cyclodextrin-based nanosponges.....	82
Figure 38: Tosylation of $\beta$ CD .....	84
Figure 39: ESI-Mass of Mono 6 – (p-tolysulfonyl) -6-deoxy $\beta$ Cyclodextrins .....	85
Figure 40: NMR spectrum of Mono 6 – (p-tolysulfonyl) -6-deoxy $\beta$ Cyclodextrins.....	85
Figure 41: NMR spectrum of Mono 6 – (p-tolysulfonyl) -6-deoxy $\beta$ Cyclodextrins treated with D <sub>2</sub> O.....	86
Figure 42: Substitution of tosyl group by azide group.....	86
Figure 43: ESI-Mass of Mono 6 – (azide) 6 – deoxy $\beta$ cyclodextrin .....	87
Figure 44: IR spectrum of Mono 6 – (azide) 6 – deoxy $\beta$ cyclodextrin .....	88
Figure 45: Synthesis of Propargil - TEMPO .....	88
Figure 46: NMR spectrum of Propargil – TEMPO .....	89
Figure 47: Mechanism of Huisgen Cycloaddition with Cu(I).....	90
Figure 48: Click reaction on Mono 6 – (azide) 6 – deoxy $\beta$ cyclodextrin .....	90
Figure 49: ESI Mass of Mono 6 – (TEMPO) 6 – deoxy $\beta$ cyclodextrin .....	92
Figure 50: NMR spectrum of Mono 6 – (TEMPO) 6 – deoxy $\beta$ cyclodextrin.....	92
Figure 51: NMR spectrum of Mono 6 – (TEMPO) 6 – deoxy $\beta$ cyclodextrin treated with D <sub>2</sub> O .....	93
Figure 52: NMR spectrum of Mono 6 – (TEMPO) 6 – deoxy $\beta$ cyclodextrin treated with D <sub>2</sub> O and phenylhydrazine.....	93
Figure 53: IR spectrum of Mono 6 – (TEMPO) 6 – deoxy $\beta$ cyclodextrin.....	94

Figura 54: Synthesis scheme of Heptafunctionalized cyclodextrin - based nanosponges .....	96
Figure 55: Simmetric Iodination of $\beta$ -CD.....	98
Figure 56: ESI Mass of Hepta 6 deoxy 6 iodo $\beta$ Cyclodextrins .....	99
Figure 57: NMR spectrum of Hepta 6 deoxy 6 iodo $\beta$ Cyclodextrins.....	100
Figure 58: NMR spectrum of Hepta 6 deoxy 6 iodo $\beta$ Cyclodextrins treated with $D_2O$ .....	100
Figure 59: Substitution of iodine groups by azide groups .....	101
Figure 60: ESI Mass of Hepta 6 – (azide) 6 – deoxy $\beta$ cyclodextrin.....	101
Figure 61: NMR spectrum of Hepta 6 – (azide) 6 – deoxy $\beta$ cyclodextrin .....	102
Figure 62: IR spectrum of Hepta 6 – (azide) 6 – deoxy $\beta$ cyclodextrin .....	102
Figure 63: Click reaction on Hepta 6 – (azide) 6 – deoxy $\beta$ cyclodextrin .....	103
Figure 64: ESI Mass of Hepta 6 – (TEMPO) 6 – deoxy $\beta$ cyclodextrin .....	104
Figure 65: NMR spectrum of Hepta 6 – (TEMPO) 6 – deoxy $\beta$ cyclodextrin.....	104
Figure 66: NMR spectrum of Hepta 6 – (TEMPO) 6 – deoxy $\beta$ cyclodextrin treated with phenylhydrazine.....	105
Figure 67: NMR spectrum of Hepta 6 – (TEMPO) 6 – deoxy $\beta$ cyclodextrin treated with phenylhydrazine and $D_2O$ .....	105
Figure 68: IR spectrum of NMR Hepta 6 – (TEMPO) 6 – deoxy $\beta$ cyclodextrin.....	106
Figure 69: Zeeman splitting of the degenerate state under the application of magnetic field B ...	108
Figure 70: Graphic Magnetization Vs B/T of random grafted TEMPO cyclodextrin based nanosponge.....	114
Figure 71: Curie-Weiss' law of random grafted TEMPO cyclodextrin based nanosponge .....	115
Figure 72: Graphic Magnetization*Temperature Vs Temperature of random grafted TEMPO cyclodextrin based nanosponge .....	115

Figure 73: Graphic Magnetization Vs B/T of Mono 6 – (TEMPO) 6 – deoxy $\beta$ cyclodextrin .....	116
Figure 74: Curie-Weiss' curve of Mono 6 – (TEMPO) 6 – deoxy $\beta$ cyclodextrin .....	117
Figure 75: Graphic Magnetization Vs B/T of Heptha 6 – (TEMPO) 6 – deoxy $\beta$ cyclodextrin.....	118
Figure 76: Graphic Magnetization Vs B of Heptha 6 – (TEMPO) 6 – deoxy $\beta$ cyclodextrin .....	119
Figure 77: Curie-Weiss' law of Hepta 6 – (TEMPO) 6 – deoxy $\beta$ cyclodextrin .....	119
Figure 78: EPR spectrum of random grafted TEMPO cyclodextrin based nanosponge .....	121
Figure 79: EPR spectrum of paramagnetic cyclodextrin based nanosponge with PMA as CL.....	122

# Table Index

Table 1: Examples of applications of nanosponges .....	21
Table 2: Characteristic of $\alpha$ -, $\beta$ - and $\delta$ -CD.....	28
Tabella 3: Regulary status of the natural cyclodextrin and HP CD .....	30
Tabella 4: The structure and redox mechanism of various type of organic catode materials .....	64

# Abbreviations

$\alpha$ -CD	alfa - cyclodextrin
$\beta$ -CD	beta - cyclodextrin
$\gamma$ -CD	gamma - cyclodextrin
$\delta$ -CD	delta - cyclodextrin
$\epsilon$ -CD	epsi - cyclodextrin
z-CD	zeta - cyclodextrin
HP $\beta$ CD	Hydroxil Propil beta - cyclodextrin
SBE $\beta$ CD	Sulfobutyl Ether beta - cyclodextrin
CD	cyclodextrin
CDNS	cyclodextrin-based nanosponges
CL	crosslinker
PMCD	Paramagnetic cyclodextrins
PMCDNS	Paramagnetic cyclodextrins based nanosponges
MCF7	Michigan Cancer Foundation-7
HT-29	Human Caucasian colon adenocarcinoma
HCPC-I	Human Cardiac Progenitor Cells
DNA	Deoxyribonucleic acid
FTIR-ATR	Fourier Transform Infrared- Attenuated Total Reflectance

NMR	Nuclear Magnetic Resonance
CGTase	Cyclodextrin glucanotransferase
MW	Molecular Weight
GRAS	Generally Regarded As Safe
FDA	Food and Drug Administration
USP	United States Pharmacopoeia
NF	National Formulary
Ph. Eur.	European Pharmacopoeia
JPC	Japanese Pharmaceutical Codex
UV	Ultraviolet
Cn	Carbon at position n of the glucopyranose ring
DMSO	Dimethyl sulfoxide
Me	Methyl
Et <sub>3</sub> N	Triethylamine
CaH	Calcium hydride
PMA	Piromellitic Anhydride
EDTA	Anhydride of Ethylenediaminetetraacetic acid
BFA	Bi Phenol Anhydride
Py	Pyridine
DTGS	Deuterated triglycene sulphate
h	hydration level
CCD	Charge-Coupled Device

HV	High Voltage
NA	Numerical Aperture
QE	Quasi elastic
BP	Boson Peak
IRaman	Raman Intensity
IRed	Reduced Raman Intensity
IQe	Quasi Elastic Intensity



## Abstract

Cyclodextrin-based nanosponges (CDNS) are a versatile class of cross-linked polymers able to generate hydrogels. CDNS are prepared by polycondensation between cyclodextrins (CDs) and suitable cross-linkers. The reaction leads to the formation of a three dimensional network, showing both hydrophilic and hydrophobic nano-sized cavities where different species can be encapsulated and selectively released. The protocol of synthesis for these materials is still incomplete due to random distribution between CD and cross-linker and to the difficulty to standardize the reaction process. For this reason, the first part of my research focused on the study and the optimization of the synthesis of CDNS in order to define once at all the ideal operative conditions. The new materials were in-deep investigated and the results were published into two papers: "Direct evidence of gel-sol transition in cyclodextrin-based hydrogel as revealed by FTIR-ATR spectroscopy" (*Soft Matter* **2014**, *10*, 2320-2326) and "Glass-like dynamics of new cross-linked polymeric systems: behavior of the Boson peak" (*J. Non-Crys. Sol.* **2014**, DOI 10.1016/j.jnoncrysol.2014.01.016).

In the second part of my work I faced the study of paramagnetic CDNS from their synthesis to their characterization. In order to introduce a paramagnetic aspect into CDNS, maintaining the metal-free character of these soft materials, which represents a key aspect for biocompatibility, the CDs were functionalized with a nitroxyl radical (TEMPO) and then reacted with an appropriate crosslinker. The introduction of a paramagnetic feature has different advantages. First, it is possible to obtain an additional characterization of CDNS through Electron Spin Resonance (ESR), which allows to identify paramagnetic moieties as probes and, hence, to define the real cross-linking degree and the structural conformation. Then, it suggests the possibility to follow drug delivery in specific diseased areas via magnetic resonance imaging. Finally, it allows to design an anti-oxidant material: TEMPO is a stable radical and it is able to modulate the level of reactive oxygen species.

# Sommario

Il mio progetto di tesi si è concentrato sulla sintesi e successiva caratterizzazione di nanospugne, precisamente cyclodextrin-based nanosponges (CDNS). Queste CDNS sono sistemi polimerici ottenuti da policondensazione di ciclodestrine e di crosslinker. I crosslinker, spesso di anidridi, fungono da ponte tra le diverse unità di ciclodestrine creando una rete tridimensionale polimerica con interessanti peculiarità. Infatti questi sistemi mostrano nano-cavità sia idrofiliche sia idrofobiche che possono incapsulare, trasportare e rilasciare selettivamente diversi tipi di sostanze organiche e inorganiche .

Lo stato dell'arte nella sintesi e nell'analisi di queste nanospugne presenta ancora delle lacune a causa della casuale distribuzione tra le unità di ciclodestrina e i relativi crosslinker e delle difficoltà nel trovare una standardizzazione efficace nel processo di reazione.

Per questo motivo, la mia ricerca si è primariamente concentrata sullo studio e sull'ottimizzazione della sintesi di queste nanospugne con l'obiettivo di ottenere le migliori condizioni operative analizzando velocità di reazione, valutando lo stato dei reagenti e dei solventi utilizzati, scegliendo il miglior ambiente e work up del prodotto finale.

Questo lavoro preliminare ha permesso di ottenere un'analisi migliore e più dettagliata attraverso il contributo di Marco Lucarini e Paola Franchi dell'Univeristà di Bologna per le misure EPR, di Andrea Mele per l'analisi spettroscopia NMR e il supporto in fase di sintesi, di Fabio Canepa dell'Università di Genova e di Gianrico Lamura del CNR per i dati di SQUID Magnetometry ed infine di Valentina Venuti dell'Università di Messina e Barbara Rossi dell'Università di Trento per le misure FT-IR e RAMAN.

I risultati ottenuti hanno inoltre permesso la pubblicazione di due articoli "Direct evidence of gel-sol transition in cyclodextrin-based hydrogel as revealed by FTIR-ATR spectroscopy" and "Glass-like dynamics of new cross-linked polymeric systems: behavior of the Boson peak".

Ottenute informazioni più complete, successivamente ho affrontato lo studio di nanospugne paramagnetiche passando dalla sintesi alla successiva caratterizzazione. Per implementare il carattere paramagnetico a questi polimeri e lavorare comunque in sistemi completamente organici (metal free), un aspetto chiave per la biocompatibilità, le ciclodestrine sono state

funzionalizzate con uno o più radicali nitrossido (in particolare il radicale TEMPO) e quindi poi fatti reagire con l'appropriato crosslinker per definire nanospugne paramagnetiche.

La stessa modalità di introduzione del radicale nell'unità di ciclodestrina ha richiesto uno studio sul miglior procedimento da seguire in relazione ai risultati desiderati.

L'introduzione di una caratteristica paramagnetica ha diversi scopi. Il primo è quello di permettere un'ulteriore caratterizzazione delle CDNS: infatti l'unità paramagnetica viene usata come sonda attraverso l'uso di uno ESR (Electron Spin Resonance) per definire l'effettivo grado di crosslink e la conformazione strutturale di questi sistemi.

Il secondo obiettivo è quello di sintetizzare dei sistemi organici che permettano di veicolare rapidamente nanoparticelle in specifiche zone malate. Mediante l'applicazione di un campo magnetico blando, il gruppo paramagnetico è attratto e allo stesso modo quindi l'unità di ciclodestrina. Raggiunta l'area desiderata, è possibile rilasciare lo specifico medicinale usando la peculiare caratteristica di inclusione e rilascio propria di queste nanospugne.

Infine, l'ultimo obiettivo è quello di definire un sistema anti-ossidant: infatti il TEMPO è un radicale stabile, in quanto nitrossi radical ciclico protetto, ed è in grado di modulare il livello di ROS (Reactive Oxygen Species) ed intervenire nei fenomeni quali lo stress ossidativo.

# Chapter 1 – Cyclodextrin based nanosponges

## 1.1. Introduction

Recent advances in nanotechnology demonstrate the increased attention that is now being turned to the supramolecular assembly of simple components for therapeutic and diagnostic purposes.

The design of new biomaterials based on nanoscale structural characteristics can be expected to provide many potential applications in the field of nanomedicine.

Cyclodextrin-based nanosponges (CDNS), which are proposed as a new nanosized delivery system, are innovative cross-linked cyclodextrin polymers nanostructured within a three-dimensional network. This type of cyclodextrin polymer can form porous insoluble nanoparticles with a crystalline or amorphous structure and spherical shape or swelling properties. The polarity and dimension of the polymer mesh can be easily tuned by varying the type of cross-linker and degree of cross-linking. Nanosponge functionalization for site-specific targeting can be achieved by conjugating various ligands on their surface. These materials are safe and biodegradable, show negligible toxicity on cell cultures and are well-tolerated after injection in mice. CDNS can form complexes with different types of lipophilic or hydrophilic molecules. The release of the entrapped molecules can be varied by modifying the structure, in order to modulate the release kinetics. The nanosponges could be used to improve the aqueous solubility of poorly water-soluble molecules, protect degradable substances, obtain sustained delivery systems or design innovative drug carriers for nanomedicine. [1-3]

These polymers can be obtained by reacting native cyclodextrins with a cross-linking agent that, after reaction, exerts its own properties and influences the behaviour of the cyclodextrin unit. Although insoluble crosslinked cyclodextrin polymers were first reported a long time ago, the term “cyclodextrin nanosponges” was first used by DeQuan Li and Min Ma [4] in 1998 to indicate  $\beta$ -cyclodextrin units crosslinked with organic diisocyanates. The result was an insoluble network that showed a very high inclusion constant with several organic pollutants. For instance, p-chlorophenol was almost completely removed from waste water even at the parts per billion level. [5] However, no other applications were claimed or proposed.

It was with the recent contribution by Trotta [6] and co-workers and the syntheses of new kinds of CDNS that they revealed their full potential in other fields, particularly as drug carriers.

## 1.2. Application of nanosponges

### 1.2.1. Nanosponges for drug delivery

Because of their nanoporous structure, nanosponge can advantageously carry water insoluble drugs (Biopharmaceutical Classification System class-II drugs). These complexes can be used to increase the dissolution rate, solubility and stability of drugs, to mask unpleasant flavors and to convert liquid substances to solids.  $\beta$ -Cyclodextrin based nanosponges are reported to deliver the drug to the target site three to five times more effectively than direct injection. [7] Drugs which are particularly critical for formulation in terms of their solubility can be successfully delivered by loading into the nanosponges.

The nanosponges are solid in nature and can be formulated as Oral, Parenteral, Topical or Inhalation dosage forms. For the oral administration, the complexes may be dispersed in a matrix of excipients, diluents, lubricants and anticaking agents suitable for the preparation of capsules or tablets [8]. For the parenteral administration the complex may be simply carried in sterile water, saline or other aqueous solutions. For topical administration they can be effectively incorporated into topical hydrogels [9-10]. The nanosponges used in the formulation of some drugs are provided in the Table 1.

Drug	Nanosponge Vehicle	Indication	Study	In vitro/in vivo/Mathematical model
Paclitaxel	$\beta$ cyclodextrin	Cancer	Bioavailability, Cytotoxicity	Sprague MCF7 cell line
Camptothecin	$\beta$ cyclodextrin	Cancer	Haemolytic activity, Cytotoxicity	Diluted blood HT-29 cell line
Tamoxifen	$\beta$ cyclodextrin	Breast cancer	Cytotoxicity	MCF-7 cell line
Resveratrol	$\beta$ cyclodextrin	Inflammation, Cardiovascular disease, Dermatitis	Cytotoxicity, Accumulation of the drug in the buccal mucosa of rabbit, Permeation study	HCPC-I cell line, Rabbit buccal mucosa, Pig skin
Temozolamide	Poly(valerolactone-allylvalerone) and poly (valerolactone-allylvalerone – oxepanedione)	Brain tumors	Drug release study	In vivo and in vitro study
Econazole	Ethyl cellulose, Polyvinyl alcohol	Antifungal	Irritation study	Rat
Itraconazole	$\beta$ cyclodextrin and copolyvidonum	Antifungal	Saturation solubility study	Higuchi model
Dexametasone	$\beta$ cyclodextrin	Brain tumors	Drug release experiment	Dialysis bag technique in vitro
Antisense oligonucleotides	Sodium alginate, Ply L-lysine	Cancer therapy, Viral infections	Pharmacokinetic studies	Mice

**Table 1: Examples of applications of nanosponges**

### 1.2.2. Nanosponges as carriers for biocatalysts and in the delivery and release of enzymes, proteins, vaccines and antibodies

Many industrial processes involving chemical transformation are associated with operational disadvantages. Non-specific reactions lead to low yields, and the frequent need to operate at high temperatures and pressures requires consumption of large amounts of energy, and very large amounts of cooling water in the down-stream process. All these drawbacks can be eliminated or significantly reduced by using enzymes as biocatalysts. These enzymes operate under mild reaction conditions, have high reaction speed, and are highly specific. They have a beneficial effect on the environment because they reduce energy consumption and reduce production of pollutants.

The catalytic activity of enzymes depend mainly on the correct orientation of the active site. [11] Proteins, peptides, enzymes and derivatives thereof also can be used in the biomedical and therapeutic field. Proteolytic enzymes can be used to treat cancer or type I mucopolysaccharidosis, while DNA and oligonucleotides are used in gene therapy. The administration of these molecules present various problems and limitations. Most protein drugs are poorly absorbed through the biological membranes due to some factors such as large molecular size, hydrophilic nature, degree of ionization, high surface charge, chemical and enzymatic instability and low permeability through mucous membranes. Following intravenous administration, protein molecules may be rapidly cleared from blood, bind to plasma proteins, and sensitive towards proteolytic enzymes. With oral administration, bioavailability is the problem. Various approaches exist for therapeutic use, such as increasing the dose or using absorption promoters, which can cause toxicity problems. [11]

A number of systems for carrying enzymes and proteins have been developed, such as nano and microparticles, liposomes and hydrogels. Carriage in a particular system can protect proteins from breakdown, modify their pharmacokinetics and improve their stability in vivo. It has been found that cyclodextrin based nanosponges are particularly suitable carrier to adsorb proteins, enzymes, antibodies and macromolecules.

In particular when enzymes are used, it is possible to maintain their activity, efficiency, prolong their operation and extends the pH and temperature range of activity and allows the conduct of continuous flow processes. Moreover, proteins and other macromolecules can be carried by adsorbing or encapsulating them in cyclodextrin nanosponges. [11]

### 1.2.3. Other applications of Nanosponges

Nanosponges based on cyclodextrins can strongly bind organic molecules and remove them from water even at very low concentrations. [12] The same concept can be useful for elimination of bitter components from grape fruit juice by selective combination of polymer and crosslinker.

The microporous hyper cross linked nanosponges have been used in selective separation of inorganic electrolytes by size exclusion chromatography. The three dimensional nanosponges will play important role in the fractionalization of peptides for proteomic applications. [13]

Nanosponges can be used as carrier for gases like oxygen and carbon dioxide. These nanosponges could be useful for many biomedical applications. In particular the oxygen-filled nanosponges could supply oxygen to the hypoxic tissues which are present in various diseases. [14] Nanosponges can selectively soak up biomarkers for the diagnosis. One study concluded that nanosponges can harvest rare cancer marker from blood. [15]

### **1.3. Methods of analysis of cyclodextrin-based nanosponges**

CDNS systems are very complex from different points of view, for both their synthesis and their analysis. In this paragraph it will be briefly faced the importance of defining suitable methods to analyze the conformation of nanosponges, intended as reticulation degree and swelling and rheological proprieties, exploiting their chemical configuration and their functional groups. The synthesis phase, instead, will be depth in the following chapter showing a direct correlation with this analysis method.

Primary hydroxyl groups are mainly involved in the formation of a network as shown by FTIR–ATR, Raman and solid-state NMR analyses. [16] Moreover, the elastic properties of cyclodextrin nanosponges were determined by analysis of the spectral modification of the Boson peak and Brillouin frequency. [17] Using ultrasound-assisted synthesis and a suitable cross-linker molar ratio, spherical nanosponges of submicron size were obtained. [18] The cross-linking produces a powder consisting of cyclodextrin connected by nanochannels to form a cage-like structure (Figure 1).

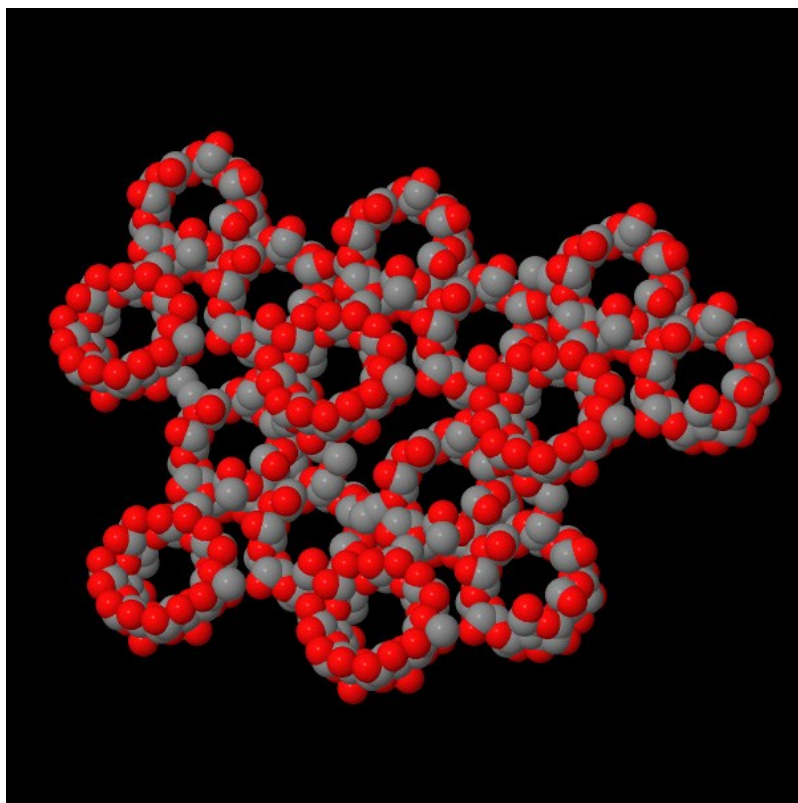


**Figure 1: Molecular structure of cyclodextrin carbonate nanosponges**

By using different amounts of cross-linking agent, or by changing the type of cyclodextrin, it is possible to modulate the channels between the cyclodextrin molecules, thereby tuning the formation of the porous network and consequently affecting both the inclusion capacity and the solubilization ability of the nanosponges. Acid nanosponges bearing free carboxylic groups can be obtained using pyromellitic anhydride or other dianhydrides as a cross-linker, forming cation exchange sites. The presence of free hydroxyl groups in the nanosponges network allows further surface modification. For instance, carboxylated nanosponges can be obtained by reacting pristine carbonate nanosponges with succinic anhydride.

As previously said the study of synthesis of this nanosponges will be faced in the following chapter.



# Chapter 2 - Cyclodextrins

## 2.1. Cyclodextrins

Cyclodextrins (CDs) are the building blocks of nanosponges, object of this thesis. As seen their reaction with different amount of the appropriate crosslink can define the global proprieties of the system. Furthermore the substitution with appropriate functional groups modifies the characteristic of the single cyclodextrin and consequently of the cyclodextrin-based nanosponge (CDNS). Therefore is important to describe the proprieties of CDs and their reactivity.

## 2.2. History

CDs are macrocyclic oligosaccharides most commonly composed of six, seven or eight D-glucopyranose units linked by  $\alpha$ -(1, 4) bonds called  $\alpha$ -,  $\beta$ -, and  $\gamma$ -CD respectively (Figure 2). They are also known as cycloamyloses, cyclomaltoses and Schardinger dextrins. [1-2] They are produced from starch, a renewable natural material, by an intramolecular transglycosylation reaction performed by CD glucanotransferase enzyme (CGTase). [3]

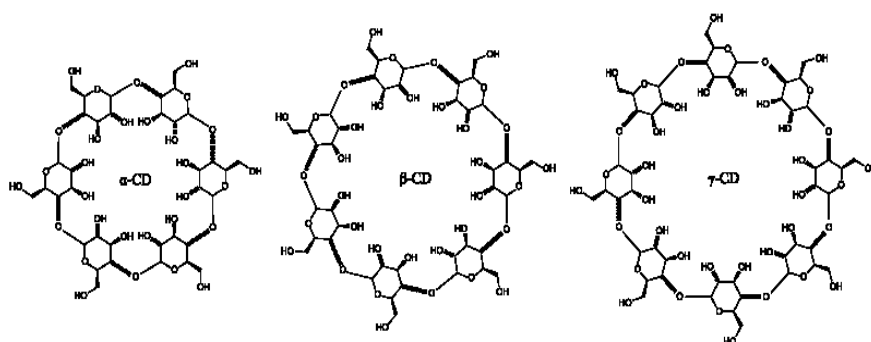


Figure 2: Chemical structure of  $\alpha$ -,  $\beta$ - and  $\gamma$ -CD

### 2.2.1. The discovery period, 1891 to the mids 1930s

CDs were first discovered in 1891. [1] Digesting starch with *Bacillus amylobacter*, Villiers isolated about three grams of a crystalline substance from one kilogram of starch. This substance appeared to be resistant towards acid hydrolysis, and, like cellulose, did not show reducing properties. His experimental results indicated that the substance was dextrin. He determined its composition to be  $(C_6H_{12}O_6) 3H_2O$  and named it "cellulosine".

Now it is thought that the CDs were produced by a *Bacillus macerans* contamination, and Villiers detected both  $\alpha$ - and  $\beta$ -CD. Twelve years later, Schardinger published a report where he described two crystalline products A and B which he isolated from bacterial digest of potato starch. B was identified as the Villiers' "cellulosine". Schardinger named these crystalline products "crystallized dextrin  $\alpha$ " and "crystallized dextrin  $\beta$ ". [4] Through his studies, he also showed that the formation of dextrins depends on the type of bacteria digesting starch and that dextrins could be produced from starch of different sources (potatoes, rice, and wheat).

CDs were named "Schardinger dextrins" in his honor as he was known as the "Founding Father" of CDs chemistry. [4] Nowadays these compounds are called CDs (i.e.  $\alpha$ -CD and  $\beta$ -CD) or less commonly cyclomaltodextrins (i.e. cyclomaltohexaose and cyclomaltoheptaose).

In 1935, Freudenberg and Jacobi discovered  $\gamma$ -CD (cyclomaltooctaose). [5] In 1948, the existence of larger CDs had been suggested. [6]

During the discovery period, the three main natural CDs were discovered and characterized. It was known that they were oligosaccharides but their molecular weight as well as their exact chemical structure and most of their physicochemical properties still remained unknown.

### 2.2.2. The exploratory period, mid 1930s to 1970

In 1938, Freudenberg and co-workers showed that CDs had a ring structure of  $\alpha(1,4)$ -linked glucose units with a central cavity. [5, 7] In the following years, their molecular weight was determined. All the basic structural and physicochemical characteristics of  $\alpha$ -,  $\beta$ - and  $\gamma$ -CDs such as chemical structure, cavity size, solubility, complexing ability and their effect on the chemical stability of guest molecules were described by Cramer in 1954. [8] Their destabilization effect on labile compounds, their potential use as enzyme models and their solubilization effect towards water-insoluble compounds were also discovered. The hypothesis of the existence of larger CDs ventured by Freudenberg and Cramer [6] was verified by French and co-workers. [9] In 1961, evidence for the natural existence of  $\delta$ -,  $\epsilon$ -,  $\zeta$ - and even h-CDs (9-12 residues) was provided by the same group. [10] Due to difficult purification and to unreasonable low yields, large-ring CDs were ignored until the mid 1980. [11]

During this period, enzymatic production of CDs was also being investigated. It was shown that CD glucosyl transferase (CGTase) was able to link the two ends of a fragment provided by the hydrolysis of linear  $\alpha(1,4)$ -linked glucose polysaccharides to give cyclic dextrins. [11] By the end of this area, the methods for the laboratory-scale preparation of CDs, their structural, physical,

chemical and inclusion properties have been discovered. Even if CDs were considered as very promising molecules because of their industrial potential application, they remained very expensive substances, and available only in small amounts as fine chemicals. Their apparent high toxicity brought into question their use for humans. [12]

### 2.2.3. The widespread application and production period, 1970 to present

After demonstrating that the origin of CD “toxicity” came from complexed impurities, an inadequate form of administration, or an extreme dosing and so proving that there is no inherent toxicity of CDs [13], their use was widespread in various applications.

However their price remained a constraint: in 1970,  $\beta$ CD was only available as a rare fine chemical at a price of about US\$ 2000 per kg. Actually, by treating starch with amylase, a crude mixture of  $\alpha$ -CD ( $\approx 60\%$ ),  $\beta$ -CD ( $\approx 20\%$ ),  $\gamma$ -CD ( $\approx 20\%$ ) together with a small amount of CD with more than eight glucose units was obtained. [14] Moreover the mixture was difficult to purify and it frequently contained several other linear and branched dextrans together with a small amount of proteins. With the biotechnological advances that occurred in this decade, the price fell down due to great improvements in their production. Genetic engineering made different types of CGTases available that were both more active and more specific towards the production of  $\alpha$ -,  $\beta$ - or  $\gamma$ -CD than the previously used. These enzymes jointly with other technological innovations (purification, characterization) made highly purified  $\alpha$ -,  $\beta$ - or  $\gamma$ -CD that could be used as pharmaceutical excipients. [15] Today the annual  $\beta$ -CD production is close to 10 000 tones and the bulk price has lowered to about US\$ 5 per kg.

## 2.3. Properties of cyclodextrins

### 2.3.1. Chemical structure of CyDs

CDs are cyclic oligosaccharides containing six ( $\alpha$ -CD), seven ( $\beta$ -CD), eight ( $\gamma$ -CD) ( $\alpha$ -1,4) linked  $\alpha$ -D-glucopyranose units. [16] Rare CDs containing nine ( $\delta$ -CD), ten ( $\epsilon$ -CD) or more glucopyranose units exist but will not be discussed in this thesis. [17, 18]

As a consequence of the  $4C_1$  chair conformation of the glucopyranose units, the hydroxyl functions are orientated to the cone exterior with the primary hydroxyl groups of the sugar residues at the narrow edge of the cone ("primary face") and the secondary hydroxyl groups at the wider edge ("secondary face"). The ring takes the shape of a truncated cone, which is frequently characterized as a doughnut.

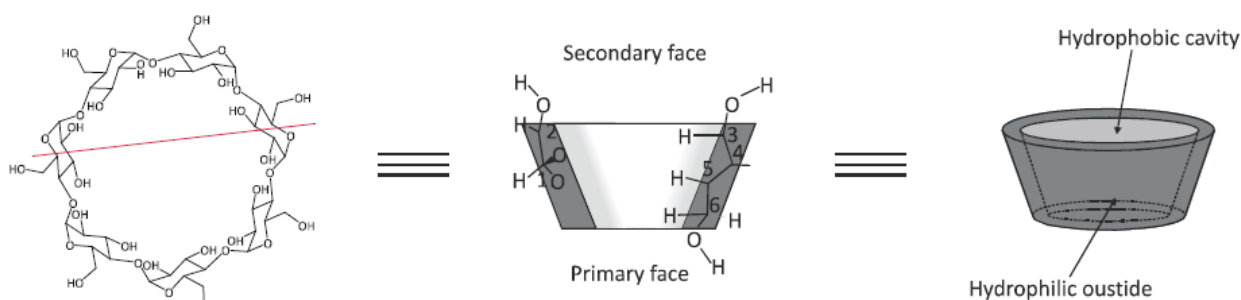


Figure 3: Morphology of CDs

Property	$\alpha$ CD	$\beta$ CD	$\gamma$ CD
Number of glucopyranose units	6	7	8
Molar weight (g/mol)	972	1135	1297
Solubility in water at 25 °C (% w/v)	14.5	1.85	23.2
Optical activity $[\alpha]_D^{25}$ °C	150 $\pm$ 0.5	162.5 $\pm$ 0.5	177.4 $\pm$ 0.5
Outer diameter ( $\text{\AA}$ )	16.4 $\pm$ 0.4	15.4 $\pm$ 0.4	17.5 $\pm$ 0.4
Inner diameter ( $\text{\AA}$ )	4.7-5.3	6.0-6.5	7.5-8.3
Height of torus ( $\text{\AA}$ )	7.9 $\pm$ 0.1	7.9 $\pm$ 0.1	7.9 $\pm$ 0.1
Approx volume of cavity ( $\text{\AA}^3$ )	174	262	427
Approx cavity volume in 1 mol CD (ml)	104	157	256
Approx cavity volume in 1 g of CD (ml)	0.10	0.14	0.20
Crystal forms (from water)	Hexagonal plates	Monoclinic parallelograms	Quadratic prism
Crystal water, wt %	10.2	13.2-14.5	8.13-17.7

Table 2: Characteristic of  $\alpha$ -,  $\beta$ - and  $\delta$ -CD

The cavity of the CD molecule is delimited by the hydrogen atoms and the glucosidic oxygen bridges. The central cavity is lined by the skeletal carbons and ethereal oxygens, which give it a lipophilic character. The C-2-OH group of one glucopyranoside unit can form a hydrogen bond with the C-3-OH group of the adjacent glucopyranose unit.

In the CD molecule, a complete secondary belt is formed by these H bonds therefore the  $\beta$ CD is a rather rigid structure. This intra-molecular hydrogen bond formation is probably the explanation for the lowest water solubility of  $\beta$ CD.

### 2.3.2. CD inclusion complex formation

The most notable feature of CDs is their ability to form solid inclusion complexes (host-guest complexes) with a very wide range of solids, liquids and gases by a molecular complexation. [2] In these complexes (Figure 4), a guest molecule is held within the cavity of the CD host molecule. The lipophilic cavity of CD molecules provides a microenvironment into which appropriately sized non-polar moieties can enter to form inclusion complexes. No covalent bonds are broken or formed during the formation of the inclusion complex. [2]

The main driving force of this process is the release of enthalpy-rich water molecules from the cavity. Water molecules are displaced by more hydrophobic guest molecules present in the solution to establish an apolar-apolar association and to decrease the CD ring strain resulting in a more stable lower energy state. [3]

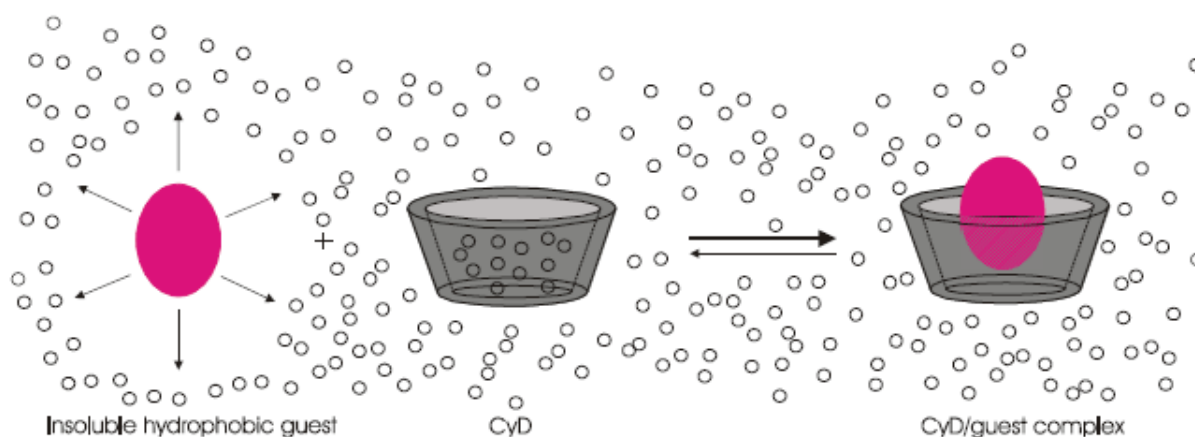


**Figure 4: Schematic representation of CD inclusion complex formation**

The binding of the guest molecule within the host CD is not fixed or permanent but is rather a dynamic equilibrium. Binding strength depends on how well the “host-guest” complex fits together and on specific local interactions between surface atoms. Complexes can be formed

either in solution or in the crystalline state. Water is typically the solvent of choice. Inclusion complexation can be accomplished in a co-solvent system and in the presence of any non-aqueous solvent.

### 2.3.3. Safety and biocompatibility of cyclodextrin

The natural  $\alpha$ -CD and  $\beta$ -CD, unlike  $\gamma$ -CD, cannot be hydrolyzed by human salivary and pancreatic amylases. However, both  $\alpha$ - and  $\beta$ -CD can be fermented by the intestinal microflora. CDs are both large (MW ranging from almost 1000 to over 2000 Daltons) and hydrophilic with a significant number of H-donors and acceptors. As a consequences, they are poorly absorbed from the gastrointestinal tract in their intact form. Hydrophilic CDs are considered non-toxic at low to moderate oral dosages. Lipophilic CD derivatives, such as the methylated CDs, are to some extent absorbed from the gastrointestinal tract in to the systemic circulation and have been shown to be toxic after parenteral administration. B-CD cannot be given parenterally due to its low aqueous solubility and adverse effects (e.g. nephrotoxicity). The metabolism of  $\gamma$ -CD closely resembles that of starch and linear dextrans. Oral administration of 8 g  $\gamma$ CD or 8 g maltodextrin to humans did not reveal any differences in gastrointestinal tolerance of these two oligosaccharides. [19]

### 2.3.4. Regulatory status of cyclodextrins

$\alpha$ -CD,  $\beta$ -CD and  $\gamma$ -CD are listed in the generally regarded as safe (GRAS) list of the FDA (Food and Drug Administration) for use as a food additive and, for example, HP $\beta$ CD (Hydroxyl Propyl  $\beta$ -CD) is cited in the FDA's list of Inactive Pharmaceutical Ingredients. SBE $\beta$ CD (Sulfobutyl Ether  $\beta$ -CD) is also available in various pharmaceutical dosage forms and is also listed in the FDA's compilation of Inactive Pharmaceutical Ingredients. Among regulators it seems that CDs are pharmaceutical excipients and not part of the drug substance although various opinions have been given and interpretation related to this point can be division and product- specific.

Cyclodextrin	Food Approval			Pharmacopoeia Monographs		
	US	Europe	Japan	USP/NF	Ph. Eur	JPC
$\alpha$ CD	GRAS	Planned	Yes	Yes	Yes	Yes
$\beta$ CD	GRAS	Food Additive	Yes	Yes	Yes	Yes
$\gamma$ CD	GRAS	Pending	Yes	In progress	In progress	Yes
HP $\beta$ CD	-	-	-	In progress	Yes	-

**Tabella 3: Regulatory status of the natural cyclodextrin and HP CD**

where:

Gras = Generally regarded as safe list of the Food and Drug Administration in US.

USP/NF = United States Pharmacopoeia/National Formulary

Ph. Eur = European Pharmacopoeia

JPC = Japanese Pharmaceutical Codex

#### **2.4. NMR studies of cyclodextrins**

NMR spectroscopy has become the most important method for structural elucidation of organic compounds, particularly in the solution state. The method is of increasing significance for most cyclodextrin (CD) applications, but is also increasing in popularity for controlling the intricate synthetic modifications of the cycloamyloses by modern preparative methods. [20 – 22] Synthetic variations usually lead to much more complicated spin systems than those in the underlying, highly symmetrical frameworks.

There are few alternatives to NMR spectroscopy in the study of CD. As with many carbohydrates it is often difficult, or too time consuming, to obtain single crystals of CD derivatives and then to analyze them by X-ray crystallography, and even more so by neutron diffraction. Other techniques such as fluorescence, UV/vis spectroscopy, calorimetry, etc. play a major role in measuring complexation energetics with CD, but usually provide only very indirect and qualitative information about inclusion modes and geometries. Structural characterization is of particular significance for supramolecular hostguest complexes, which are the basis of most CD applications in medicine, catalysis, or in food chemistry, separation and sensor technology. Pharmaceutical uses of CD for drug protection or targeting now legally require structural characterization of the administered compounds. NMR spectroscopy is also becoming an important tool for in vitro, in future perhaps even for in vivo, studies of CD interactions with biological macromolecules such as nucleic acids, proteins, or cell membranes. The most obvious incentive, however, to use NMR techniques for the investigation of CD complexes is the interest to understand the driving forces and binding modes in these noncovalent associations, and then to make optimal use of these factors for new applications. It should be reminded, that the driving force for CD inclusion often is of solvophobic nature and that most CD applications involve action in a liquid matrix, which emphasizes again the role of NMR spectroscopy as the most important method applicable in solution. As an example of how misleading it can be to rely only on taken-for-granted assumptions on intracavity inclusion as the major factor behind CD interactions it is cited the well-known

deacylation acceleration of p-nitrophenylacetate by  $\alpha$ -CD. Tee et al. have convincingly demonstrated that opposite to popular earlier views, this does not imply intracavity complexation of the substrate. [23-24]

After the first publications on NMR spectra of CD appeared decades ago [20, 21, 22, 25] and after the pioneering NMR investigations of Bergeron, Komiyama, Demarco and others [26 – 28], there has been a virtual explosion of such studies.

The spectacular advances of NMR techniques during the last years has led to a much more detailed structural elucidation of cyclodextrins and their complexes. These tasks represent a fascinating challenge for the NMR spectroscopist in view of the high complexity of the underlying cycloamylose  $^1\text{H}$  NMR spin systems. These are characterized by signals which, apart from the anomeric proton, absorb in a range of only 0.5 ppm and are strongly coupled. In addition, the shielding effects of the CD cavity on entrapped guest molecules are limited to few tenths of a ppm at most, as a consequence of a host framework being built up entirely of single, less polar and polarizable bonds and thus weak shift tensors.

Cyclodextrins have played a major role in the development of supramolecular chemistry. Such studies should always involve the characterization of their structures, besides the energetics of complex formation. The latter also can be significantly helped by NMR shift titrations, for which modern high-field instruments usually allow to follow several signals, yielding independent data on equilibrium constants. Progress in the empirical quantification of noncovalent forces, and their use for the design of new chemical technologies will essentially depend on knowledge of both thermodynamics and structures of supramolecular complexes in the same state of matter.

In view of the excellent introductions in modern NMR techniques available in several monographs and reviews [29 – 31], this paragraph discuss these methods only along their uses to solve specific problems in cyclodextrin research. First it'll described the conformational properties of free (unsubstituted) and of substituted CD , providing also reference data for substituted derivatives which are gaining more and more importance for many present and future applications.

In this context more qualitative interpretations of  $^1\text{H}$  NMR shifts and the use of vicinal HCCH coupling constants for conformational analyses with emphasis on rotamers around the C5-C6 bond in CD will be analyzed.



### 2.4.1. <sup>1</sup>H NMR Spectra of Cyclodextrins

At magnetic fields above 9.4 T, corresponding to 400 MHz for <sup>1</sup>H NMR spectra, the dispersion is already high enough to locate in conventional onedimensional spectra most of the protons, eased by the high symmetry of the macrocycles (Figure 5 a,b).

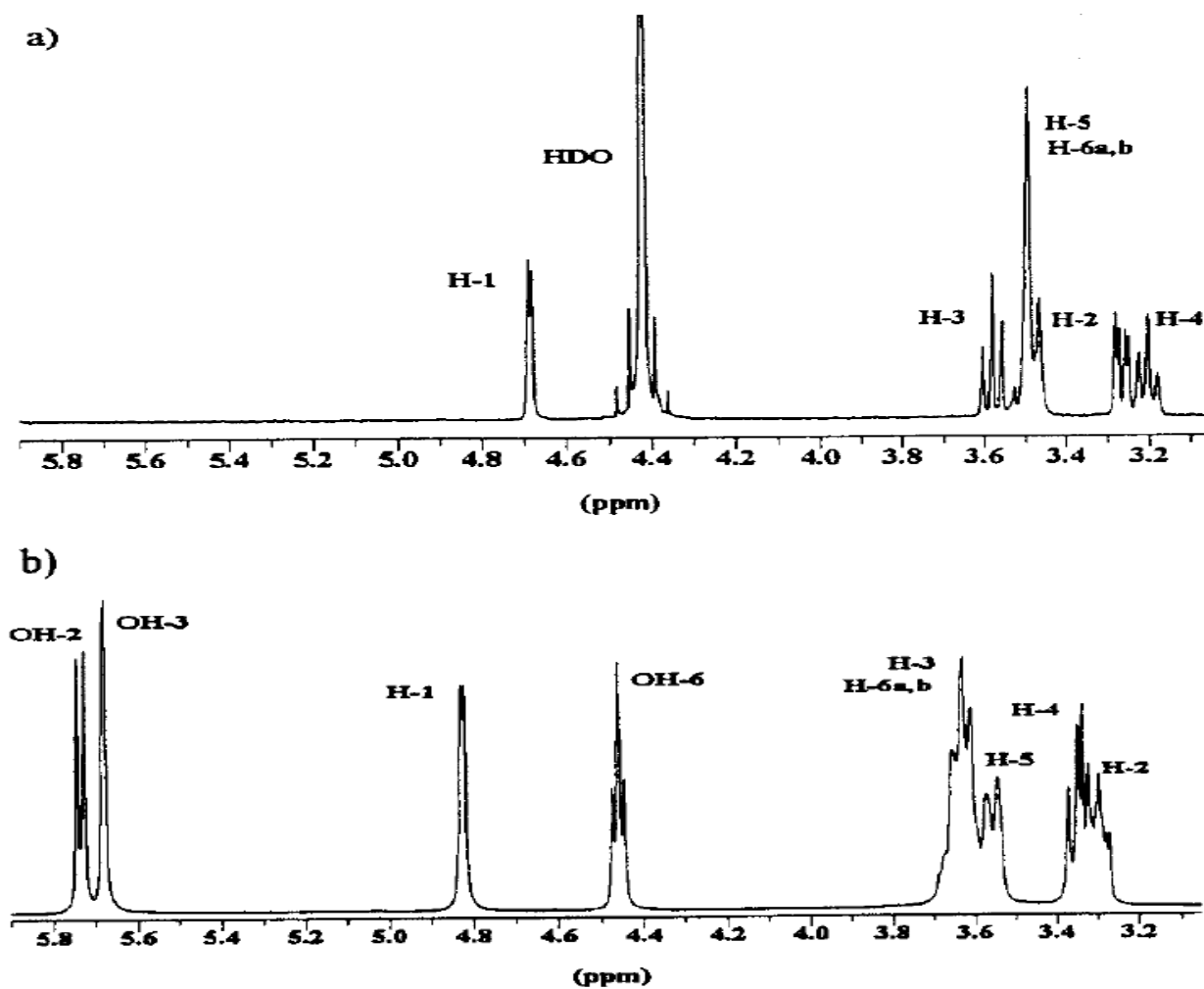


Figure 5: <sup>1</sup>H NMR spectra (400 MHz) of CD at 298 K: (a) in D<sub>2</sub>O and (b) in DMSO-d<sub>6</sub>

Proton shielding differences among  $\alpha$ -,  $\beta$ -,  $\gamma$ -CD amount only to 0.1 ppm at the anomeric H-1, and are even smaller at other positions (Table 4). At fields around 400 MHz, only the anomeric protons are separated well enough from the others for an approximate first-order analysis of the <sup>1</sup>H NMR spin system.

# Chapter 3 – Rheological analysis of CDNS

## 3.1. Synthesis process of CDNS

After analyzing some key aspects about cyclodextrins (CDs), it is now possible to face and focus the real object of this thesis: preparation and characterization of cyclodextrin-based nanosponges (CDNS). Moving on a synthetic point of view, the synthesis of CDNS is difficult to standardize. In order to obtain a product with specific characteristic it is necessary to analyze every aspect of the reaction, from reagents and their condition to reaction time and the work up. By simply modifying a single variable is possible to obtain a completely different product. For this reason it is necessary to define a standard procedure in order to realize a nanosponge which satisfies appropriate rheological features, particularly swelling and gelification (hydrogel).

In the presence of aqueous solutions, CDNS swell [1,2], giving rise to hydrogels, i.e. three-dimensional networks which have the capacity to entrap a large amount of water within their porous structure, depending by crosslinker.

As said before, these polymers can be obtained by reacting native cyclodextrins with a cross-linking agent. If the cross-linker used is a dianhydride it is necessary to work with anhydrous solvents in order to avoid the hydrolysis and consequent formation of carboxylic acids.

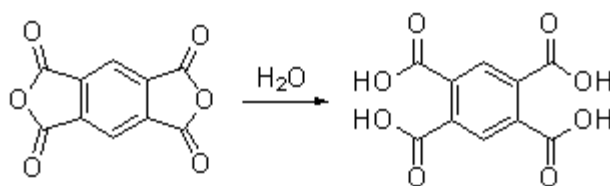
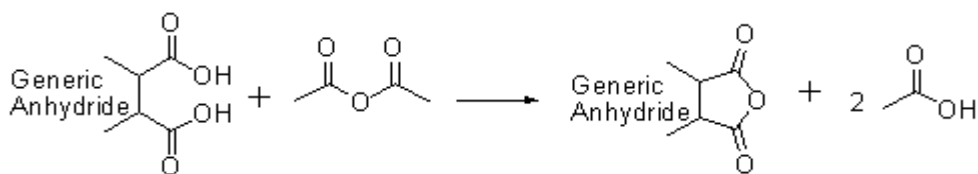


Figure 6: Hydrolysis of generic anhydride

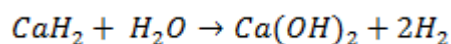
The latter inhibits the formation of ester bond . For the same reason, regeneration of the dianhydride with acetic anhydride is mandatory before conducting the cross-linking reaction.



**Figure 7: Regeneration of generic anhydride**

Through a microwave oven at 1000 W, a flask containing crosslink agent and acetic anhydride was heated at 140 °C (boiling temperature of acetic anhydride) for 1 hour. The resulting product was recovered by filtration under vacuum (18 mbar).

To synthesize CDNS, regardless of the crosslink, dimethyl sulfoxide (DMSO) is used as solvent. The anhydrification of DMSO and Et<sub>3</sub>N, the catalyst of the reaction, is obtained in the presence calcium hydride (CaH) with the release of bubbles of H<sub>2</sub>.



A determinant aspect for the success of the cross-linking is the removal of water from cyclodextrin. In fact, this supramolecules are able to absorb the moisture present in the air. In this way, the water in the cavity of the CDs can compromise a good output of the reaction. For this reason, CDs were dried in oven at 100 °C for 8-9 hours prior to use. The polycondensation of cyclodextrin with the suitable cross linking agent is an exothermic reaction but it is necessary to work at room temperature in order to avoid the freezing of DMSO, whose melting temperature is 18 °C.

The cross-linking is a anhydride-alcohol reaction promoted by a basic catalyst. The fundamental steps can be described by an easier reaction model between a generic anhydride and a primary alcohol, where the first reagent represent the cross-linking agent (e.g. Piromellitic Anhydride, Ethylenediaminetetracetic acid di-anhydride or other di-anhydride) while the second one represents the cyclodextrin in its most reactive position (hydroxyl group at C6).

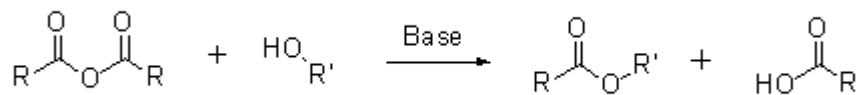
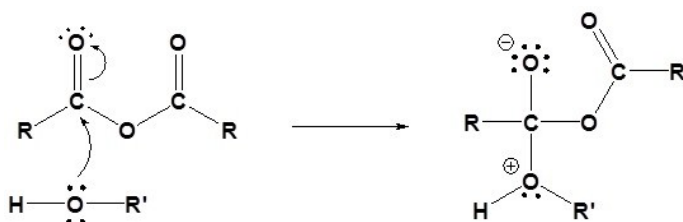


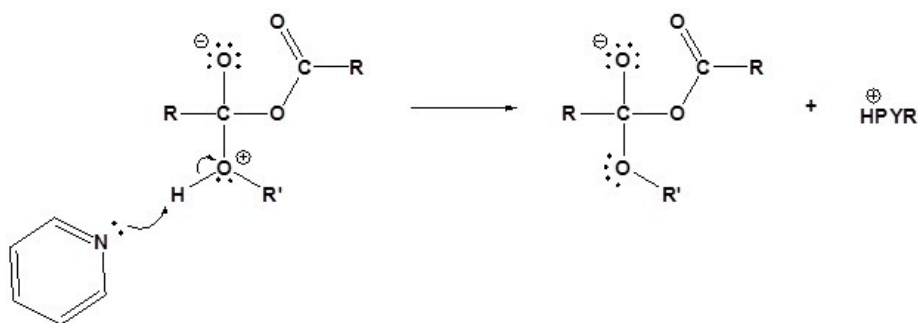
Figure 8: Reaction anhydride - alcohol

In polymerization process here in followed, the two R groups of the generic anhydride are connected forming a ring.

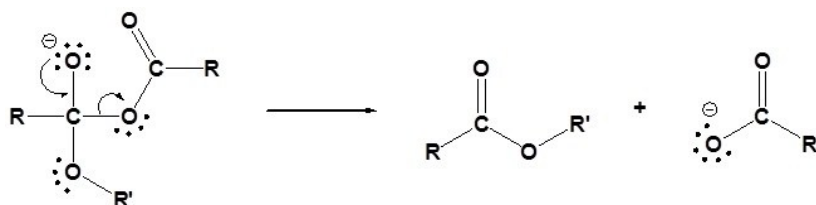
1) Nucleophilic attack by the Alcohol



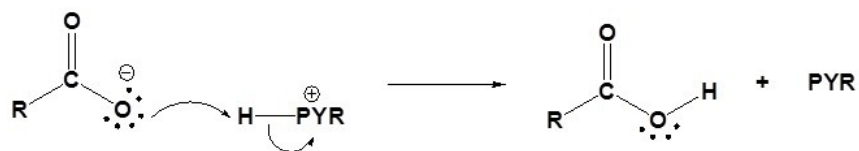
2) Deprotonation by basic agent. Usually a tertiary amines are chosen due to their pKa value (Et<sub>3</sub>N and Py are about 9.7). In this way a substitution with the base is avoided.



3) Leaving group removal



4) Protonation of the carboxylate



Similarly the reaction of polymerization between  $\beta$ -CD and the cross-linking agent PMA involves the formation of ester groups between adjacent molecules of cyclodextrins (Figure 9 (a)), leading to the covalent crosslinked network schematized in Figure 9 (b).

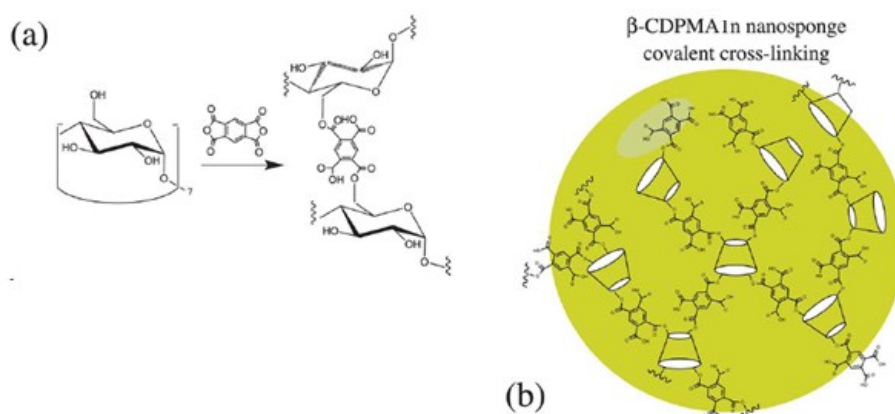
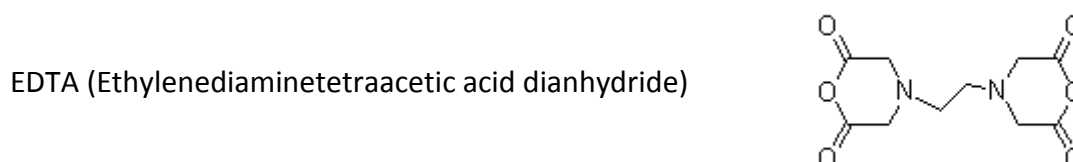
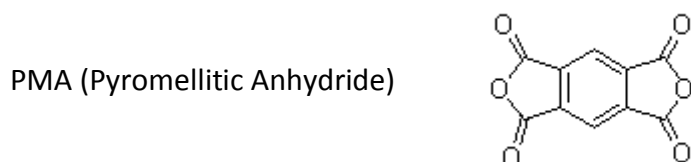


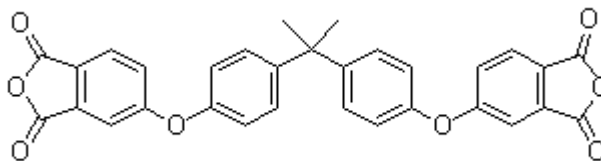
**Figure 9: (a) Scheme of formation of ester groups between two adjacent cyclodextrins. (b) Model of the covalent network of  $\beta$ -CDPMA1n nanosponges.**

### 3.1.2. Synthesis of cyclodextrin-based nanosponges

In a flask of 50 ml, cyclodextrins (1 gr, 0.88 mmol of  $\beta$  – 1.02 mmol of  $\alpha$  – 0.77 mmol of  $\gamma$ ) was dissolved in DMSO (5 ml). Then  $\text{Et}_3\text{N}$  (1 ml), the catalyst of polymerization, was dropped into the flask. The mixture was allowed to stirring until complete dissolution of  $\text{Et}_3\text{N}$  and cyclodextrins into the solvent medium. At occurred dissolution, the appropriate crosslink was used.



BFA (Biphenylanhydride)



In a variable ratio with cyclodextrin, the cross-linker agent was added into the flask and at different time, in relation to its type and his ratio, the polymerization occurred. A hard solid is obtained. This solid was minced using mortar: this step is necessary to ensure a better swelling of the obtained powder, offering a higher surface area with the reduction of diameter and hence a better interaction with water. Finally the minced product was washed in a soxhlet with acetone in order to remove solvent and catalyst. The washed powder was allowed in an oven at 100 °C for 4-5 hours, obtaining pure.

During the synthesis of CDNS, a direct proportional change of polymerization kinetic with the ratio crosslink/cyclodextrin was noted. It was also observed the reliance of the kinetic by the involved crosslink: in fact a polymerization using BFA showed the fastest kinetic between analyzed crosslink giving a solid in a maximum of five minutes; using EDTA, instead, very long time of reaction was observed attending until 6 hours; the use of PMA, finally, required about forty minutes.

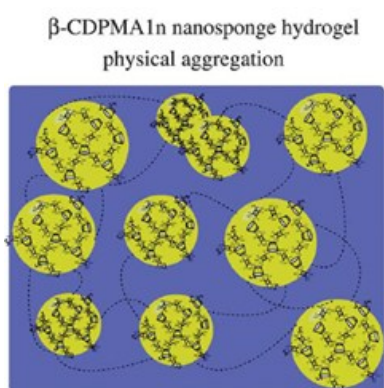


**Figure 10: Schematic representation of the network of non-covalent interactions among different nanosponge molecules in the gel phase.**

### 3.2. Swelling

Two simultaneous effects which involve different length scales ranging from the mesoscopic to macroscopic domain can be supposed to lead to the formation of the hydrogel network as a consequence of hydration of polymers. On one hand, CDNS can swell because of the progressive penetration of water molecules inside the hydrophilic pores of the polymer and, at the same time, different CDNS domains can aggregate via non-covalent (physical) interactions with each other, thus resulting in a three-dimensional network of interconnected domains extending on the macroscopic length scale (i.e. the gel), as summarized in Fig. 10. It is reasonable to assume that the intermolecular interactions, which drive the aggregation of nanosized domains in gel phase, are mainly due to hydrogen bonds. This assumption is consistent with the presence, in the structure of CDNS, of both the hydroxyl (OH) groups of cyclodextrins and the ester and residual free carboxylic (C=O) groups [6, 7] of the covalent network. All these functional groups are acting as hydrogen bond acceptor or donor groups. In turn, these hydrogen bonds are mainly responsible of the different behaviours of the CDNS–hydrogel as a function of temperature.

### **3.3. Direct evidence of gel-sol transition in cyclodextrin-based hydrogel as revealed by FTIR-ATR spectroscopy**

In the last few years different research focused on the understanding how hydrogen bond network and covalent crosslinks determine the swelling and macroscopic properties of nanosponges hydrogels.

The relevance of physical and chemical interactions in nanostructured self-assembled systems is recently emerged in the framework of the rational design of new soft materials. [8] Three dimensional network of cross-linked polymers are considered a very versatile class of components of a bottom-up approach toward self-assembled materials with tailored properties at different length-scales. [9] The possibility of tuning the chemical physical interactions occurring among the different components of these assemblies makes it possible to control the structural properties of the system at the nano and microscales and obtain particular phases of the matter, i.e. liquid or gel states. All these materials rise tremendous interest in fast-growing fields of technology, like drug delivery, tissue engineering and regenerative medicine. [10-12]

By the combined use of inelastic light scattering experiments, infrared spectroscopy and numerical computations, the structural and dynamic properties of dry polymers were explored at molecular level, as a function of some parameters which can be varied during the synthesis of CDNS. [1, 6, 13-15] The results clearly evidenced that the cross-linking degree and the elastic properties of the polymer matrix can be successfully modulated by varying the chemical structure of the crosslinking agent and by acting on the relative amount of the cross-linker with respect to the monomer CD (i.e.  $n$ =cross-linking agent molar excess with respect to CD) during the synthetic procedure. Surprisingly, in all the systems a triggering of stiffness and connectivity was systematically observed in correspondence of a 6-fold excess of cross-linker with respect to CD: this finding gives evidence that at  $n = 6$  a balance between two competing effects (reticulation and branching of CD units) is reached. [14, 15] On the other side, this puzzling scenario was further recently enriched by the accurate inspection of the effect of the confinement of H<sub>2</sub>O and D<sub>2</sub>O in the porous structure of nanosponges. [1, 2, 16] The entire amount of the experimental results suggests that the physical and covalent bonds within the CDNS hydrogels combine to determine the macroscopic properties of the gel phase, like the water holding capacity and the rigidity of the gel network, in a complex interplay over different length scales. [16]



In this work, the investigation on the effect of water confinement in the nano-sized cavities of CDNS is extended, giving a direct evidence of the phase transition process from gel to liquid phase, [8, 17, 18] observed in these cyclodextrin-based hydrogels.

Ester-bridged CDNS based on pyromellitic anhydride have been recently shown to undergo a sol-gel phase transition upon gradual increase of the concentration of CDNS from 0.2 to 2000 mg·mL<sup>-1</sup> in water. [19] Transparent precipitates were formed at 1.0 mg·mL<sup>-1</sup> concentration of CDNS, whose particle size gradually increased by increasing CDNS contents. At higher contents, the solution became a gel-like diphasic system containing both liquid and gel phases or “flowing gel”, and eventually gave a rigid gel at critical gelation ratios depending on the type of CDNS. The hydrogenbond network of water molecules in the polymeric gel as well as the water-polymer interactions are expected to play a crucial role in the progressive sol-to-gel phase evolution.

In the present thesis nanosponges hydrogel obtained by polymerization of  $\beta$ -CD with an activated derivative of ethylenediaminetetraacetic acid (EDTA) at different CD/EDTA molar ratio, have been left to evolve from gel into sol state upon gradual increase of the hydration level. At the same time, the changes observed in the vibrational spectral features assigned to the O-H stretching and HOH bending bands of water molecules progressively confined in the nano-pores of the polymer were monitored during the evolution of the system by using Fourier transform infrared spectroscopy in attenuated total reflectance geometry (FTIR-ATR).

A detailed evaluation of the observed modifications in the OH stretching profile was achieved by decomposition of the band into individual sub-components associated to different levels of water connectivity. The experimental findings are explained by accounting the fraction of water molecules involved and not involved in hydrogen-bonds tetrahedral arrangements. As main result, a cross-over hydration level from gel to liquid state was observed and correlated to the other parameters of the system (i.e. the absorption ability of CDNS and elasticity of the polymer matrix) surprisingly revealing, once again, the fundamental role played by the molar ratio  $n$  to define the nano and microscopic properties of nanosponges hydrogel.

### 3.3.1. Materials and methods

The nanosponges were obtained following the synthetic procedure previously reported. [20, 21] For this analysis EDTA was used as crosslinking agent and cyclodextrins was used in their  $\beta$  conformation. Ethylenediaminetetraacetic acid dianhydride was added at molecular ratios of 1:n (with  $n = 4, 6, 8, 10$ ). The final powder appeared pale yellow.

The corresponding hydrogel of nanosponges was prepared by adding the dry samples of  $\beta$ -CDEDTA1n ( $n = 4, 6, 8, 10$ ) of suitable amount of double-distilled water in order to obtain different levels of hydration  $h$  in the range  $1.4 \div 25.8$ . The hydration level  $h$  is defined as weight ratio  $H_2O/\beta$ -CDEDTA1n. Water containing traces of Rhodamine B dye ( $<0.1\text{mg/L}$ ) was uniquely employed to better visualize the phase evolution of specific samples in photographs.

All the gel samples were freshly prepared and used for FTIRATR measurements.

### 3.3.2. B FTIR-ATR measurements

FTIR-ATR measurements were performed by means of a BOMEM DA8 Fourier transform spectrometer, using a Globar source, a KBr beamsplitter, and a thermo-electrically cooled deuterated triglycene sulphate (DTGS) detector. Spectra were collected at room temperature in the  $400 \div 4000 \text{ cm}^{-1}$  wavenumber range. Samples were contained in a Golden Gate diamond ATR system, based on the attenuated total reflectance (ATR) technique. [22] Each spectrum was recorded in dry atmosphere, in order to avoid dirty contributions, with a resolution of  $4 \text{ cm}^{-1}$ , and is an average of 100 repetitive scans, so guaranteeing a good signal-to-noise ratio and high reproducibility. No mathematical correction (e.g. smoothing) was done, and spectroscopic manipulation such as baseline adjustment and normalization were performed using the Spectralcalc software package GRAMS (Galactic Industries, Salem, NH, USA). Band decomposition of the O-H stretching spectral range ( $2800 \div 3800 \text{ cm}^{-1}$ ) was undertaken using the curve fitting routine provided in the PeakFit 4.0 software package, which enabled the type of fitting function to be selected. The strategy adopted was to use well-defined shape components of Voigt functions with all the parameters allowed to vary upon iteration. The statistical parameters were used as a guide to 'best fit' characterized by  $r^2 \approx 0.9999$  for all the investigated systems.

### 3.3.3. Results and discussion

Figure 11 shows photographs of the phase evolution of a sample of  $\beta$ -CDEDTA14 hydrogel observed as increasing the water content with respect to the amount of nanosponge. The initially rigid opaque gel (the sample does not flow if turned upside down, as evident from the Fig. 11 a)), obtained at low hydration levels, progressively tends to flow as increasing the water content up to become a fluid suspension for high values of  $h$  (Fig. 11 l)). The characteristic hydration levels  $h$  of gelation, as probed by vibrational spectroscopy, depend on the type of nanosponge and they are generally in the range.

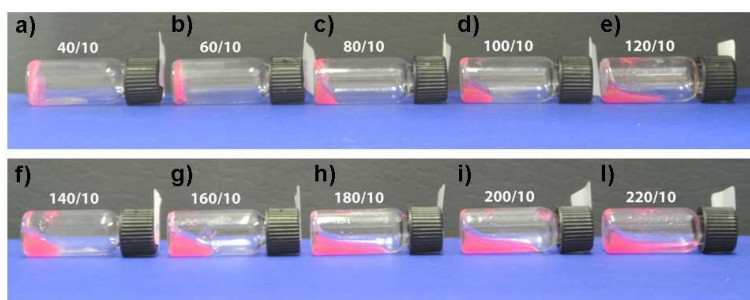


Figure 11: Photographs of samples of  $\beta$ -CDEDTA14 hydrogel obtained as increasing the weight ratios H<sub>2</sub>O/ $\beta$ -CDEDTA14. Note: a suitable dye (Rhodamine B) was added to the water solvent in order to better visualize the phase changes of the system. The hydration level is reported above each vial.

In Fig. 12, (a)-(b), the FTIR-ATR spectra of  $\beta$ -CDEDTA14 and  $\beta$ -CDEDTA110 hydrogel at two different values of hydration  $h = 10$  2.7 and  $h = 16.4$  are reported, in the wavenumber region between 2800 and 3800  $\text{cm}^{-1}$ , as example.

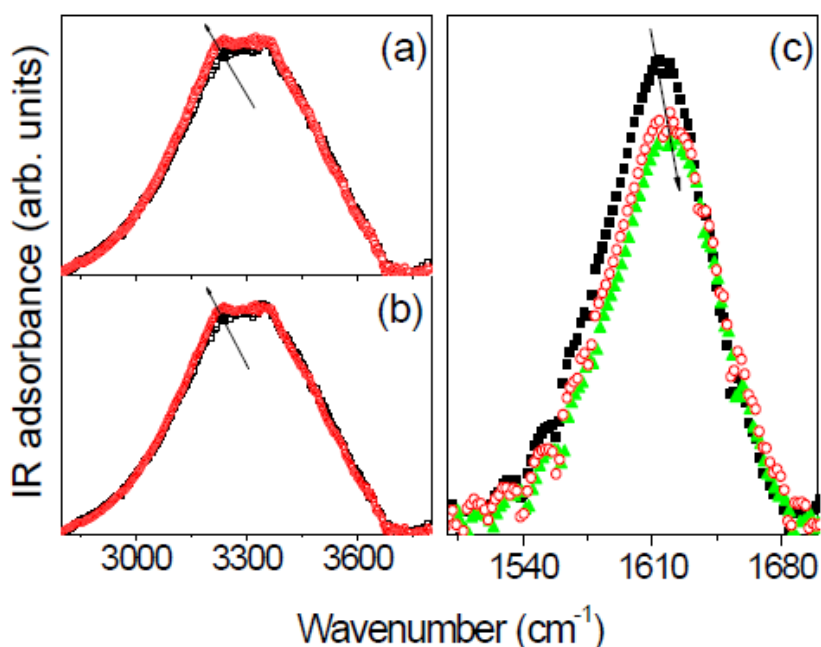


Figure 12: Experimental FTIR-ATR spectra in the O-H stretching region for  $\beta$ -CDEDTA14 (a) and  $\beta$ -CDEDTA110 (b) hydrogels at  $h = 2.7$  (black closed squares) and  $h = 16.4$  (red open circles). (c) Experimental FTIRATR spectra in the HOH bending region for  $\beta$ -CDEDTA18 hydrogel at  $h = 2.7$  (black closed squares),  $h = 11.8$  (red open circles) and  $h = 20.2$  (green closed up triangles).

This specific spectral regime, where typically the O-H stretching band of H<sub>2</sub>O molecules falls, is particularly informative of the three-dimensional interconnected network of hydrogen-bonds in which the molecules of water are involved. [4, 23]

As known [24 – 26], any spectral variation, in shape and/or centre frequency, of the OH stretching profile, can be related to the changes in the characteristic strength, distances and cooperativity of the hydrogen-bonds arrangement involving the water molecules which are attached or confined in the pores of the CDNS polymeric matrix.

The analysis of the spectra acquired at different *h* values points out remarkable changes in the OH stretching profile by varying the hydration level, as indicated by the arrows in Fig. 12 (a)-(b). This experimental finding suggests a redistribution of water molecules among the different hydrogen bond sites as changing *h*. As a general trend, it is observed an increasing of the hydration level corresponds to an enhancement of the low frequency contribution of the OH stretching band, suggesting an increase of the co-operativity in the H-bonds scheme.

These results appear consistent with what already observed in PMA-nanosponges [2] and can be explained by hypothesizing that by increasing the water content a first layer of H<sub>2</sub>O molecules tends to saturate the active sites of the polymer surface, then rearranging in highly coordinated, bulk-like environments. A further confirmation of this interpretation is provided by the behaviour observed for HOH bending band of water molecules which appears as a relative intense and broad band centred at ~1615 cm<sup>-1</sup> (Fig. 12 (c)). This band, assigned to water molecules not involved in a symmetric tetrahedral network, [27, 28] progressively shifts towards higher wavenumbers with increasing *h* values and, at the same time, decreases in intensity as shown in Fig. 12 (c) for β-CD/EDTA18 hydrogel, as an example. The quantitative analysis, of the observed O-H profiles is then carried out by the curve fitting and deconvolution procedure already described in literature. [29 – 32] Accordingly, the O–H stretching profile of water can be decomposed into four classes of O–H oscillators, corresponding to four transient H-bonded and non-H-bonded structures (Fig 13). In particular, the two sub-bands at the lowest wavenumber, namely  $\omega_1$  and  $\omega_2$ , have been assigned to the symmetric and asymmetric O–H stretching mode of water molecules arranged in a tetrahedral network and exhibiting strong hydrogen bonding on both the hydrogen atoms. The spectral component  $\omega_3$  reflects the non-in-phase O–H stretching mode of tetrahedral arrangements commonly referred to as ‘bifurcated Hbonds’, originating distorted tetrahedral structures. Finally, the highest wavenumber sub-band  $\omega_4$  is representative of the O–H mode of water molecules whose H-bond network is, totally or at least partially, broken.

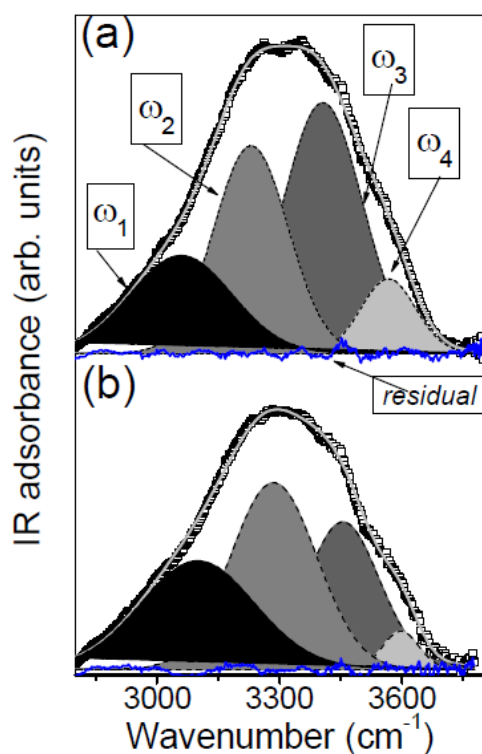


**Figure 13:** Examples of fitting results of O-H stretching profile for  $\beta$ -CDEDTA16 hydrogel at  $h = 4.3$  (a) and  $\beta$ -CDEDTA18 hydrogel at  $h=20.2$  (b). The experimental data (empty squares) are reported together with the best-fit (grey line), the deconvolution components (indicated in the individual subpanels) and the residual (blue lines)

An example of best curve-fitting results is shown for  $\beta$ -CDEDTA16 and  $\beta$ -CDEDTA18 hydrogels at  $h=4.3$  and  $h=20.2$ , respectively, in Fig. 13 (a) and (b).

The presence, in the experimental spectra, of four sub-bands with the assigned centre-frequencies was suggested by the analysis of the second derivative profiles (not reported here) that showed four minima approximately corresponding to the maxima of each band component. This procedure allowed us to overcome, in a way, the well-known difficulties related to the possibility of uniquely fitting IR band profiles. [33, 34] Finally, it is remarked that the protocol adopted here makes use of the minimum number of parameters, furnishing at the same time best-fits characterized by  $r^2 \sim 0.9999$  for all the analyzed samples.

From the inspection of the Fig. 14, it clearly appears that to an increase of the water content corresponds to an enhancement of the population of water molecules arranged in highly coordinated, hydrogen bonded networks (I1 and I2), i.e. bulk-like contribution. Correspondingly, a decreasing of the population of water molecules involved in less cooperative structures which are typically associated to water molecules “perturbed” by the presence of solutes or attached to

some interface (I3 and I4), is found with increasing  $h$ . Moreover, a characteristic saturation effect is observed at the high values of  $h$  for the populations I1 and I4.

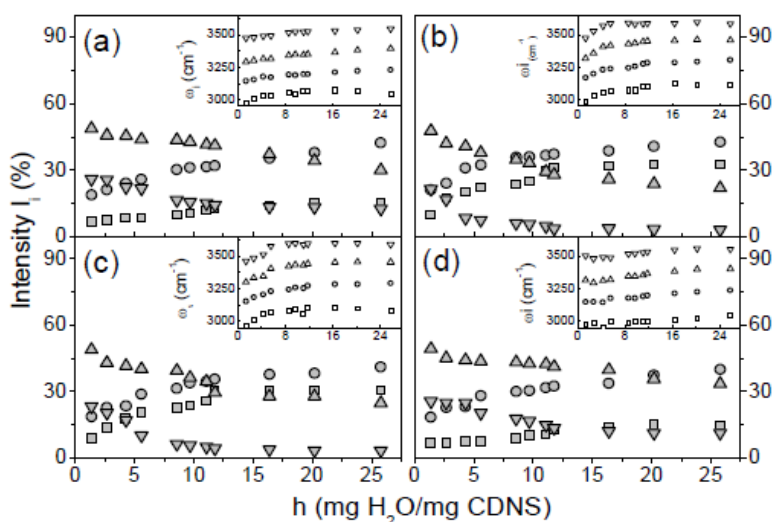


**Figure 14:** Percentage intensities  $I_i$  of the different spectral contributions to the O-H stretching band as a function of the hydration level  $h$  for (a)  $\beta$ -CDEDTA14, (b)  $\beta$ -CDEDTA16, (c)  $\beta$ -CDEDTA18, and (d)  $\beta$ -CDEDTA110 hydrogel. I1: closed squares, I2: closed circle, I3: closed up triangles; , I4: closed down triangles. For each plot, the inset reports the evolution of the corresponding peak wavenumbers:  $\omega_1$ : open squares,  $\omega_2$ : open circles,  $\omega_3$ : open up triangles,  $\omega_4$ : open down triangles.

For all the analyzed samples, any single H-bond environment is slightly reinforced by increasing the hydration level, as indicated by the behaviour of the peak wavenumbers reported in the insets of Fig. 14.

These findings could be explained by invoking an increasing in the pore size of nanosponges, as increasing  $h$ , up to a certain value of the hydration level beyond which the nano-cavities of CDNS are no longer able to enlarge, despite the fact that other water molecules are added. This interpretation is consistent also with small angle neutron scattering measurements recently performed on CDNS hydrogel which will be reported elsewhere.

The conclusion that high values of  $h$  induce an enlargement of size pores of nanosponges can be further supported by previous Raman spectroscopy investigations, aimed at exploring the influence of nanoscopic confinement on the vibrational properties of liquid water confined in Gelsil glass with pores of different dimensions. [35] In that case, a detailed evaluation of the observed changes in the O–H stretching profile gave evidence that the population associated to fully tetrahedrally hydrogen bonded water molecules is lower in the case of water confined in Gelsil 75 Å with respect to Gelsil 200 Å, allowing to hypothesize that enlarging pore diameter produces on the connectivity pattern of water an effect similar to that obtained by lowering temperature.

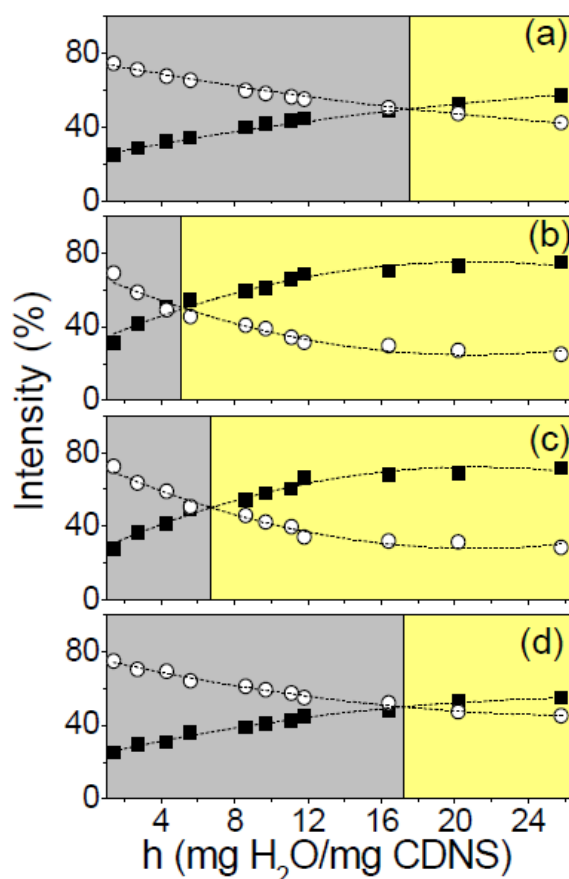


**Figure 15: Percentage intensities I1+I2 (closed squares) and I3+I4 (open circles) of the spectral contributions to the O-H stretching band, as a function of the hydration  $h$ , for (a)  $\beta$ -CDEDTA14, (b)  $\beta$ -CDEDTA16, (c)  $\beta$ -CDEDTA18, and (d)  $\beta$ -CDEDTA110 hydrogel. The vertical lines indicates the value.**

In order to give a more synthetic view of the phenomena, the intensities (I1+I2) and (I3+I4) are considered which are representative of the population of the bulk-like (i.e. tetraordinated) and not bulk-like water molecules, respectively. The behaviour of these quantities is reported as a function of hydration  $h$  in Fig. 15 (a)-(d) for all the analyzed  $\beta$ -CDEDTA1n hydrogel. The experimental data were fitted by using a simple second-order polynomial function (dashed lines in Fig. 15) which well describes the evolution of the experimental points.

The curves reported in Fig. 15 clearly give evidence of the existence of a characteristic crossover point. Such point is indicative of the experimental conditions where the tetrahedral arrangements of the water molecules become favoured with respect to the structures having connectivity less than four (vertical lines in panels of Fig. 15). An estimation of the hydration level  $h_{cross}$  at the cross-over condition can be obtained directly by the curves of Fig. 15 for each of the investigated hydrogels. The  $h_{cross}$  can be seen as a descriptor of the maximum hydration level above which the pores of nanosponge are saturated. At higher water content, H<sub>2</sub>O molecules tend to rearrange

in more cooperative, bulk-like networks, due to the lack of available space inside the pores of the polymeric matrix.

Correspondingly, for  $h > h_{cross}$  the phase transition from a rigid gel-forming system to a fluid suspension is observed, as revealed in the photographs of Fig. 16.

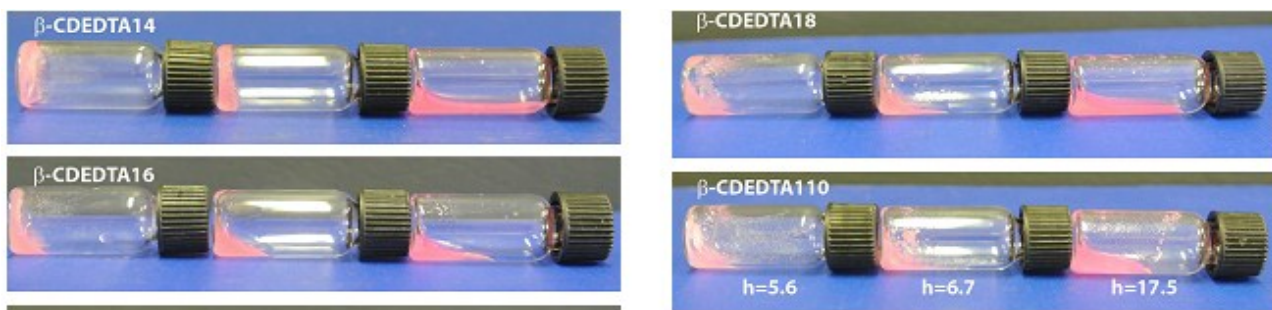


**Figure 16: Photographs of different phase behaviour for  $\beta$ -CDEDTA1n hydrogels as increasing the level of hydration  $h$ . Note: a suitable dye (Rhodamine B) was added to the water solvent in order to better visualize the phase changes of the system.**

In Fig. 17, the estimation of  $h_{cross}$  is reported as a function of the parameter  $n$  which represent the molar ratio between crosslinking agent EDTA and the monomer CD used in the synthesis of the nanosponge polymer matrix.

Two different regions corresponding to a phase of rigid gel state and fluid suspension can be identified for  $h < h_{cross}$  and  $h > h_{cross}$ , respectively, as evidenced in Fig. .

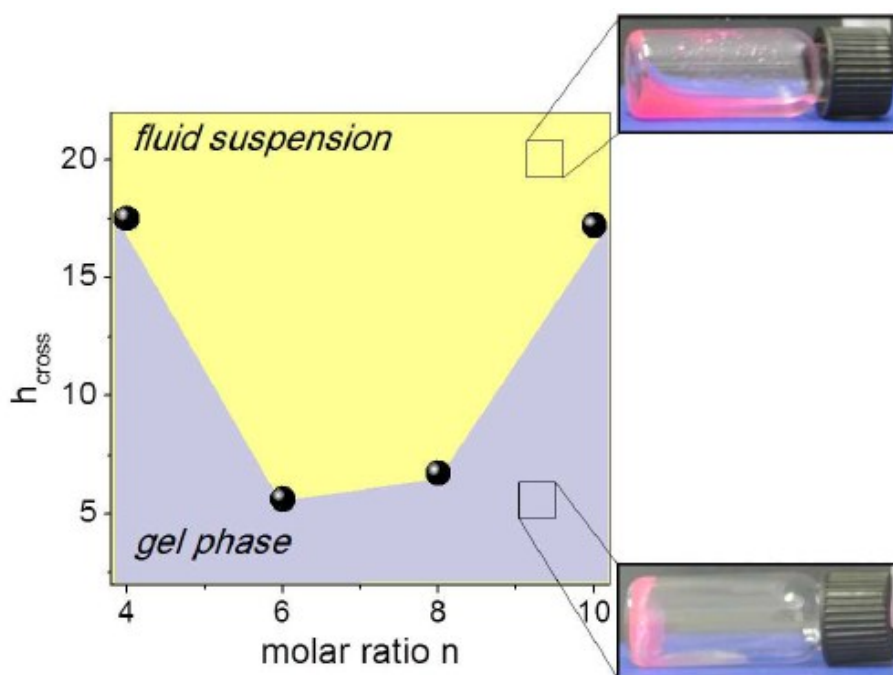


**Figure 17: Crossover hydration level  $h_{cross}$  estimated for nanosponges hydrogels as a function of the parameter  $n$ .**



Interestingly, the plot shown in Fig. 17 points out an inversion point in correspondence of a 6-fold excess of cross-linker with respect to CD, closely recalls what already observed on different classes of nanosponges by low-frequency Raman, Brillouin and FTIR-ATR experiments, in dry and gel state. Considering the dry CDNS [1, 6, 13 - 15] the six-fold excess of cross-linking agent with respect to CD corresponded to the maximum extent of bond connectivity and stiffness of the polymers. Further excess of cross-linking agent was shown to provide branching of cyclodextrin units rather than a further increase of the polymerization. Upon hydration, [2, 16] it was found that the molar ratio  $n = 6$  corresponds also to the formation of the most strongly interconnected hydrogen-bonded network in the hydrogel. [16] On the other side, higher values of  $n$  were found to decrease the degree of the hydrogen bond network due to the destructuring effects associated to the increased steric hindrance of the polymeric network introduced by the excess of cross-linker.

The plot of Fig. seems to indicate that the saturation of the confinement sites of water (i.e. the pores of the nanosponge) is reached, in the case of  $n = 6$ , at lower hydration levels with respect to the other nanosponges.

This means that  $\beta$ -CDEDTA16 nanosponge is able to entrap much less water with respect to, for example,  $\beta$ -CDEDTA18 while  $\beta$ -CDEDTA14 and  $\beta$ -CDEDTA110 nanosponges appear to be the most absorbent polymers.

Two possible explanations to this occurrence can be given. On one side, the reduced ability of  $\beta$ -CDEDTA16 nanosponge to adsorbing water can be ascribed to its highest rigidity, as proved by previous Brillouin and Raman measurements. [14, 15] As a consequence, water molecules show reduced capability to enlarge the pores and a lower number of H<sub>2</sub>O molecules are confined.

Another reasonable hypothesis could be that the pores of  $\beta$ -55 CDEDTA16 nanosponge may have smaller dimensions with respect to the other samples, as  $\beta$ -CDEDTA16 exhibits the highest cross-linking degree. The interplay between the two factors reported above is currently being investigated by small angle neutron scattering and will be reported elsewhere.

Finally, a discussion of the behaviour, as a function of  $n$ , of the percentage intensities  $I_1+I_2$  at different hydration levels  $h$  is worth of mention.

In Fig. 18 an estimation of the quantity  $I_1+I_2$  is plotted, as a function of the parameter  $n$ , for each investigated hydration level  $h$ .

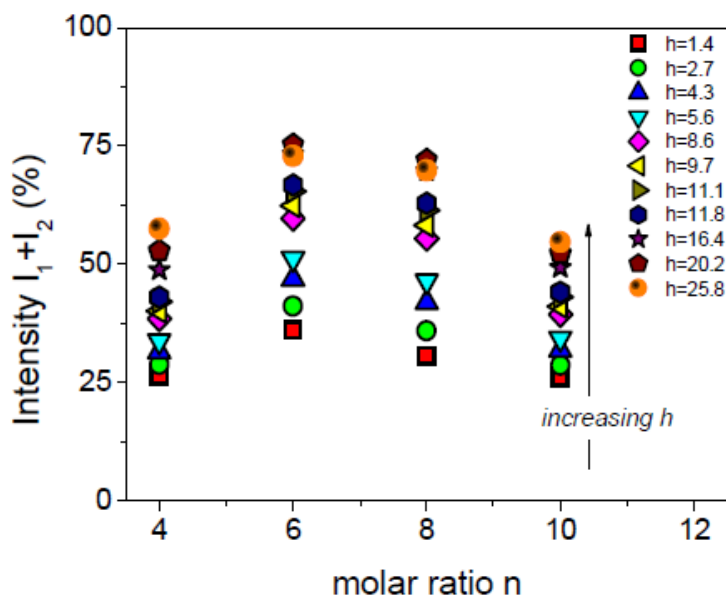


Figure 18: Percentage intensities  $I_1+I_2$  reported as a function of the molar ratio  $n$  for different values of hydrations  $h$ , as indicated in the panel.

The maximum value of  $I_1+I_2$ , i.e. the maximum value of the population corresponding to tetrahedral contributions, is always reached at  $n = 6$ . That is, whatever hydration level is considered, at least in the explored  $h$ -range, the tetrahedral network of water molecules becomes prevalent in  $\beta$ -CDEDTA16 nanosponge with respect to the others. This finding confirms that the properties observed for  $n=6$  in ester-based CDNS are deeply related to the structure of the polymeric network as obtained by the synthetic process.

### 3.3.4. Conclusions

Direct evidence of gel-sol phase transition in a new class of cyclodextrin-based hydrogel is given by monitoring the changes occurring in the vibrational dynamics of the system during its evolution.

The hydration of cyclodextrin nanosponges with progressively increasing amounts of water allowed us to follow the transition of the polymers from a state of a rigid gel into a liquid suspension.

At the same time, measurements of the spectral changes occurring in the O–H stretching and HOH bending profile of water molecules progressively confined in the nano-pores of CDNS were carried out by using Fourier transform infrared spectroscopy in attenuated total reflectance geometry (FTIRATR).

To this end, best-fitting and deconvolution procedures were employed for the separation of spectral components contributing to the O–H stretching band in order to account the connectivity pattern of water molecules concurring to the gelation process of CDNS. The experimental data give evidence that the increase of the hydration level in nanosponges is accompanied by an enhancement of the population of H<sub>2</sub>O molecules engaged in tetrahedral-coordinated hydrogen-bonds networks. This configuration becomes dominant with respect to the no bulk-like contributions above a characteristic cross-over hydration level  $h_{cross}$ . As main result, this crossover was demonstrated to be strictly correlated to the macroscopic properties of the system (i.e. the absorption ability of CDNS and rigidity of the corresponding hydrogel network) and to be strongly dependent, on the cross-linking agent/CD molar ratio.

These findings suggest the existence of a specific phase diagram of the cyclodextrin nanosponges hydrogels, where the parameter  $n$  plays a fundamental role in defining the nano- and microscopic properties of the system. Finally, these results provide a novel contribution to the rational comprehensive view of the chemicalphysical interactions controlling the behaviour of self-assembled cyclodextrin-based systems over different length scales. Future efforts will be devoted to the study of the rheological properties of these hydrogels in order to better define their macroscopic mechanical properties.

### 3.4. Glass-like dynamics of new cross-linked polymeric systems: Behavior of the Boson peak

Recent experimental-numerical works [1, 6, 7, 13 – 15] showed how the study of the vibrational dynamics of CDNS is a powerful tool to characterize amorphous polymeric networks, from a structural point of view, too. The detailed analysis of the high-frequency vibrational dynamics of nanosponges revealed a clear dependence of the hydrogen-bonded network involving the OH groups of the polymers on the temperature and on the cross-linking degree of CDNS. [6] Moreover, the inspection of the vibrational spectra of the polymers over a broad spectral range [1, 7, 13 – 15] allowed us to demonstrate that the cross-linking density of the polymeric network and the stiffness (i.e., rigidity) of the whole material can be effectively tuned by varying the chemical structure of cross-linking agent and the reaction conditions. In particular, the relative amount of crosslinking agent with respect to the monomer CD (i.e.,  $n = \text{crosslinking agent/CD molar ratio}$ ) was observed to be the parameter which mainly can affect the covalent connectivity [7, 13, 15] and the elastic properties of the polymeric matrix. [1, 14, 15]

The low-energy vibrational excitations of cyclodextrin nanosponges, obtained by polymerization of  $\alpha$ - and  $\gamma$ -CD with the cross-linking agent ethylenediaminetetraacetic acid (EDTA), are investigated by means of Raman scattering experiments. The structure of  $\alpha$ - and  $\gamma$ -CD differs by the number of glucose units, composed of macrocycle (6 and 8, respectively), and this is reflected in a different size of the cavity diameter of the CD ( $\approx 4.7$  and  $7.5 \text{ \AA}$  for  $\alpha$ - and  $\gamma$ -CD, respectively). The aim of this thesis is exploring as how the steric hindrance and the number of reactive sites on each CD unit (which varies from 12 secondary and 6 primary OH groups to 16 secondary and 8 primary groups per CD residue passing from  $\alpha$ -CD to  $\gamma$ -CD) can affect the stiffness properties of the polymer network over a mesoscopic length scale. For this purpose, the spectral evolution of the so-called Boson peak (BP), a vibrational feature usually observed in the low-energy vibrational spectra of a wide range of different amorphous materials, [36 – 39] will be analyzed and discussed in terms of a physical descriptor correlated to the elasticity properties of these amorphous polymeric networks. [14, 15]

### 3.4.1. Materials and methods

The nanosponges were obtained following the synthetic procedure previously reported. [20, 21] For this analysis EDTA was used as crosslinking agent and cyclodextrins was used in their  $\alpha$  and  $\gamma$  conformation. Ethylenediaminetetraacetic acid dianhydride was added at molecular ratios of 1:n (with  $n = 2, 6, , 10$ ). The final powder appeared pale yellow.

### 3.4.2. Raman scattering measurements

All the Raman measurements were carried out at room temperature from dried specimens of nanosponges placed on a glass slide exposed to air. Cross-polarized (HV) anti-Stokes and Stokes Raman spectra were recorded over the wave number range between about  $-400\text{ cm}^{-1}$  and  $+370\text{ cm}^{-1}$  in backscattering geometry, by means of a triplemonochromator spectrometer (Horiba-Jobin Yvon, model T64000) set in double-subtractive/single configuration and mounting three holographic gratings with 1800 grooves/mm. Micro-Raman spectra were excited by the 632.8-nm wavelength of a helium/neon or by the 647.1-nm wavelength of an argon/krypton ion laser and detected by a multichannel detector (CCD with  $1024 \times 256$  pixels) cryogenically cooled by liquid nitrogen. The laser beam was focused onto the sample surface with a spot size of about  $1\ \mu\text{m}^2$  through an 80 $\times$  objective of the microscope with  $\text{NA} = 0.75$ . The resolution was better than  $0.4\text{ cm}^{-1}/\text{pixel}$ .

No appreciable damage due to possible heating of the sample was observed by means of an accurate inspection of the irradiated sample surface throughout the camera coupled to the microscope objective and carried out after each measurement. Moreover, four Raman spectra were recorded from different regions of each examined sample in order to verify their reproducibility.

### 3.4.3. Results

Cross-polarized Raman intensity  $I_{\text{Raman}}(\omega, T)$  of  $\alpha$ -CDEDTA110 nanosponge is shown in the wave number region between  $+200 \text{ cm}^{-1}$  and  $-200 \text{ cm}^{-1}$  (Fig. 19). The experimental profile shows two different contributions, which appear evident in both the anti-Stokes and Stokes components of the spectrum: a quasi-elastic (QE) signal, related to diffusive and relaxational dynamics of the system, which appears as a broadening of the elastic peak, and the broad bump, characteristic of disordered systems, usually referred as the boson peak (BP).

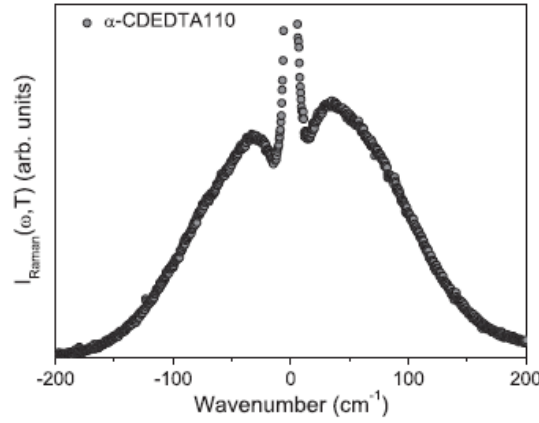


**Figure 19: Cross-polarized (HV) Raman intensity  $I_{\text{Raman}} \text{ HV}$  of  $\alpha$ -CDEDTA110 nanosponge in the wave number region between  $+200 \text{ cm}^{-1}$  and  $-200 \text{ cm}^{-1}$ .**

According to Shuker and Gammon model [40], the experimental intensity  $I_{\text{Raman}}(\omega, T)$  of Raman scattering Stokes processes turns out to be proportional to the density of states  $g(\omega)$  through the following relation:

$$I_{\text{Raman}}(\omega, T) = C(\omega)g(\omega) \frac{[n(\omega, T) + 1]}{\omega}$$

where  $n(\omega, T) = [\exp(\hbar\omega/kT) - 1]^{-1}$  is the temperature Bose factor and  $C(\omega)$  is the coupling function between light and vibrational mode of frequency  $\omega$  of the system.

In order to rule out the temperature dependence of the Raman spectra, the measured intensity can be converted into the reduced Raman intensity, defined as

$$I^{\text{Red}}(\omega) = \frac{I_{\text{Raman}}(\omega, T)}{[n(\omega, T) + 1]\omega} = C(\omega) \frac{g(\omega)}{\omega^2}$$

The reduced Raman intensity  $I^{Red}(\omega)$  derived from the Stokes component of the cross-polarized spectrum of three different  $\alpha$ -CDEDTA1n nanosponges in the low-energy region (0–200  $\text{cm}^{-1}$ ) is shown in Fig. 20, as an example.

In order to compare Raman spectra acquired on different samples of EDTA nanosponges, the experimental data were preliminary normalized to the total measured area.

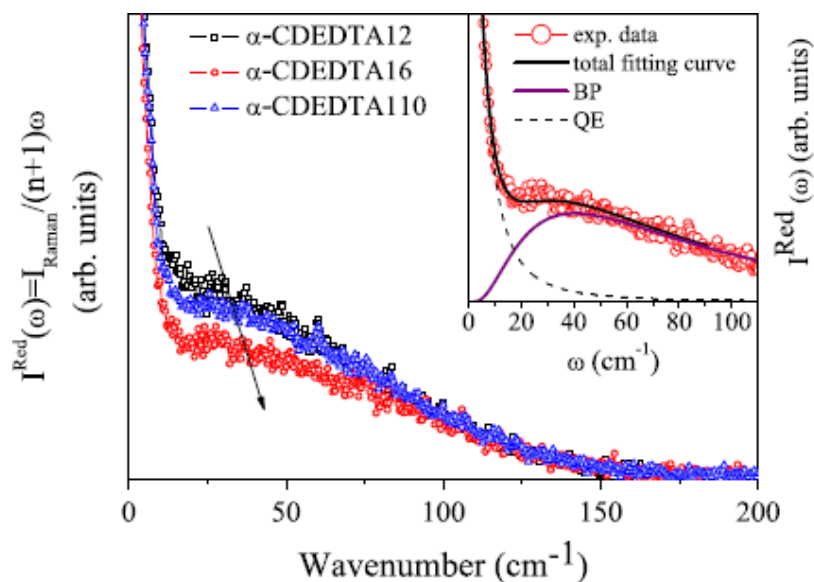


Figure 20: Reduced Raman spectra of  $\alpha$ -CDEDTA1n nanosponges ( $n = 2, 6, 10$ ) in the energy range 0–200  $\text{cm}^{-1}$ ; the arrow indicates the evolution of the BP peak frequency. (Inset) Typical example of the best fitting results for  $\alpha$ -CDEDTA16: the experimental data (red circles) are shown together with the total fitting curve and the different components (QE, quasi-elastic; BP, boson peak).

The total reduced Raman intensity reported in Fig. 20 can be effectively modeled as the sum of two spectral components:

$$I^{Red}(\omega) = I_{QE}(\omega) + I_{BP}(\omega)$$

Where  $I_{QE}(\omega)$  and  $I_{BP}(\omega)$  are the respective spectral intensities.

The inspection of the experimental profiles of Fig. 20 points out significant variations of both intensity and frequency position of the BP, as a function of the  $n$  parameter. By the way, the intensity of the quasi-elastic signal varies, passing also from its maximum value in the spectrum of  $\alpha$ -CDEDTA12 nanosponges to its minimum value in the  $\alpha$ -CDEDTA16 sample.

Since in this work only the boson peak variations are investigate, the  $I_{QE}(\omega)$  of the quasi-elastic contribution was subtracted from the total experimental profile  $I^{Red}(\omega)$  by adopting a well-established fitting procedure, already successfully applied to other polymeric systems. [14, 15, 41

– 43] In the inset of Fig. , the best fitting results for the reduced Raman spectrum of  $\alpha$ -CDEDTA16 are shown. The total experimental profile  $I_{Red}(\omega)$  is well reproduced by the sum of a Lorentzian function, centred at zero wave number, with width  $\Gamma$  and amplitude  $A$  to model the QE contribution (dashed line), and a lognormal distribution function that well describes the shape and the position of the BP with width  $W$ , amplitude  $B$  and peak frequency  $\omega_{BP}$  (continuous line).

$$I_{Red}(\omega) = \frac{A\Gamma}{\Gamma^2 + \omega^2} + B \exp\left\{-\frac{[\ln(\omega/\omega_{BP})]^2}{2W^2}\right\}$$

It is noteworthy that the choice of the log-normal function, although arbitrary, provides a suitable method to estimate in more quantitative way the position of the maximum of BP. [14, 15, 41 – 45] The data handling described above has been applied to the Raman spectra of both  $\alpha$ - and  $\gamma$ -EDTA1n nanosponges.

#### 3.4.4. Discussion

Fig. 21 displays the Stokes components of the reduced Raman spectra of the three different samples of  $\alpha$ -CDEDTA1n nanosponges, in the spectral range 0–200  $\text{cm}^{-1}$ , obtained after the subtraction of QE contribution. The profiles obtained in this way correspond only to the intensity  $I_{BP}(\omega)$  of the vibrational component of the reduced spectra.

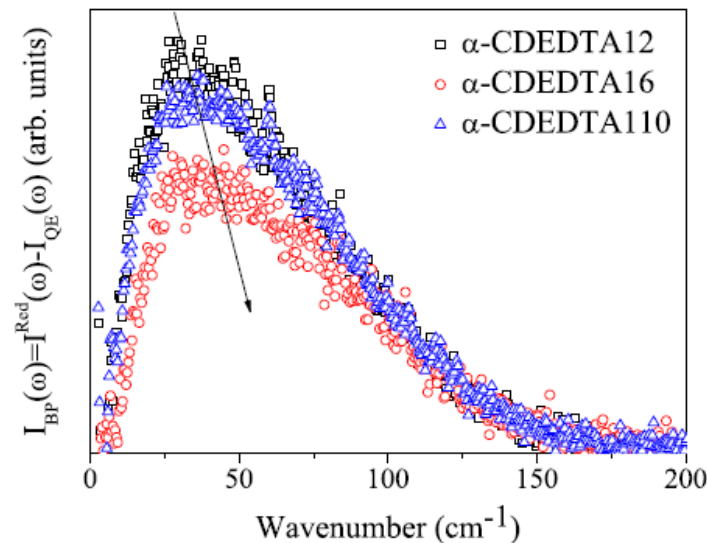
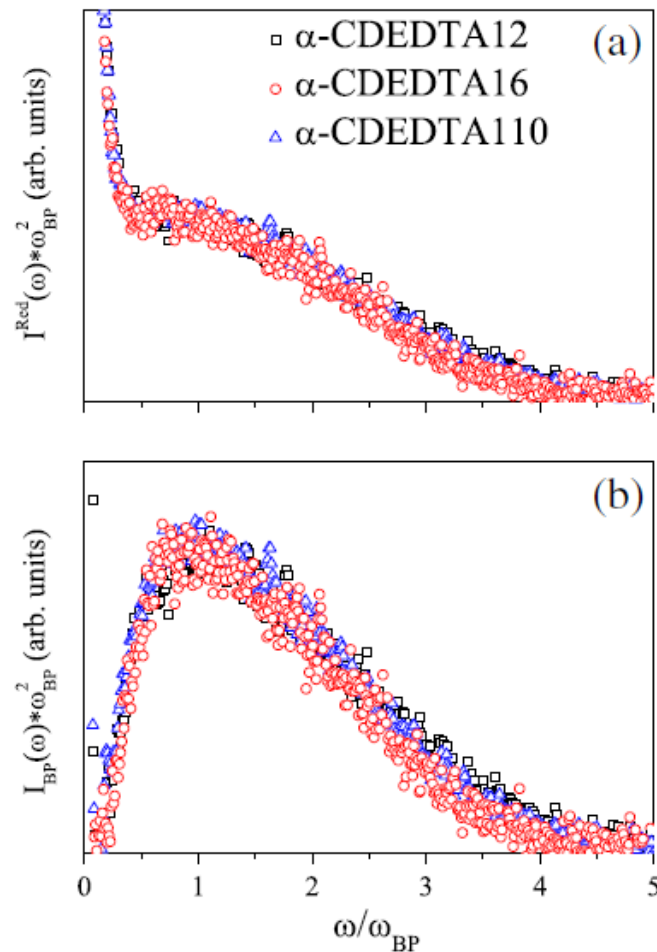


Figure 21: Reduced Raman spectra of  $\alpha$ -CDEDTA1n nanosponges ( $n = 2, 6, 10$ ) after subtraction of QE contribution in the energy range 0–200  $\text{cm}^{-1}$ .



It turns out clearly evident that the boson peak shifts toward higher wave numbers and decreases in intensity when the parameter  $n$  passes from 2 to 10 and then to 6. It should be pointed out that the overall evolution of the vibrational component, obtained after subtraction of the QE contribution, is the same as the one observed for the reduced Raman spectra of Fig. 22, thus confirming that the described subtraction procedure of the QE contribution does not affect the final results. As already widely demonstrated in previous work papers, [14, 41 – 44] a clear relationship exists between the changes in the frequency and intensity of the BP and the transformation of the elastic properties of the material over a mesoscopic length scale. As a matter of fact, it has been shown that the position of the maximum of BP tends to move to higher energies when the stiffness of the amorphous system increases, as induced by pressure, [41 – 43] density [44 – 46] or increasing of connectivity. [14, 15] In particular, in the case of cyclodextrin-based polymers, it has been observed that the evolution of  $\omega_{BP}$  as a function of the cross-linking degree of the polymeric network is in fair agreement with the trend observed for the Brillouin sound velocity measured on the same samples. [14]



**Figure 22:** Reduced Raman spectra of  $\alpha$ -CDEDTA1 $n$  nanosponges ( $n = 2, 6, 10$ ) after subtraction of QE contribution in the energy range 0–200  $\text{cm}^{-1}$ .

The behaviour of  $\omega_{BP}$  observed for  $\alpha$ -CDEDTA1n nanosponges in Fig. is consistent with the change in the elastic properties of these systems, which appears to show a maximum in the stiffness of the polymeric matrix corresponding to  $n = 6$ .

This result can be further confirmed by the analysis of the shape of the BP as a function of molar ratio  $n$ , which is achieved by rescaling the frequency axis of the Raman spectra in terms of  $u = \omega/\omega_{BP}$ . To this aim, in order to warrant the invariance of the density of vibrational states of the materials, it is put  $g(\omega)d\omega = g(u)du$ . [44]

Accordingly, the change of  $x$  variable from  $\omega$  to  $u$  imposes that also the reduced Raman intensity must be rescaled through the relation [44]

$$I(u(\omega)) = I^{Red}(\omega) \times \omega_{BP}^2$$

The so-rescaled spectra reproducing the Raman spectra and the profile of the resulting vibrational components, obtained after subtraction of the QE contribution, are shown in Fig. (a) and (b), respectively, for  $\alpha$ -CDEDTA1n nanosponges. The values of  $\omega_{BP}$  used to rescale both the frequency and the intensity of the spectra were preliminarily estimated by using the data fitting procedure based on the above equation.

It is worth noticing that, within the experimental error, the spectra corresponding to different samples of EDTA nanosponges are perfectly overlapped, collapsing into a single master curve, clearly evident in both the panels of Fig.. It should be pointed out that its master curve is obtained without any adjustable parameter.

The existence of a master curve for BP, in agreement with the results obtained on other glass-former systems, [42, 44, 47, 48] gives evidence that the spectral shape of the BP is essentially the same for the three different types of  $\alpha$ -CDEDTA1n nanosponges. This finding is consistent with the conclusion that the transformation of BP is only determined by the changes occurring in the elastic properties of the material, independently of the modifications of the microscopic structure of the sample.

Finally, Fig. 24 shows the evolution of  $\omega_{BP}$  for the two different types of nanosponges obtained by polymerization of  $\alpha$ - and  $\gamma$ -CD with the cross-linking agent EDTA as a function of the parameter  $n$ . The plots show a similar dependence on  $n$  of the stiffness of polymeric network with a maximum of the rigidity of the systems which corresponds to a six-fold excess of cross-linker EDTA with

respect to the monomer  $\alpha$ - or  $\gamma$ -CD. This finding is in agreement with the behavior observed for other cyclodextrin-based polymers obtained by polymerization of  $\beta$ -CD with the same crosslinking

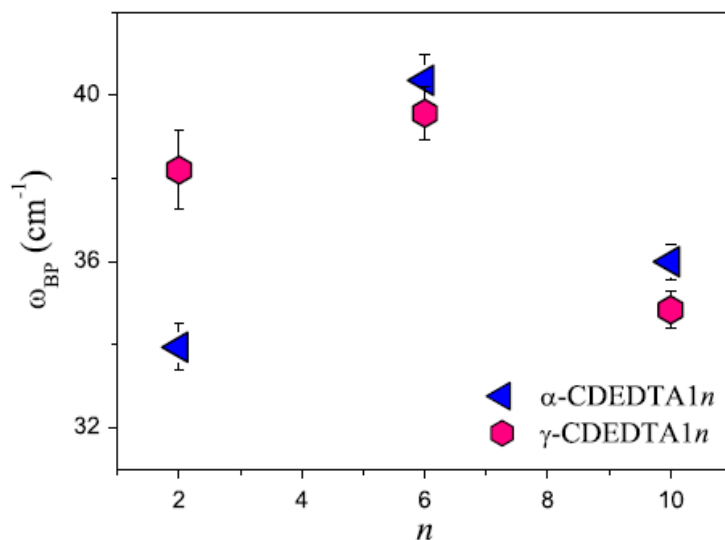


**Figure 23: Evolution of  $\omega_{BP}$  as a function of the molar ratio  $n$  for different types of EDTA nanosponges:  $\alpha$ -CDEDTA1n (blue left triangles) and  $\gamma$ -CDEDTA1n (pink hexagons).**

agent EDTA [15] and with pyromellitic dianhydride (PMA), in dry [1, 7, 14] and hydrated state. [16] In fact, in all these systems, a triggering of stiffness and cross-linking degree (i.e., connectivity) was systematically observed in correspondence of the molar ratio  $n = 6$ . The rationale of this experimental finding could rely on two competing effects, as schematized in Fig. : on one side, the cross-linker molar excess boosts the reactivity, leading to reticulation and formation of three-dimensional network mediated by both covalent bonds (ester linkages) and non-covalent interactions (hydrogen bonds). Otherwise, beyond a six-fold excess of EDTA or PMA, the addition of cross-linkers does not result in a further growth of the polymeric network but rather increases the branching of cyclodextrin units and introduces some destructuring effects, mainly of entropic nature, that do not favor the establishment of hydrogen bonds.

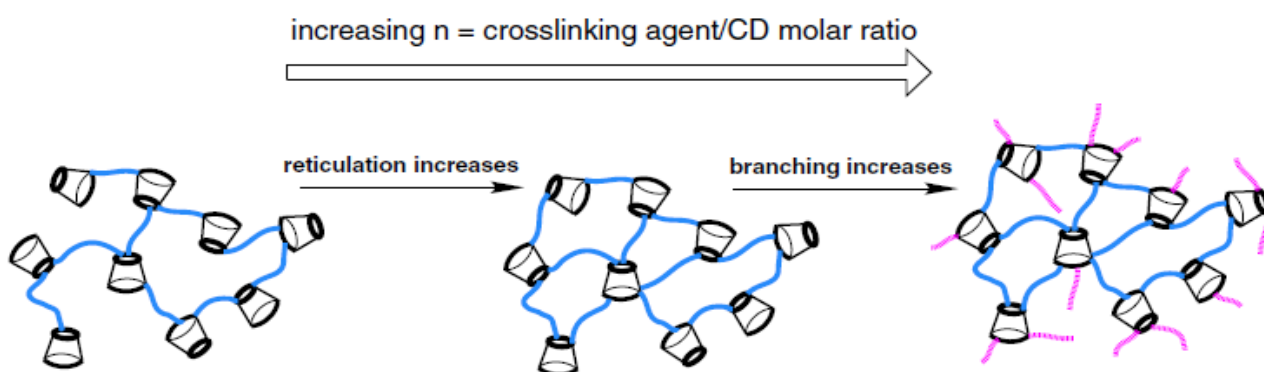


**Figure 24: Schematic picture representing the effect of increasing of the parameter  $n$  on the structural properties of CDNS polymer network.**

### 3.4.5. Conclusions

The evolution of the low-frequency vibrational spectra of cyclodextrin-based cross-linked polymers was here investigated as a function of the type of CD monomeric unit ( $\alpha$ - or  $\gamma$ -CD) and the relative amount of cross-linking agent with respect to CD. Significant changes in the intensity and frequency position of the boson peak were observed, mainly depending on the parameter  $n$ , in agreement with the results obtained on other cyclodextrin-based polymers. By using the BP maximum as a physical descriptor of the stiffness properties of the material, an upper limit in the rigidity of EDTA nanosponges polymeric network is found corresponding to a six-fold excess of cross-linker with respect to the monomer CD. This result confirms that the effect of saturation for the three-dimensional growth of the polymer is triggered for values of  $n > 6$ . Finally, the existence of a scaling law for the BP spectral shape was verified, supporting that the transformation of BP is only determined by the changes occurring in the elastic properties of the material.

# Chapter 4 – Paramagnetic Cyclodextrin based nanosponges

## 4.1. Aims of the chapter

After a rheological evaluation of cyclodextrin-based nanosponges observing their behaviour during the conversion in hydrogel, it was faced the study of paramagnetic cyclodextrin-based nanosponges from their synthesis to their analysis.

The synthesis of paramagnetic cyclodextrin-based nanosponges aims to design spin labeled systems through the use of nitroxyl radicals, in particular way TEMPO.

In fact the nitroxyl paramagnetic group is particularly versatile and finds application in different fields:

- As catode material for rechargeable lithium batteries
- As Magnetic Resonance (MR)/Electron Spin Resonance (EPR) contrast agent
- As Reactive Oxygen Species (ROS) scavenger

The synthesis of paramagnetic CDNS confers an high added value to our approach, allowing:

- The in vivo detection of CDNS nanoparticles by advanced diagnostic system
- The preparation of uniquely organic (metal free) soft materials moderately sensitive to magnetic fields.
- The application of CDNS as intrinsic and extrinsic ROS scavengers.

## 4.2. Radical TEMPO

Among nitroxyl radicals(2,2,6,6-tetramethylpiperidin-1-oxyl) radical, also known as TEMPO radical, and its derivatives, plays an important role. The biological application of TEMPO and derivatives has been intensely investigated in the last years by different authors as promoters of ROS metabolism and nitric oxide bioavailability. [1] Very recently Nagasaki and co-workers proposed different applications of nitroxide radicals. In particular, they produced polymeric micelles containing TEMPO radical moieties working at the same time as system for delivery of oligonucleotides and scavenger for the ROS generated by cells. [2] With a similar approach they prepared pH nitroxide radical-containing nanoparticles for ROS scavenging in renal ischemic regions. The nanoparticles were synthesized attaching tempo radical to poly(ethylene, glycol)-b-poly(methylstyrene) block copolymer via amine linkage. [3]

The same authors created blood compatible surfaces suitable for suppressing blood activation and coagulation using nitroxide radical containing polymers with ROS scavenging activity. [3]

TEMPO is a chemical compound with the formula  $(\text{CH}_2)_3(\text{CMe}_2)_2\text{NO}$ . [4] This heterocyclic compound is a red-orange, sublimable solid. It was discovered by Lebedev and Kazarnovskii in 1960 [5] and prepared by oxidation of 2,2,6,6-tetramethylpiperidine. TEMPO being a cyclic nitroxide compounds possessing bulky substituents is highly stable, unlike non-cyclic nitroxide radicals that are unstable chemical species similar to conventional radicals.

The stability of this radical so arises from the steric protection provided by the four methyl groups adjacent to the nitroxyl group. The methyl groups prevent a double bond occurring between nitrogen and the carbon adjacent. [6] Additional stability is attributed to the resonance provided by non-bonding electrons on the nitrogen atom and hyperconjugative ability. The stability of the radical is also indicated by the weakness of the O-H bond in the hydrogenated derivative TEMPO-H. With an O-H bond dissociation energy of about 70 kcal/mol, this bond is about 30% weaker than a typical O-H bond. [7]

TEMPO can be also sublimated without decomposition. [8]

Because of its moderate stability and reactivity, TEMPO is so employed in organic synthesis as a catalyst for the oxidation of primary alcohols to aldehydes and is, thus, known as versatile catalytic reactant.

Oxidation of TEMPO gives oxoammonium cations and TEMPO is reduced to hydroxylamine, as shown in Fig. 25: these are facilitated by “boat and chair” conformational changes that underlie the rapidity and catalytic nature of the reactions.

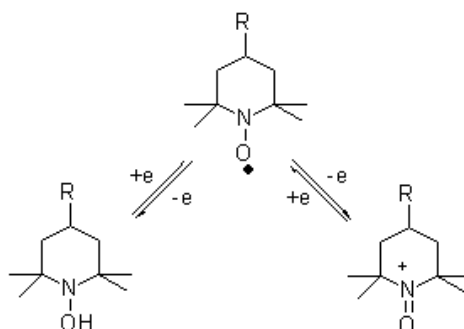
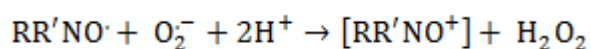
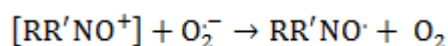
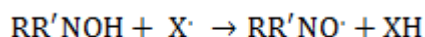
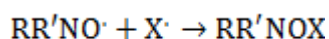


**Figure 25: Redox reaction of nitroxide radical.**

Both TEMPO and its oxoammonium cations can react with superoxide according to the following equations.



Both TEMPO and hydroxylamine react with radical species according to the following equations



Thus, TEMPO behaves like SOD (super oxide dismutase, an antioxidant protective enzyme) and scavenges ROS effectively. This ability to participate in redox reactions is the reason for nitroxide compounds being used for protection against oxidative damage in several models, ranging from models of cell systems to isolated organs to whole animals.

### 4.3. Cathode Material for rechargeable lithium batteries

#### 4.3.1. Requirements for electrochemical performance

All the organic molecules that can undergo a reversible electrochemical redox reaction are a possible candidate electrode material for energy storage.

Based on each structure listed in Table 4, large amount of organics can be designed and synthesized.

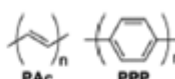
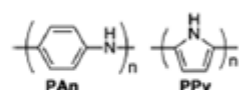
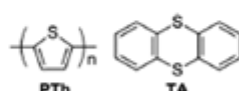
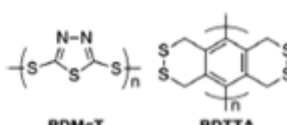
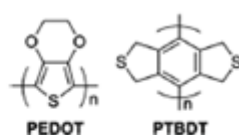
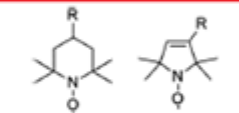
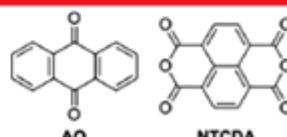
Structure	Redox mechanism	Examples
Conjugated hydrocarbon	$(R)_n^{x+} \leftrightarrow (R)_n \leftrightarrow (R)_n^{y-}$	 PAc      PPP
Conjugated amine	$R-\overset{+}{N}(H)-R \leftrightarrow R-\overset{-}{N}(H)-R$	 PAn      PPy
Conjugated thioether	$R-S^+-R \leftrightarrow R-S-R$	 PTh      TA
Organodisulfide	$R-S-S-R \leftrightarrow R-S^+ + ^-S-R$	 PDMcT      PDTTA
Thioether (4e)	$R-\overset{O}{S}-R \leftrightarrow R-\overset{O}{S}-R \leftrightarrow R-S-R$	 PEDOT      PTBDT
Nitroxyl radical	$R-\overset{O}{N}-R \leftrightarrow R-\overset{O}{N}-R \leftrightarrow R-\overset{O}{N}-R$	
Conjugated carbonyl	$R-\overset{O}{C}-R \leftrightarrow R-\overset{O}{C}-R$	 AQ      NTCDA

Tabella 4: The structure and redox mechanism of various type of organic cathode materials

These materials have to meet different needs. Some basic requirements are here summarized:

- Reaction reversibility: reversibility means not only chemical reversibility, but also thermodynamic reversibility. It is an important factor determining the electrochemical polarization and rate capability of the electrode material. The different reaction mechanisms in Table 4 show huge differences in reaction kinetics. Especially, nitroxyl radicals presents the highest reaction kinetics and always leads to high rate performance.



- Redox potential: Like the reaction reversibility, it is also mainly determined by the electroactive organic group or moiety. Different structures in Table 1 show huge difference in charge/discharge plateau or average charge/discharge voltage. In Fig. 26, the redox potentials of

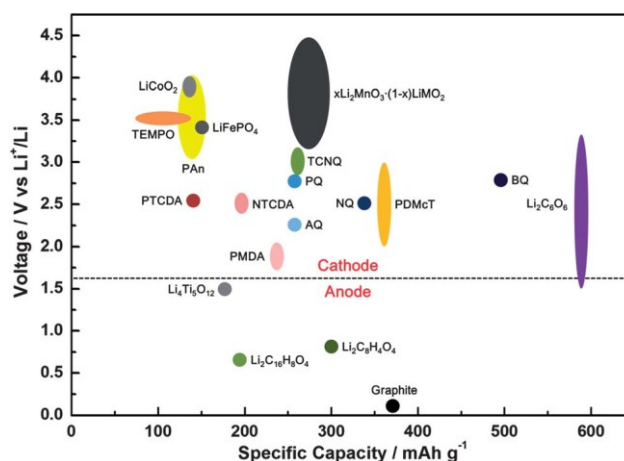


Figure 26: The redox voltage and specific capacity of typical inorganic and organic electrode materials for rechargeable lithium batteries. The structure of some organic can be found in Table 9

some typical organic electrode materials can be compared. Organics prefer to be applied as the cathode rather than the anode, since their redox potentials are usually between 2.0 and 4.0 V. [9, 10] For instance, nitroxyl radical TEMPO (only TEMPO<sup>+</sup>/TEMPO couple is utilized) and conducting polymer PAn always show a similar average charge/discharge voltage of about 3.5 V.

- Theoretical capacity: the theoretical specific capacity of an organic electrode material can be calculated by the following formula:

$$\begin{aligned}
 C_t(\text{mA h g}^{-1}) &= \frac{n \cdot F(\text{C mol}^{-1})}{M_w(\text{g mol}^{-1})} \\
 &= \frac{n \cdot 96485 (\text{C})}{M_w(\text{g})} = \frac{n \cdot 96485 (\text{A s})}{M_w(\text{g})} = \frac{n \cdot 96485 \cdot 1000/3600 (\text{mA h})}{M_w(\text{g})} \\
 &= \frac{n \cdot 26801}{M_w} (\text{mA h g}^{-1})
 \end{aligned}$$

In the formula,  $C_t$ ,  $n$ ,  $F$  and  $M_w$  respectively mean the theoretical specific capacity, the transferred electron number in each structural unit, the Faraday constant and the molecular weight of the structural unit. There is a huge difference in the theoretical capacity between

different types of organic electrode materials (Fig. 3). For example, TEMPO polymers can only achieve a theoretical specific capacity below  $140 \text{ mA h g}^{-1}$  because the monomer molecular weight is large, and only one electron (TEMPO<sup>+</sup>/TEMPO) can be reversibly transferred-in per structural unit.

#### 4.3.2. Nitroxyl radical as cathode material

In 2002, K. Nakahara et al. [11] first proposed a stable nitroxyl radical polymer, 4-methacryloyloxy-TEMPO(PTMA) (fig. 27), as cathode material for rechargeable lithium batteries.

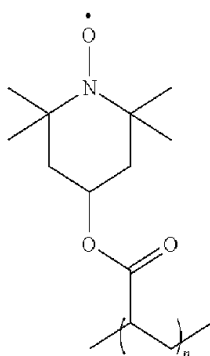


**Figure 27: PTMA: poly(2,2,6,6-tetramethylpiperidine-1-oxyl-4-yl methacrylate)**

In Table 4, the reaction mechanism of nitroxyl radical indicates it is a bipolar organic, Fig. 28 (a) and (b) show the typical battery performance of PTMA, which is the most studied among various nitroxyl radical polymers due to its sufficient stability and relative high capacity. The charge/discharge plateau is very flat at 3.5 V and the utilization ratio is close to 100%. The cycling and rate performance of PTMA are also excellent due to the stable polymer structure and fast reaction kinetics of the radical. Other TEMPO based polymers always show similar electrochemical behavior but different specific capacity. The greatest strength of nitroxyl radical polymers is their high rate performance. If the electrode is well fabricated, TEMPO based polymers can easily sustain a current rate of 20 C or 50 C. This arises mainly from the fast electron self-exchange reaction between adjacent TEMPO units (Fig. 28 (c)), which result in the efficient electron transfer despite the insulating polymer main chain.

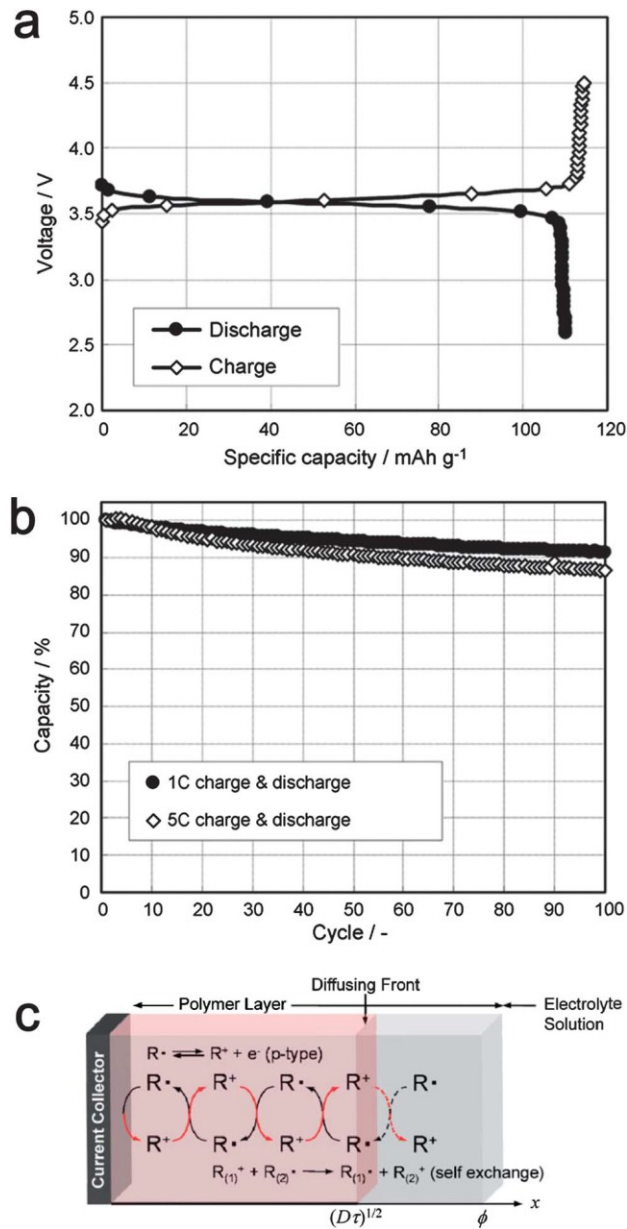


Figure 28: a) Typical charge/discharge curves and (b) cycling and rate performance of PTMA as the cathode material for a rechargeable lithium battery. Copyright © 2006 Elsevier. (c) The electron transfer process in a radical polymer electrode.

#### 4.4. MR contrast agent

The contrast agents are substance used to enhance the contrast of structures or fluids within the body in medical imaging. It is commonly used to enhance the visibility of blood vessels and the gastrointestinal tract. Specifically they alter the contrast of an organ, of a lesion, or of any other structure than that which surrounds it, in order to make visible details that would otherwise be not appreciable. [14]

Contrast agents are used mainly in the field of diagnostic radiology (traditional radiology, angiography) or magnetic resonance imaging. They have not to be confused with radiopharmaceuticals, radioactive substances used in nuclear medicine for functional studies.

##### 4.4.1. Magnetic Resonance Imaging

Unlike Radiography and computer tomography (CT), where the magnitude of the signal is proportional to the density and the atomic weight of the atoms that make up the target tissue, in the MR the parameters that affect the signal are related not only to the proton density but especially to the proton relaxation. [15] This has made possible to develop products that can significantly increase the contrast between normal tissue and pathological tissue even at very low concentration , because MRI contrast media affect the relaxation times T1 and T2 of the protons arranged in their adjacency. In this way a single molecule of contrast medium exerts an action favoring the relaxation on a large number of protons, thus requiring concentrations much lower than those needed in diagnostic CT. The contrast agent in MR are constituted by atoms or molecules with different action , not only can increase the signal (positive contrast agents) but also to lower (negative contrast agents). These effects are obtained by locally modifying the properties of the magnetic field using ferromagnetic substances , diamagnetic or paramagnetic.

The most important parameter that characterizes a contrast agent for magnetic resonance imaging is the relaxivity, which quantifies the change induced in the T1 or T2 as a function of concentration. In a constant magnetic field , the relaxivity is defined as follows:

$$\frac{1}{T_{1/2}} = \frac{1}{T_{1/2,0}} + r_{1/2}C$$

where  $T1 / 2$  indicates the resulting T1 or T2,  $T1 / 2,0$  indicates the T1 or T2 of the original tissue,  $r$  is the relaxivity and  $C$  is the concentration of contrast medium in the tissue. The relaxivity varies with the magnetic field, with a non-linear "bell", that presents a peak for a particular field value and is lower than in the rest of the cases.

#### 4.4.2. Nitroxyl radicals as MR/EPR contrast agent

Paramagnetic nitroxyl radicals have been proposed as redox-sensitive MR contrast agents. [16,17] The time sequence of T1-weighted MR images at 4.7 T showed readily visible enhancement of image intensity due to paramagnetic nitroxyl contrast agents and then sequentially showed gradual decrement of the image enhancement level. [16,17] The decrement of T1-weighted image enhancement is due to reduction of the nitroxyl radical form to the corresponding hydroxylamine form, which is a diamagnetic molecule. The decay rate of the signal enhancement level, that is, the reduction rate of the nitroxyl radical, is faster in tumor tissue than in normal tissue. This difference in the decay rate of the nitroxyl radical is ascribed to the difference of oxygen levels between the tumor and normal tissues.

Reoxidation of the hydroxylamine to the nitroxyl radical caused by normoxic normal tissue makes the decay rate apparently slow, On the contrary the reoxidation reaction is lower under the hypoxic conditions in tumor tissue; therefore, the method can be a diagnostic tool for tumor hypoxia.

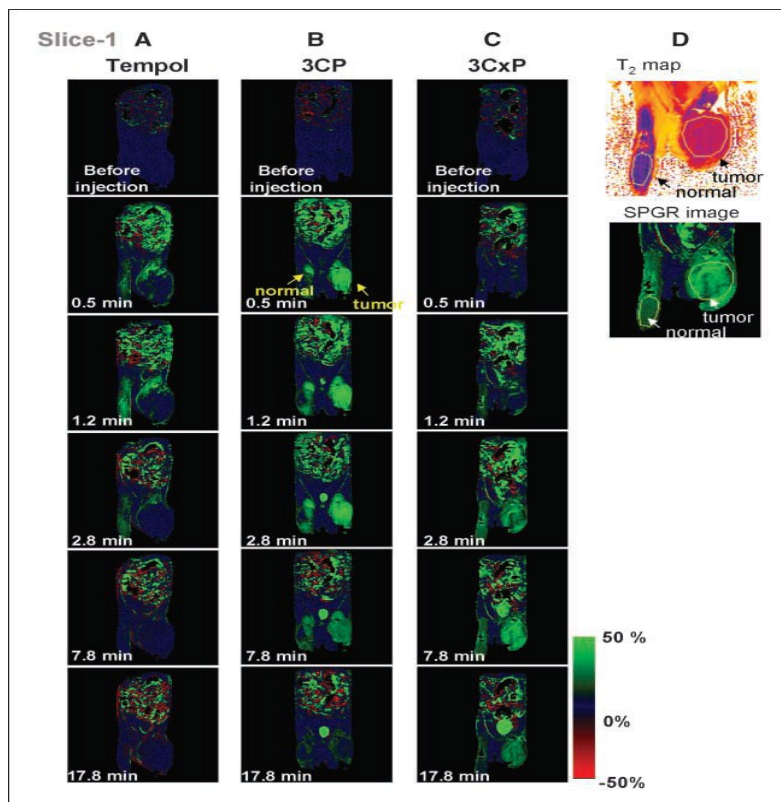


**Figure 29: Comparison of pharmacokinetic/redox images (slice 1) of three nitroxide contrast agents by SPGR MRI. Sixty serial images of Tempol (A), 3CP (3-carbamoyl-2,2,5,5-tetramethylpyrrolidine-1-Oxyl) (B), and 3CxP(3-carboxy-2,2,5,5,5-tetramethylpyrrolidine-1-oxyl) (C) were obtained during 20 minutes of continuous imaging. Slice 1, normal and tumor tissue area. Enhanced image intensity (%) against preinjection image by T1-weighted MRI (green). D, for T2 mapping, spin echo images were obtained using a MSME sequence with eight echo trains and 15-ms echo times.**

Although brain imaging is one of the main clinical applications of MR, clinically available BBB-permeable T1-shortening MR contrast agents are currently absent. Gadolinium-based contrast agents, cannot permeate BBB. Some lipophilic nitroxyl compounds have attracted increasing interest as BBB-permeable nonmetal contrast agents. In the field of in vivo EPR and MR imaging/spectroscopy, a nitroxyl contrast agent with high retention in the brain has been reported. [18]

R. Bakalova et. all [19] analyzed a stable nitroxy-radicals and magnetic resonance imaging. They synthesized a TEMPO-labelled analogue (SLENU) of the conventional anticancer drug Lomustine [1-(2-chloroethyl)-3-cyclohexyl-1-nitrosourea, CCNU]

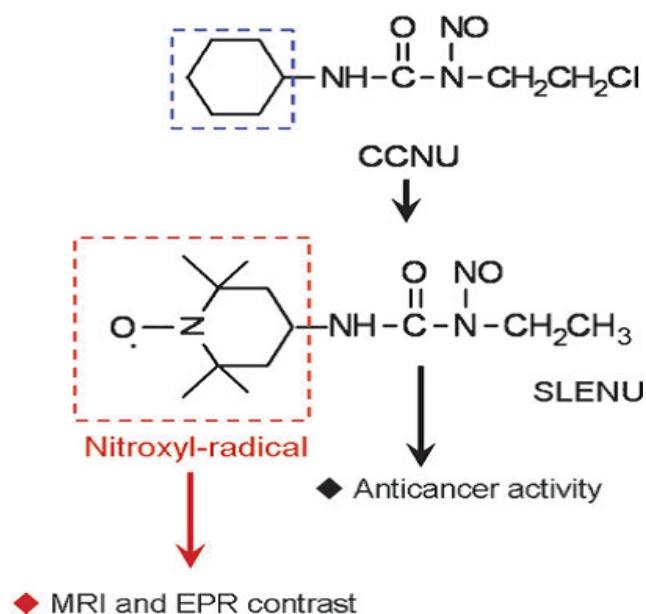
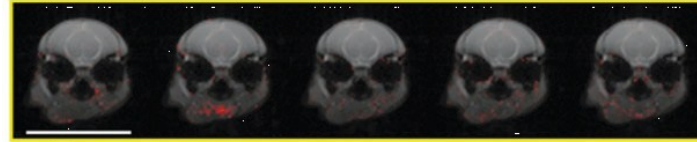


Figure 30: Lomustine (CCNU) and its nitroxyl labelled analogue (SLENU).

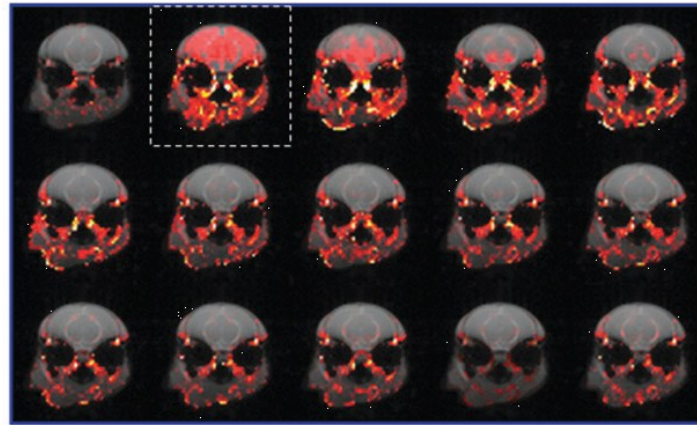
Lomustine significantly improves the health-related quality of life of patients treated for brain and other tumors. [20] Both TEMPO radical and Lomustine are permeable for BBB and cell membranes. [16, 21] Formally, the Lumustine molecule can be separated into two parts (Fig. 30). The nitrosoarea ensures the anticancer effect and should not be modified. The cyclohexyl part of the molecule was exchanged with TEMPO radical. This substitution did not influence the anticancer effect of the drug or its toxicological characteristics. [22,23] This study was designed to clarify whether the TEMPO-labelling of nitrosoarea will affect its BBB permeability and localization in the brain tissue and whether nitroxyl radicals were appropriate spin-labels of conventional drugs.

Before injection of SLENU



~20 sec

After i.v. injection of SLENU (0.8 mmoles/kg b.w.)



Time-decay of MRI signal  
(a histogram)

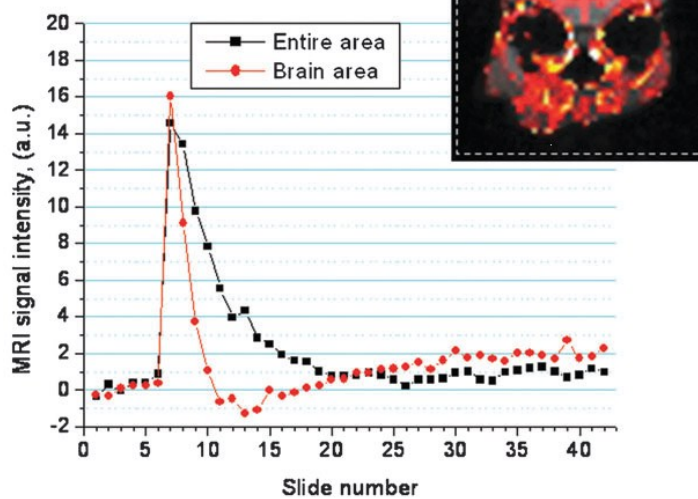


Figure 31: MRI signal dynamic of SLENU in the brain after intravenous injection in mice

This Fig. 31 shows the MRI signal dynamic of SLENU in the brain after intravenous injection in mice. Each image was obtained within a 20-s interval, using Gradient-echo T1-weighted MRI. In the image, the red colour represents an extraction of the signal between every single slide and the averaged baseline signal (first five slides – before injection). In the chart, the red and black colours represent an MRI signal dynamic in the brain or entire area, respectively.



Matsumodo et al. [24] noted the same behavior with the EPR technique. They compared N-PDT (4-oxo-2,2,6,6-tetramethylpiperidine-d16-1-N-oxyl), capable of permeating the cell membrane, with Oxo63, a triarylmethyl radical probe. Based on the free induction decay (FID) signal properties, NPDT was selected for the in vivo imaging studies. The pulsed EPR/SPI technique was applied to imaging the distribution of N-PDT in mice after intravenous administration and the result is shown in this figure 32.

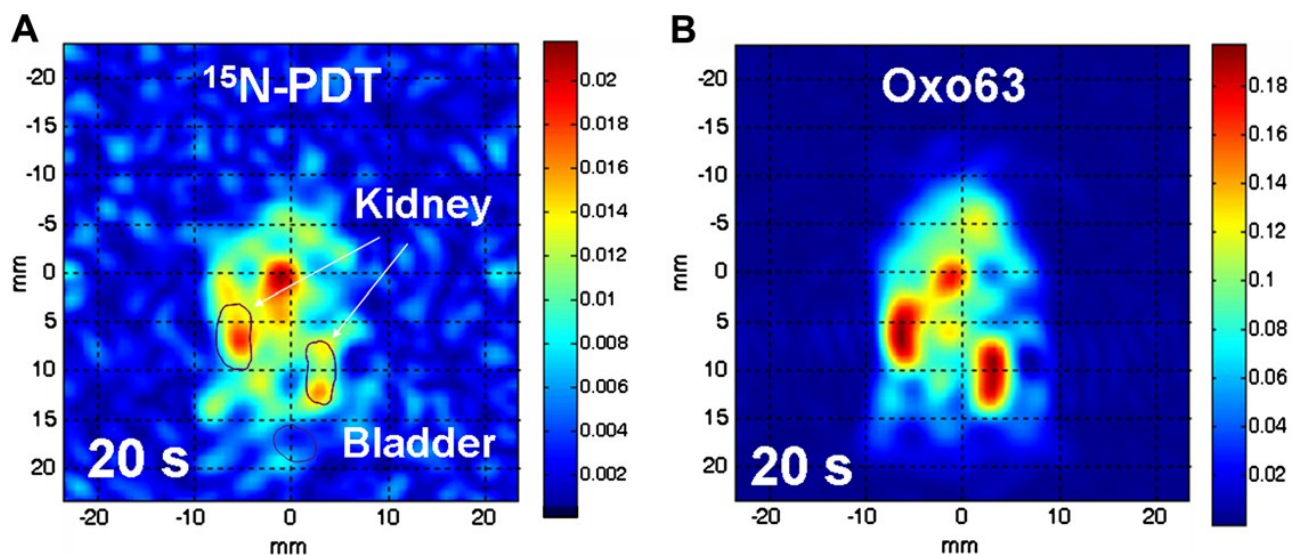


Figure 32: Pulsed EPR imaging of nitroxide in mice. (A) The first pulsed EPR image of nitroxide distribution in mouse. (B) Pulsed EPR image of Oxo63 injected into the same mouse after N-PDT signal disappeared.

The relatively fast in vivo paramagnetic loss of the nitroxyl contrast agents was unacceptable for the requirement of stable contrast agents at that time. Biologically stable Gadolinium-based contrast agents have a high T1 relaxivity, while nitroxyl-based contrast agents have not yet been used clinically: this represents a motivating challenge and also for this reason paramagnetic cyclodextrin-based nanosponges gain interest.

Recent interest in biofunctional imaging is again highlighting nitroxyl contrast agents as redox-sensitive and/or BBB-permeable MR contrast agents.

The relatively small T1 relaxivity of nitroxyl contrast agents makes it difficult to detect T1-weighted MR signal enhancement at low concentration levels. A higher magnetic field, such as 7 T, may increase the signal-to-noise ratio (SNR), while most clinical machines work in lower magnetic fields, such as 3 and 1.5 T or less.

The performance of multispin nitroxyl contrast agents was tested in order to improving the sensitivity of MR detection for nitroxyl contrast agents.

Several nitroxyl contrast agent with different number of spin in the molecule were synthesized: a good linear relationship was observed between T1-weighted image enhancement and the concentration of nitroxyl contrast agent: r1 (relaxivity T1) levels of nitroxyl contrast agents were increased depending on the number of nitroxyl spins in a molecule. [25]

The multi spin nitroxyl molecules can enhance the T1- weighted MR contrast effect: hence, for this last reason, a synthesis of cyclodextrin with more nitroxyl radical groups is particularly motivated.

## 4.5. ROS Scavenger

### 4.5.1. Reactive Oxygen Species

Atomic oxygen has two unpaired electrons in separate orbitals in its outer electron shell. This electron structure makes oxygen susceptible to radical formation. The sequential reduction of oxygen through the addition of electrons leads to the formation of reactive oxygen species. [26] Reactive oxygen species, known with the acronym ROS, are hence short-lived diffusible entities and are highly unstable and active towards chemical reactions with other molecules. This term, ROS, is used for molecules such as hydroxyl ( $\cdot\text{OH}$ ), alkoxy ( $\text{RO}\cdot$ ) or peroxy ( $\text{ROO}\cdot$ ) radicals and for some radical species of medium lifetime such as superoxide ( $\text{O}\cdot\text{O}_2$ ) or nitroxyl radical ( $\text{NO}\cdot$ ):

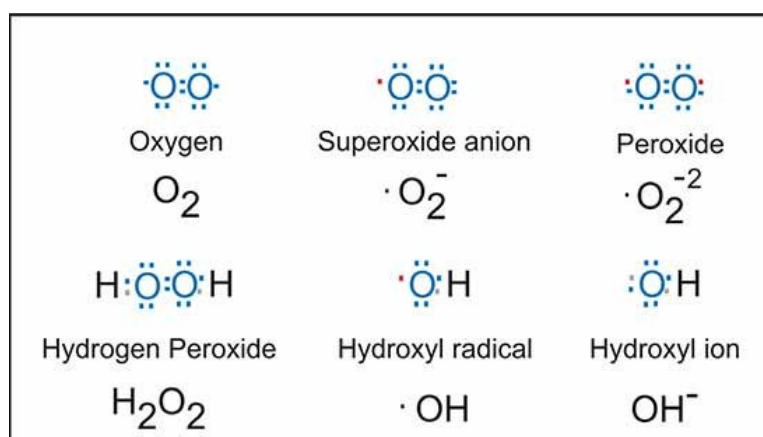


Figure 33: Electron structures of common reactive oxygen species. Each structure is provided with its name and

The excessive production of oxygen based radicals is the bane to all aerobic species. In fact, in aerobic organism, this reactive species are produced as a normal part of metabolism during the

mitochondrial electron transport of aerobic respiration or are formed as necessary intermediates of metal catalyzed oxidation processes. Their reactions (redox) are among the most important events in biological activity but an increase of ROS induces damage mainly on proteins, DNA e RNA molecules, sugar and lipids yielding to damages to cell structure and functions and causing an oxidative stress. An uncontrolled oxidative stress is involved in the origin and development of many pathologies, including chronic inflammation, cancer, atherosclerosis, renal lesion and the deposition of arterial plaque.

This overproduction of ROS can be promote by external factors like smoking, UV-light, exposition or environmental pollutant. [27, 28]

#### 4.5.2. State of the art for inhibitors and anti-oxidant molecules

A fundamental role in balancing free radicals inside the living organism is played by antioxidants (AO), a large class of both enzymatic and non-enzymatic substances that directly scavenge ROS or indirectly act to up-regulate antioxidant defences or inhibit ROS production. [29] Antioxidants are often reducing agents such as thiols, ascorbic acid, or polyphenols. The final balance between production and neutralization of ROS made by administration of specific AO acting as ROS level modulators (RLM) is hence a topic of high scientific interest. The literature evidences that, in general, antioxidant therapy has enjoyed relative successes in preclinical studies but little benefits in human intervention studies or clinical trials. In fact, despite the huge, largely untapped potential therapeutic benefit of natural phenolic antioxidants, such as vitamins, non-flavonoid and flavonoid compounds, they appear not to be suitable drug candidates. The main issue to be overcome during the administration of RLM is providing them into reliable and safe therapies because most AO show poor solubility and inability to cross membrane barriers.

In the last years, different antioxidant delivery systems have been engineered and biologically investigated: liposomes, polymeric micelles, magnetic nanoparticles, gold nanoparticles and electrospun fibres. In particular, delivery systems based on magnetic or gold nanoparticles are very interesting for nanomedicine application, being detectable in the target tissues by different techniques like magnetic resonance imaging (MRI). The main drawback associated with the biomedical application of inorganic nanoparticles is related with their over accumulation in brain,

liver and spleen. Moreover, it is known that iron oxide nanoparticles can induce oxidative stress by excess of ROS production. That reason shifts the interest on organic molecules. [30]

An interesting family of organic molecules that possesses both paramagnetic and antioxidant behavior are nitroxyl radicals. Numerous in vitro cell experiments have confirmed that nitroxyl radicals effectively scavenge ROS and regulate redox conditions, which improve cell viability and biofunctions. In fact nitroxyl radicals have the ability to react and/or interact with a free radical. They have been employed as a biophysical tool for many years. Owing to the ability of the radicals to degrade superoxide, inhibit Fenton reactions and undergo radical–radical recombination reactions, biological reactions involving these radicals have recently been used in novel therapies [31]

#### 4.5.3. Cyclodextrins as anti-oxidant molecules

As shown before, probably the biggest obstacle to overcome during the administration of RLM is the poor solubility of the most of AO. For these reasons, the design and production of polymeric vectors as biocompatible carriers, in a stable chemical form, with sufficient concentration and with reduced or, possibly, null adverse effect, is highly valuable. These vectors should combine:

- High and selective RLM delivery capability to the target tissue
- Possible intrinsic ROS scavenging activity
- Detectability by advanced diagnostic techniques
- Reduced bioaccumulation in the human body
- Biocompatibility

The use of cyclodextrins, a class of cyclic, non-reducing oligosaccharides having a well consolidated biomedical application as biocompatible drug carriers, fit with these requirements both in their simple form like “torus” and in their nanosponge form, using different and appropriate crosslinks.

The key aspect of this chapter is the introduction of a persistent radical (TEMPO) in a biocompatible carrier (CD) that would allow to produce paramagnetic nanodevices with a dual benefits:

- Introducing probes for both further characterization of nanomaterials by means of Electron Spin Resonance (ESR) and detection of nanoparticles in vitro and in vivo
- Introducing organic paramagnetic labels to rapidly vehicle nanoparticles in specific disease areas by application of mild magnetic fields

#### 4.6. Synthesis of fully organic paramagnetic CD (pmCD) bearing persistent nitroxyl radical

Paramagnetic cyclodextrins have been synthesized by two alternative approaches. The first approach is based on the one-pot random grafting of nitroxyl persistent radicals on the CD units: exploiting the same mechanism involved during the synthesis of nanosponges nitroxyl radicals are first linked to carboxylic acid anhydride moieties. The resulting product is then added to the solution of CD in anhydrous DMSO (or DMF) in presence of a base and a crosslinking agent. The addition of specific crosslinkers starts the polymerization leading to the final pmCDNS. This pathway doesn't allow the use on aqueous solvent. The second approach is based on the synthesis of cyclodextrins bearing one (or more) nitroxyl radical moieties at specific position on the glucopyranose ring through a "click reaction", giving a stronger bond than previous one. So paramagnetic cyclodextrin (pmCD) that can be crosslinked giving paramagnetic nanosponges (pmCDNS)

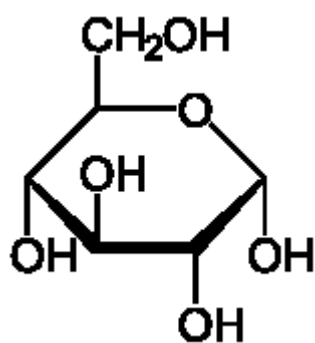


Figure 34: The glucopyranose ring

The main advantage in this second strategy are:

- The strict control on grafting position of the nitroxyl radical (generally but not exclusively, at C6 position of the glucopyranose ring)
- The obtained pmCDs can be crosslinked in both anhydrous and aqueous solvent to obtain the final pmCDNSs
- The copper-catalyzed azide-alkyne cycloaddition (CuAAC) reaction, coined as a “click reaction”, (9) has proven to be most powerful for ligating functional molecules to supporting scaffolds or to each other.

#### 4.7. Synthesis of CDNS through TEMPO anhydride

The one-pot random grafting of TEMPO radical on the CD units exploits an alcohol-anhydride mechanism, the same one seen during the nanosponge synthesis. In order to obtain this reaction it is necessary introduce an anhydride group into nitroxyl radical group affording a TEMPO anhydride, inasmuch as the alcohol group is represented by the hydroxyl group of CD at c6.

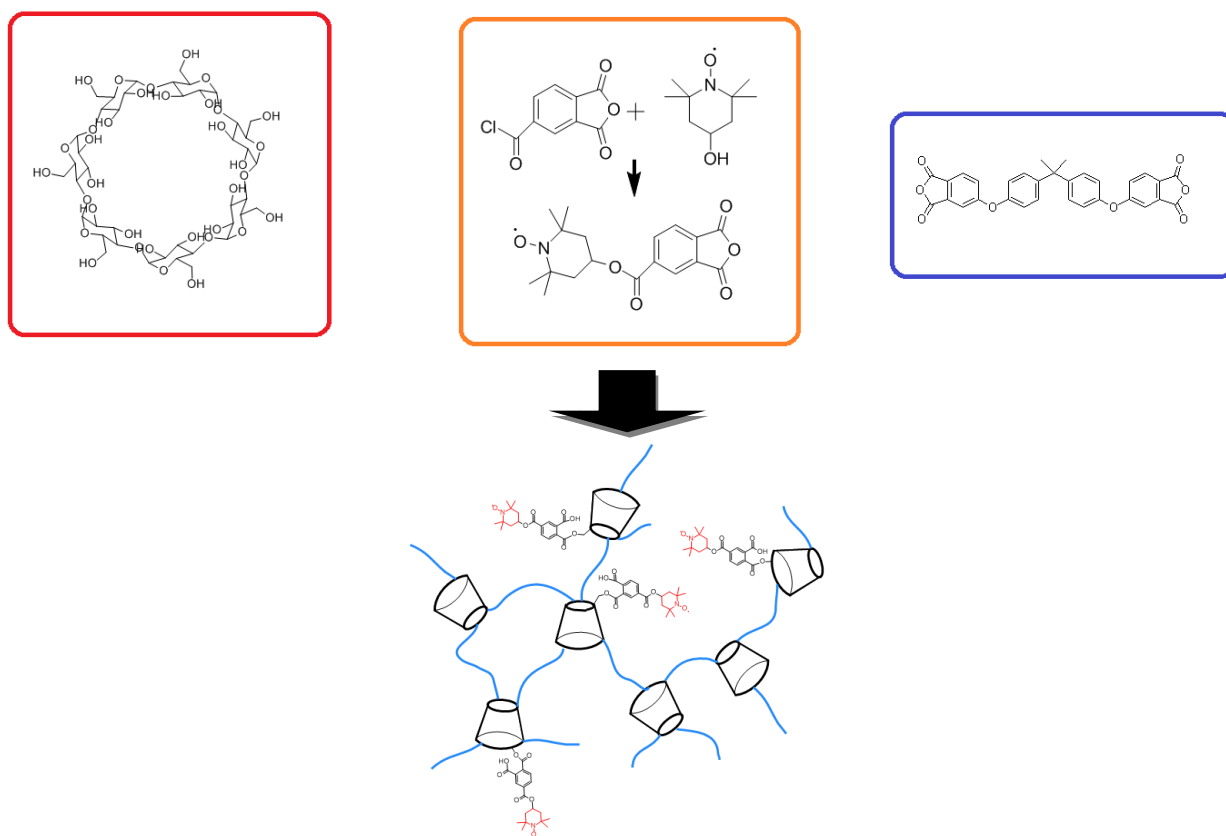
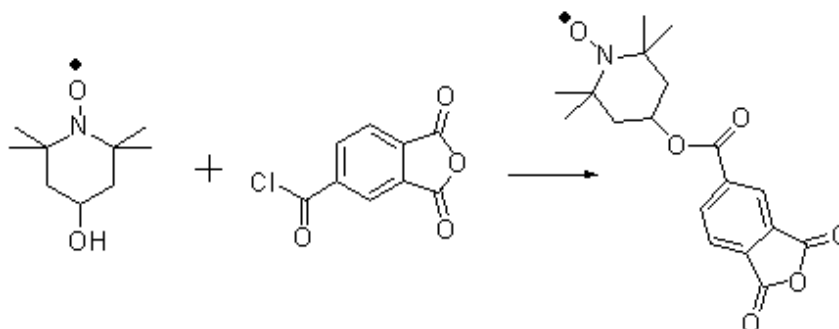


Figura 35: Synthesis scheme for CDNS through TEMPO anhydride

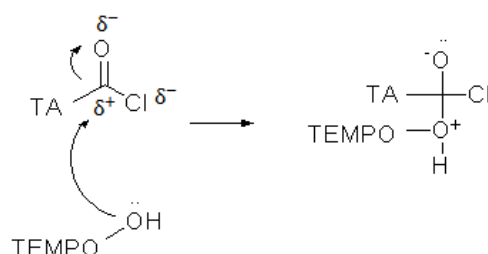
The TEMPO anhydride was obtained from the reaction between trimellitic anhydride chloride (TA) and 4-hydroxy TEMPO. The functionalization of CD with the nitroxyl group occurs under the same condition used for the synthesis of cyclodextrin based nanosponges. After then the synthesis of TEMPO anhydride, random TEMPO grafted based nanosponges was performed.

#### 4.7.1. TEMPO anhydride

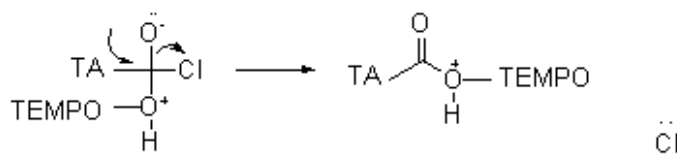
The mechanism involved during the synthesis of TEMPO anhydride is a nucleophilic addition/elimination in the reaction between the acyl chloride (TA) and the alcohols (4-hydroxy TEMPO).



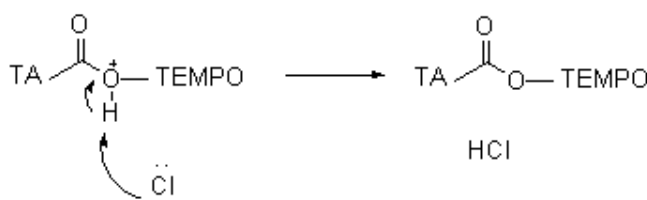
The first stage (the addition stage of the reaction) provides a nucleophilic attack on the fairly positive carbon atom by one of the lone pairs on the oxygen of the hydroxyl group of 4-hydroxy TEMPO.



The second stage (the elimination stage) occurs in two steps. In the first one, the carbon-oxygen double bond reforms and a chloride ion is pushed off.



The second one consist into the removal of a hydrogen ion by the chloride ion to give TEMPO anhydride and hydrogen chloride.



#### 4.7.1.1. Synthesis TEMPO anhydride

Trimellitic anhydride chloride TA (1.89 gr, 9 mmol ) was dissolved in anhydrous THF (20ml) under  $N_2$  atmosphere into a two-neck flask (100 ml). Then in another flask (100 ml), 4-hydroxy-TEMPO (1.46 gr, 8.5 mmol) was dissolved in anhydrous THF (20ml) with anhydrous  $Et_3N$  (3ml) and then added dropwise through addition funnel to the flask with TA solution in an ice bath over 1 hour at  $0^\circ C$  (exothermic reaction). The mixture was kept under stirring for 3 hours, and then the solvent was evaporated under reduced pressure. The orange solid was used without further treatment.

#### 4.7.2. Synthesis random grafted TEMPO cyclodextrin based nanosponge.

DMSO and  $Et_3N$  was anhydrificated on molecular sieves. In a flask (50 ml), anhydrous  $\beta CD$  (1 gr, 0.88 mmol) were dissolved in anhydrous DMSO. After complete solubilization, TEMPO anhydride (0.61 gr, 1.76 mmol – molar ratio 2:1 with CD) and  $Et_3N$  (1 ml) were added. The mixture maintained under magnetic stirring was stirred for 1 hour at room temperature under  $N_2$  atmosphere. This solution was pipetted into a flask (50 ml) containing a mixture of BFA (1.38 gr, 2.65 mmol – molar ratio 3:1 with CD) in anhydrous DMSO (3ml). An orange solid polymer was obtained in 15 minutes. The material was crushed in a mortar and washed with acetone in Soxhlet for 24 hours at reflux.



#### 4.8. Synthesis paramagnetic cyclodextrin through click reaction

The second approach aims to synthesize a paramagnetic cyclodextrin bearing a nitroxyl radical in a particular position of glucopyranose ring. This goal was obtained through two different approaches:

- A paramagnetic cyclodextrin was synthesized using a ratio TEMPO/CD = 1:1, aiming to obtain one TEMPO moiety for each CD
- All C6 positions of the glucopyranose ring were substituted by TEMPO, obtaining a ratio TEMPO/CD = 7:1.

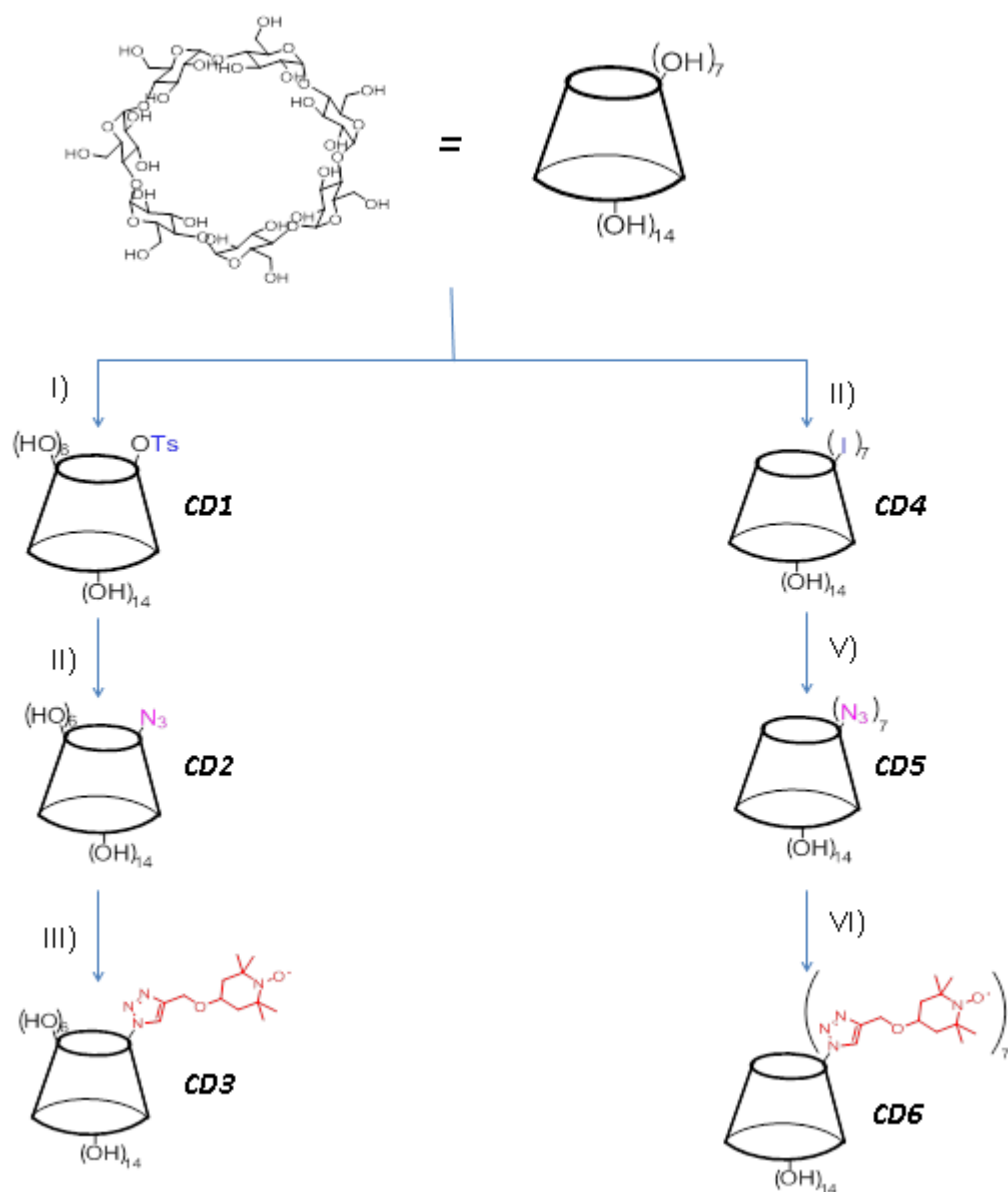


Figure 36: Synthesis scheme for functionalization of CD through Click Reaction

#### 4.8.1. First approach: Monofunctionalization of CD with nitroxyl radical

This synthesis requires different step of reaction in order to obtain the Mono 6 tempo 6 deoxy  $\beta$ Cyclodextrins. The link between the CD and the nitroxyl radical is given by a click reaction. To obtain a “click reaction”, in particular way a Huisgen cycloaddition, is necessary an azide group and a terminal or internal alkyne. For this reason an azide group has been introduced into a CD and an alkyne group to TEMPO in order to promote this molecular interconnection.

While, on one hand, the junction between TEMPO and the alkyne group is substantially one-pot, on the other part the connection between CD and the azide group requires an intermediate step: initially one C6 group of CD has been substituted by a tosyl group, a good substrate for substitution reaction, through a tosylation. Then tosyl group will be substituted, in turn, by one azide group obtaining a reagent for the Huisgen reaction following the scheme in Fig.37

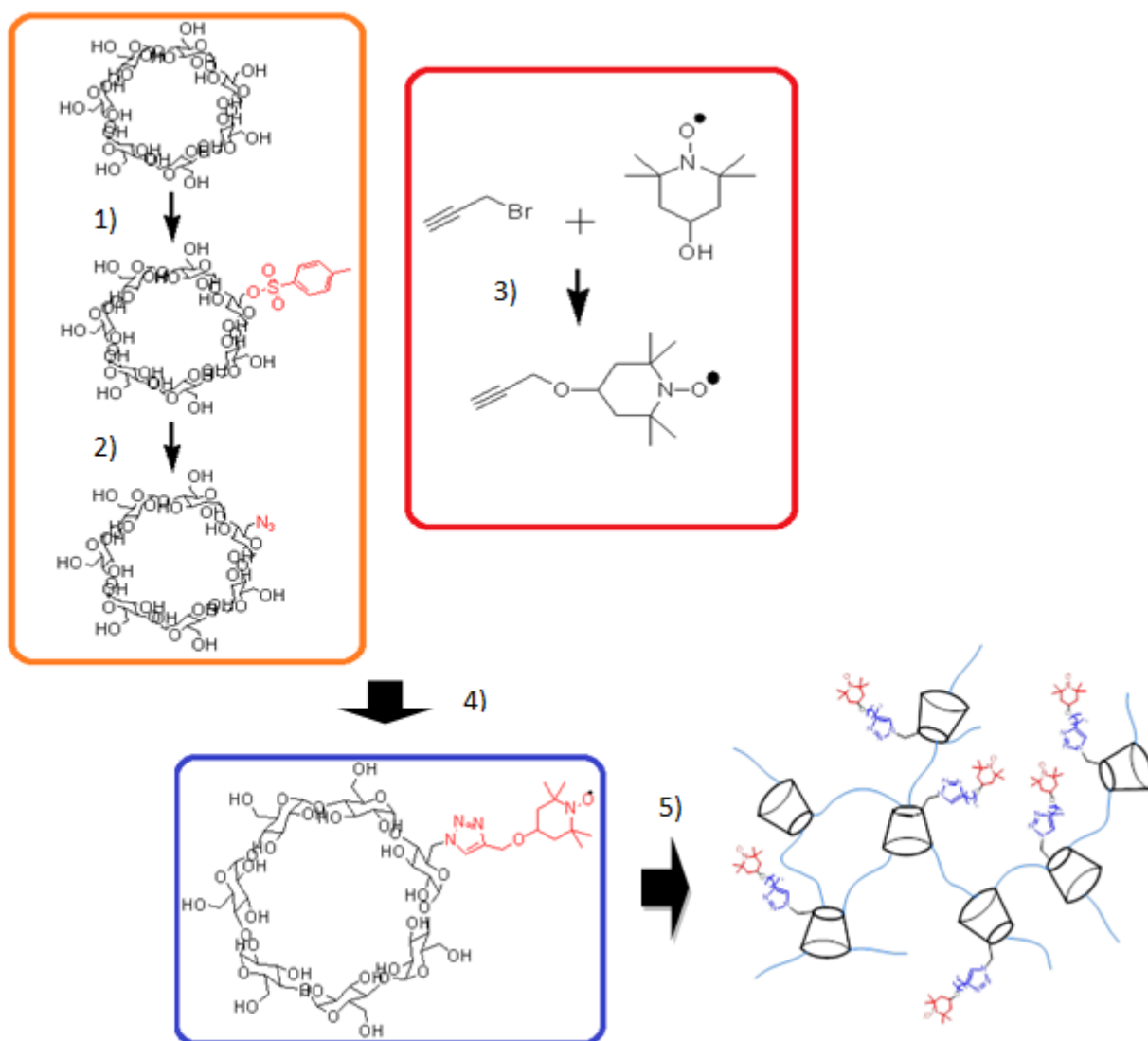
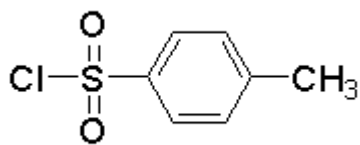


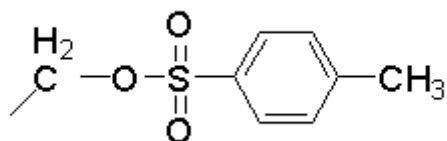
Figura 37: Synthesis scheme for Monofunctionalized cyclodextrin-based nanosponges

#### 4.8.1.1. First approach: Mono 6 - (p-tolylsulfonyl) -6-deoxy $\beta$ Cyclodextrins (CD1)

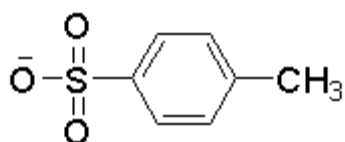
The tosylation of cyclodextrin expects a sulfonate ester bond between tosyl group and CD. In order to create this ester bond, a sulfonyl chloride is used as reagent. The reaction of tosyl chloride with an alcohol is easily represented by the standard nucleophilic substitution sequence, where the -OH reacts first as a nucleophile, attacking the electrophilic center of tosylate, displacing a chloride ion and finally giving a sulfonate ester called tosyl ester. Tosyl esters are good alkylating agents, rather like dimethyl sulphate, and show the presence of a good resonance stabilized leaving group: the tosylate anion. This is the conjugate base of p-toluensulfonyl acid, a strong acid ( $pK_a = -2.8$ , compared to hydroxide, the conjugate base of water,  $pK_a = 15.7$ ). For this reason, tosyl chloride can be used to facilitate nucleophilic substitutions.



p – toluensulfonyl chloride: This is the reagent used to prepare the tosylate ester.



p – toluensulfonyl ester: the oxygen atom from the original alcohol is retained.



Conjugate base of p-toluensulfonyl alcohol: in the reactions of tosylates, the displaced group is the resonance stabilized anion shown which is a good leaving group.

A way to convert the alcohol into its tosylate ester is using the tosyl chloride. Once obtained the ester undergoes a nucleophilic substitution leading to the formation of the corresponding azide derivatives. The advantage of this method is that the substitutions reactions are not under the strongly acidic conditions: This monofunctionalisation of C-6 can be achieved because in the presence of a base (e.g. NaOH), the proton at C-6 is removed to make O<sup>-</sup> which is a nucleophile

that can be easily substituted. Thus when a CD is reacted with a tosyl group in a basic medium, a monofunctionalised CD derivative (CDOTs) is afforded (10)

#### 4.8.1.1.1. Synthesis Mono 6 – (p-tolysulfonyl) -6-deoxy $\beta$ Cyclodextrins

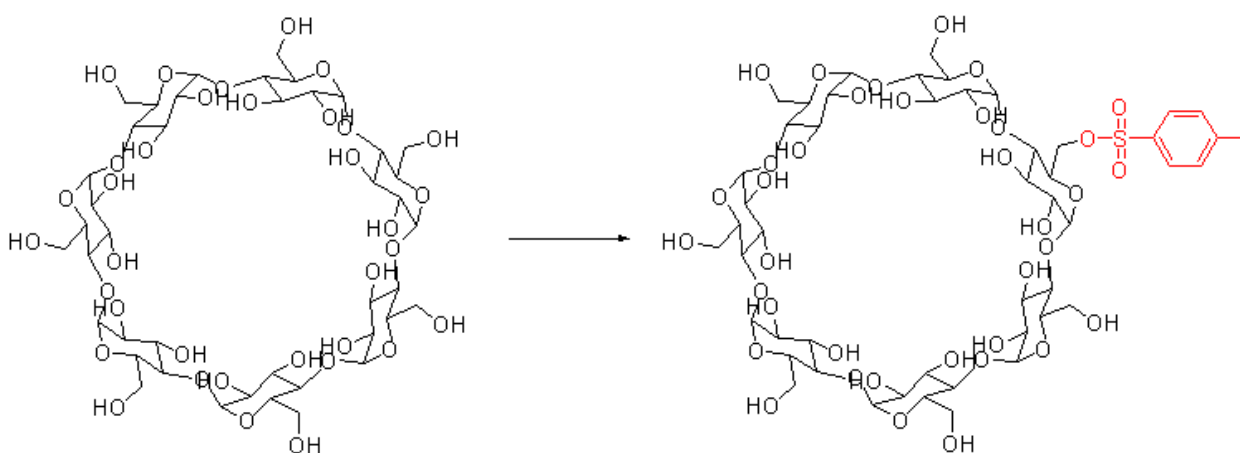


**Figure 38: Tosylation of  $\beta$ CD**

In a flask (500 ml) NaOH (5gr, 125 mmol) was dissolved in water (200ml). Then dry  $\beta$ Cyclodextrins (11.40 gr, 10.04 mmol) was dispersed in the basic water resulting a clear solution. The mixture was stirred vigorously and cooled at 0° C. Subsequently p-toluensulfonyl chloride (TsCl) (2.30 gr, 12.1 mmol) was ground in a mortar, added to the mixture and allowed to vigorous stirring at 0° C for 7 hours. The unreacted TsCl was isolated by filtration on sintered glass and the filtered was decanted in another flask at 0° C. After neutralization using 10 ml of HCl (37%), the crude product was isolated by filtration and washed with water. After TLC analysis, unreacted  $\beta$ Cyclodextrin ( $R_f$  = 0.25) was found. Another washing with water allow to obtain the Mono 6 – (p-tolysulfonyl) -6-deoxy  $\beta$ Cyclodextrins (1a) with also some of di-p-tosyl-  $\beta$ Cyclodextrins (1b).

Completed this check the solution was washed with acetone and allowed to stand overnight affording pure (3.793 gr, 34%).

TLC (2PrOH- H<sub>2</sub>O – EtOAc - NH<sub>4</sub>OH, 5:3:1:0.5)  $R_f$  = 0,45 (1a),  $R_f$  = 0.58 (1b)

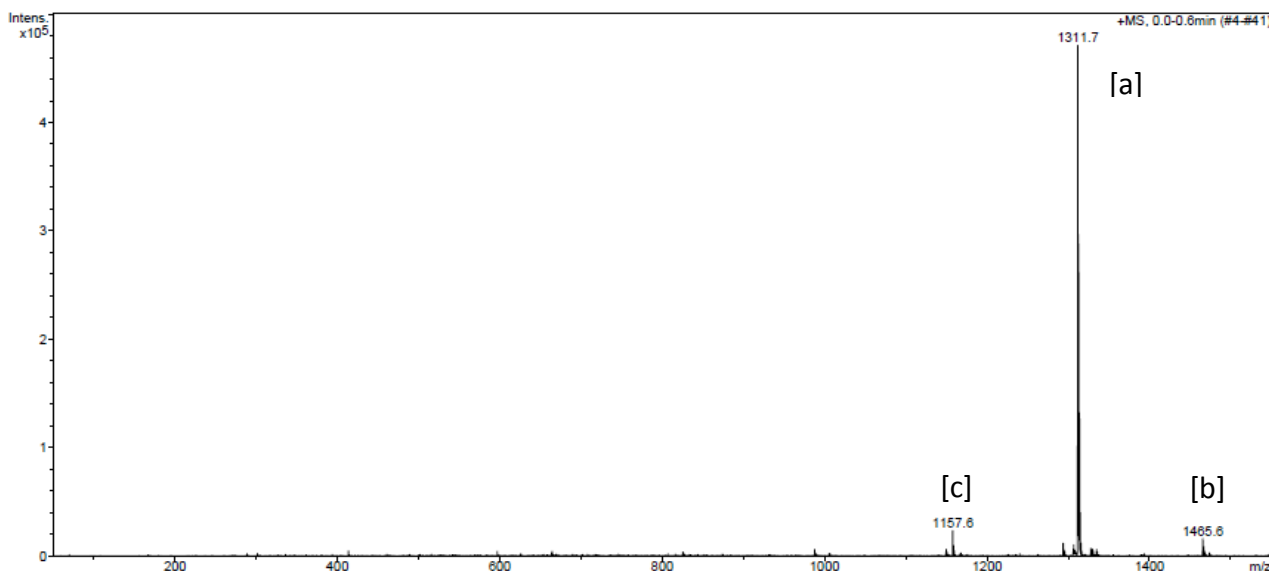


Figure 39: Esi-Mass of Mono 6 – (p-tolysulfonyl) -6-deoxy  $\beta$ Cyclodextrins

Esi-Mass:

- a)  $m/z = 1311.7$  (Mono 6 – (p-tolysulfonyl) -6-deoxy  $\beta$ Cyclodextrin +  $\text{Na}^+$ )
- b)  $m/z = 1465.6$  (Di 6 – (p-tolysulfonyl) -6-deoxy  $\beta$ Cyclodextrin +  $\text{Na}^+$ )
- c)  $m/z = 1157.6$  ( $\beta$ Cyclodextrin +  $\text{Na}^+$ )

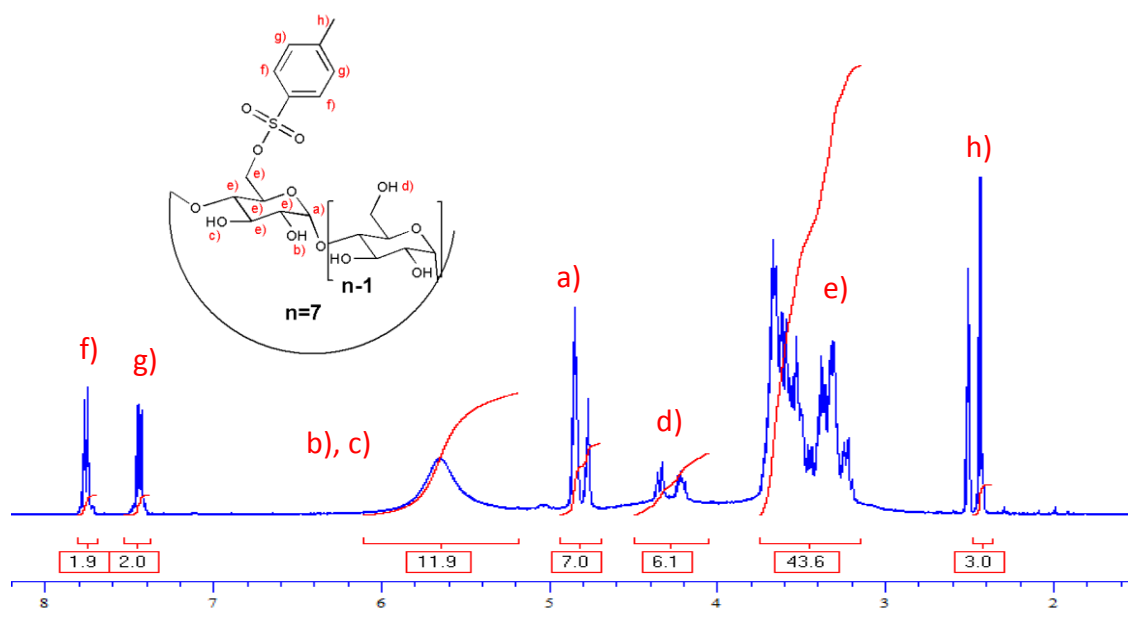


Figure 40: NMR spectrum of Mono 6 – (p-tolysulfonyl) -6-deoxy  $\beta$ Cyclodextrins

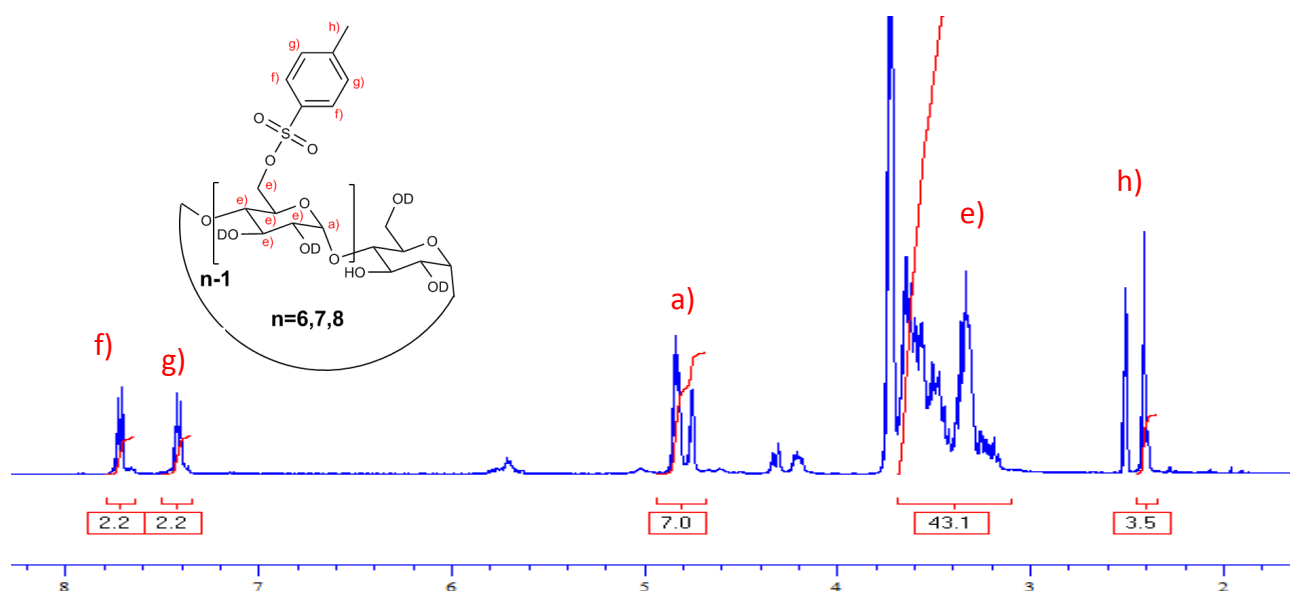


Figure 41: NMR spectrum of Mono 6 – (p-tolysulfonyl) -6-deoxy  $\beta$ Cyclodextrins treated with  $D_2O$

Treating the product with  $D_2O$ , the hypothesis were confirmed: in fact the hump found at 5.7 disappeared, like the peaks at 4.2 – 4.4, inasmuch as the hydroxyl group exchanged their hydrogens with the deuterium atoms of  $D_2O$ , becoming invisible at NMR spectrum.

#### 4.8.1.2. First approach: Mono 6-azido-6-deoxy- $\beta$ Cyclodextrins (CD2)

The tosyl group was removed by a nucleophilic substitution  $S_N2$  with  $NaN_3$  in order to obtain the Mono-6-azide-6-deoxy-  $\beta$ Cyclodextrins, the first reagent for the Huygen's cycloaddition

##### 4.8.1.2.1. Synthesis Mono 6-azido-6-deoxy- $\beta$ Cyclodextrins

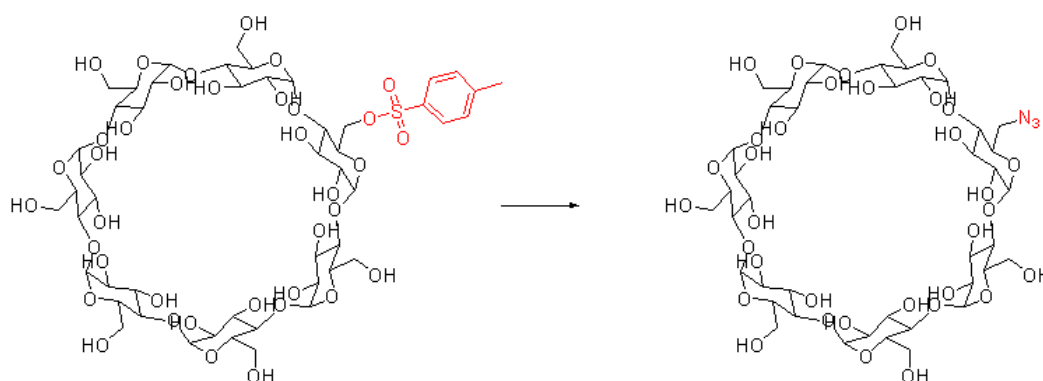


Figure 42: Substitution of tosyl group by azide group

In a flask of 100 ml mono 6-azido-6-deoxy-  $\beta$ Cyclodextrins (4.4 gr, 3.4 mmol) was dissolved in DMSO (20 ml). Then an excess of sodium azide (650 mgr, 10 mmol) was added to the mixture resulting a clear solution. The mixture was stirred vigorously at R.T. for 12 hours. After washing with acetone the precipitate was filtered obtaining the crude product. Then the product was dissolved in H<sub>2</sub>O and treated with ion exchange resins (IRA 400 Amberlist) in order to remove un reacted azide.

A test was performed in order to check the absence of unreacted azide: in a little vial, copper sulphate (CuSO<sub>4</sub>) was dissolved in water obtaining a blue solution, then 2 drops of mono 6-azido-6-deoxy-  $\beta$ Cyclodextrins dissolved in water was added into the vial. As copper is azaphilic, if some azide had been remained in solution, the color of this one would have turned yellow. On the contrary if the azide had been totally removed the color would not have changed. After three treatment with resins the color of the solution remained blue. Finishing this treatment, resins were separated by filtration and the mono 6-azido-6deoxy- $\beta$ cyclodextrins in the filtered liquid was separated by his solvent using rotavapor attending pure (quantitative yield)

TLC (2PrOH – H<sub>2</sub>O – EtOAc – NH<sub>4</sub>OH, 5:3:1:0.5) R<sub>f</sub> = 0.37

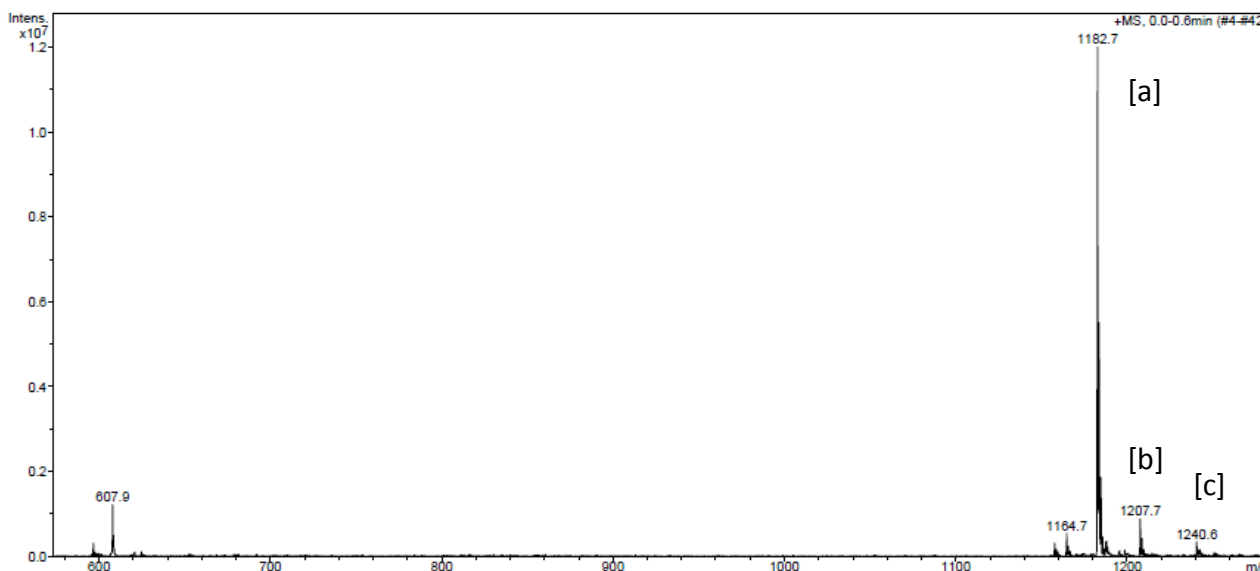
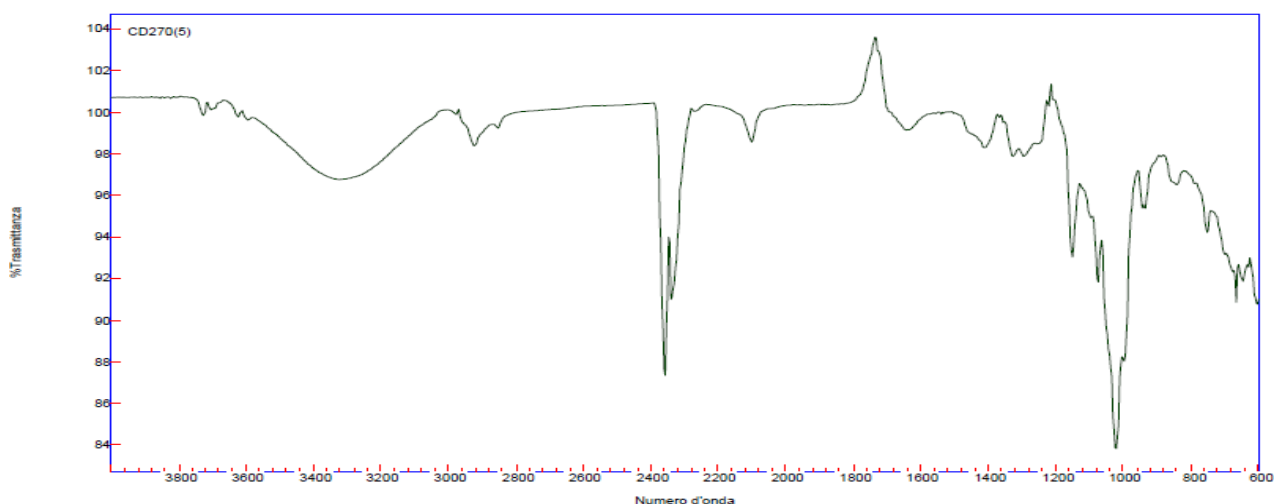


Figure 43: ESI-Mass of Mono 6 – (azide) 6 – deoxy  $\beta$  cyclodextrin

ESI – Mass:

- a)  $m/z = 1182.7$  (Mono 6 – (azide) 6 – deoxy  $\beta$  cyclodextrin + Na<sup>+</sup>)
- b)  $m/z = 1207.7$  (Di 6 – (azide) 6 – deoxy  $\beta$  cyclodextrin + Na<sup>+</sup>)
- c)  $m/z = 1240.6$  (Di 6 – (azide) 6 – deoxy  $\beta$  cyclodextrin + Na<sup>+</sup> + 2 H<sub>2</sub>O)



**Figure 44: IR spectrum of Mono 6 - (azide) 6 - deoxy  $\beta$  cyclodextrin**

Through an IR analysis, the presence of the azide was confirmed: in fact the peak at 2100  $\text{cm}^{-1}$  as wave number identified the stretching of the azide group. The peaks at 2350 were correlated at carbon anhydride in the air.

#### 4.8.1.3. First approach: Propargil – TEMPO

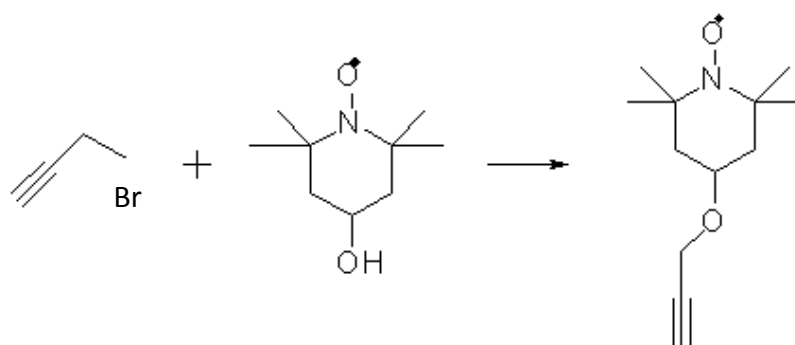


**Figure 45: Synthesis of Propargil - TEMPO**

In a two necked flask (100 ml), 4-Hydroxy-TEMPO (1.72 gr, 10 mmol) was dissolved in dry THF (40 ml) under vigorous stirring at 0 °C under inert atmosphere using  $\text{CaCl}_2$  valve. Then NaH (1g), prior treated with hexane to remove paraffin, was added to the mixture allowed to stirring for 2 hours resulting in the release of bubbles of  $\text{H}_2$ .



Finally Propargil Bromide (4.71 gr, 39,6 mmol), dissolved in THF (15 ml), was dropped through funnel into the flask; during this operation the funnel was covered by tinfoil in order to protect Propargil Bromide from sunlight. The mixture was allowed under vigorous stirring for 6 hours and then let stand overnight at R.T.

Water was slowly dropped into the dark solution obtained, with release of H<sub>2</sub>. At effervescence completed, the mixture was decanted in a separating funnel in ethyl acetate in order to separate the organic phase, lower layer, from aqueous one. This one was dehydrated on Na<sub>2</sub>SO<sub>4</sub>. This washing was repeated 4 times in order to remove water.

Through TLC the product was detected, purified on silica gel (hexane : ethyl acetate = 8:2) and isolated from his solvent using rotavapor, obtaining pure (1.826 gr, 0.86% mol)

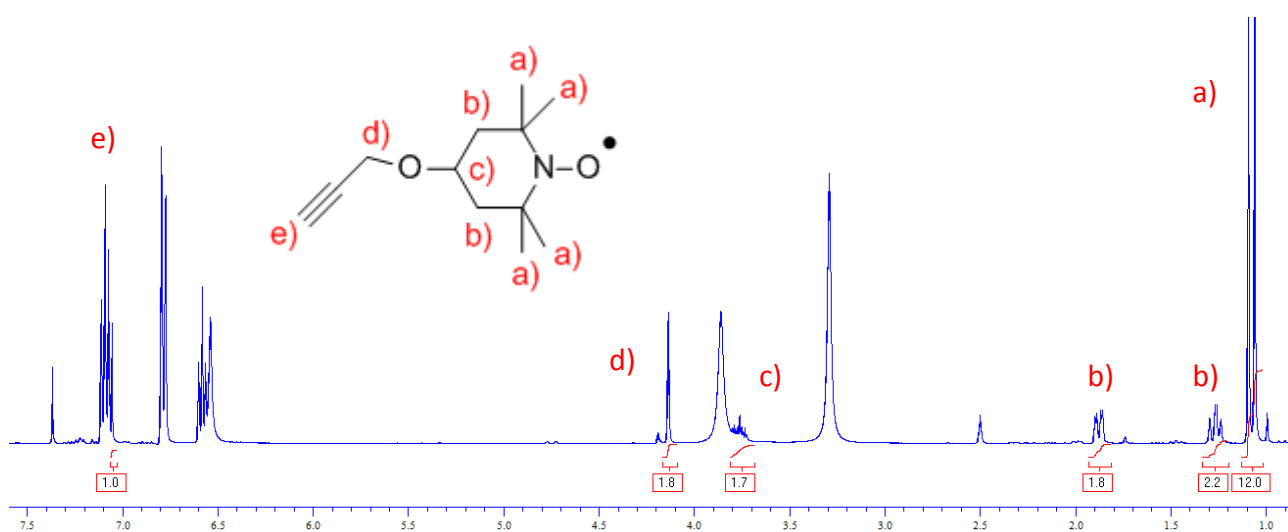


Figure 46: NMR spectrum of Propargil – TEMPO

#### 4.8.1.4. First approach: Mono-6-Tempo-6-Deoxy $\beta$ cyclodextrin (CD3)

In order to guarantee a paramagnetic aspect, and then antioxidant, CDs have been functionalized with a nitroxyl radical: this functionalization occurred through a “click reaction”, in particular way The Azide-Alkyne Huisgen Cycloaddition Huygens’ cycloaddition.

The Huigen’s cycloaddiction follows the mechanism represented in Fig. 47

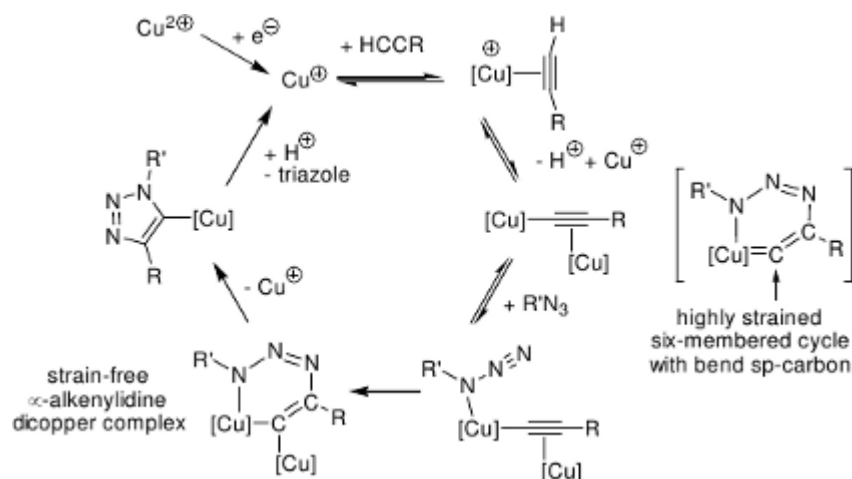


Figure 47: Mechanism of Huisgen Cycloaddition with Cu(I)

#### 4.8.1.4.1. Synthesis Mono 6 Tempo 6 deoxy $\beta$ Cyclodextrins

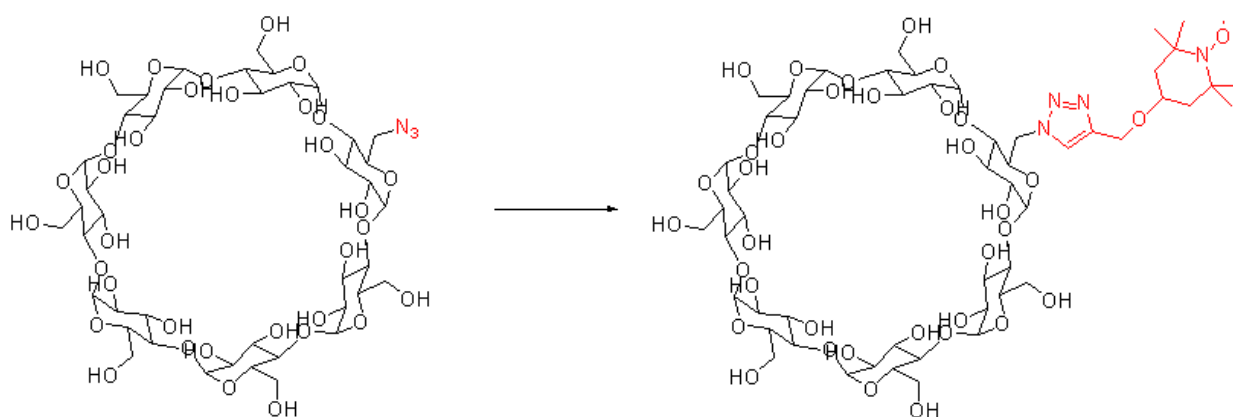


Figure 48: Click reaction on Mono 6 – (azide) 6 – deoxy  $\beta$  cyclodextrin

In a two necked flask (50 ml) into a bath oil, mono 6-azido-6-deoxy-  $\beta$ Cyclodextrins (1.160 gr, 1 mmol) is dissolved in DMF (5 ml) under stirring at 50 °C and then triethylamine (few drops) are added resulting an opaque solution.

Subsequently, under inert atmosphere, CuI (50 mg), the catalyst of the reaction, was added to the mixture: it's important keep CuI under  $\text{N}_2$  atmosphere in order to avoid the contact with oxygen that can oxide copper from the desired oxidation state (1) to 2.

The mixture was allowed to stir for 10 minutes, after then Propargil TEMPO is dissolved in the same flask resulting a reddish solution, so the flask is allowed to stir for 10 hours.

The crude product was precipitated in acetone and washed still in acetone in order to remove DMF through centrifuge.

Acetone was removed under vacuum from solution and TLC analysis showed the presence of Mono 6 Tempo 6 deoxy  $\beta$ Cyclodextrins and Di-Tempo- $\beta$ Cyclodextrins without impurities. On the other hand the presence of CuI cannot be showed using TLC and can give some problems during NMR analysis, so a silica column result necessary to purify the product. During separation, as eluent was used DMF adding some drops of  $\text{NH}_4\text{OH}$  in order to facilitate the adsorption of CuI on silica. A blue layer was observed during this procedure, which confirmed the presence and consequent separation of CuI from the product. The latter was washed again with acetone to remove DMF during chromatography, affording the product (1.209 gr, 86.5 % mol) TLC (2PrOH – H<sub>2</sub>O – EtOAc – NH<sub>4</sub>OH, 5;3;1;0.5) R<sub>f</sub> = 0,43 Mono, R<sub>f</sub> = 0.58 Di

In order to realize a NMR spectrum was necessary reduce mono 6 Tempo 6 deoxy  $\beta$ Cyclodextrins using phenylhydrazine in fact the presence of a stable radical interferes with the magnetic field of NMR hiding TEMPO's peaks: mono 6 Tempo 6 deoxy  $\beta$ Cyclodextrins (140 mg) was dissolved in DMSO in a flask of 25 ml. Then phenylhydrazine was dropped into the mixture under stirring releasing some N<sub>2</sub> bubbles that show the effect of the reduction. After 20 minutes other phenylhydrazine was dropped and no bubbles was released, so the reduction was completed.

Finally acetone was added to the reaction flask to precipitate the reduced cyclodextrin and remove phenylhydrazine and DMSO. The new product was obtaing through centrifuge. After this work up a complete NMR was possible.

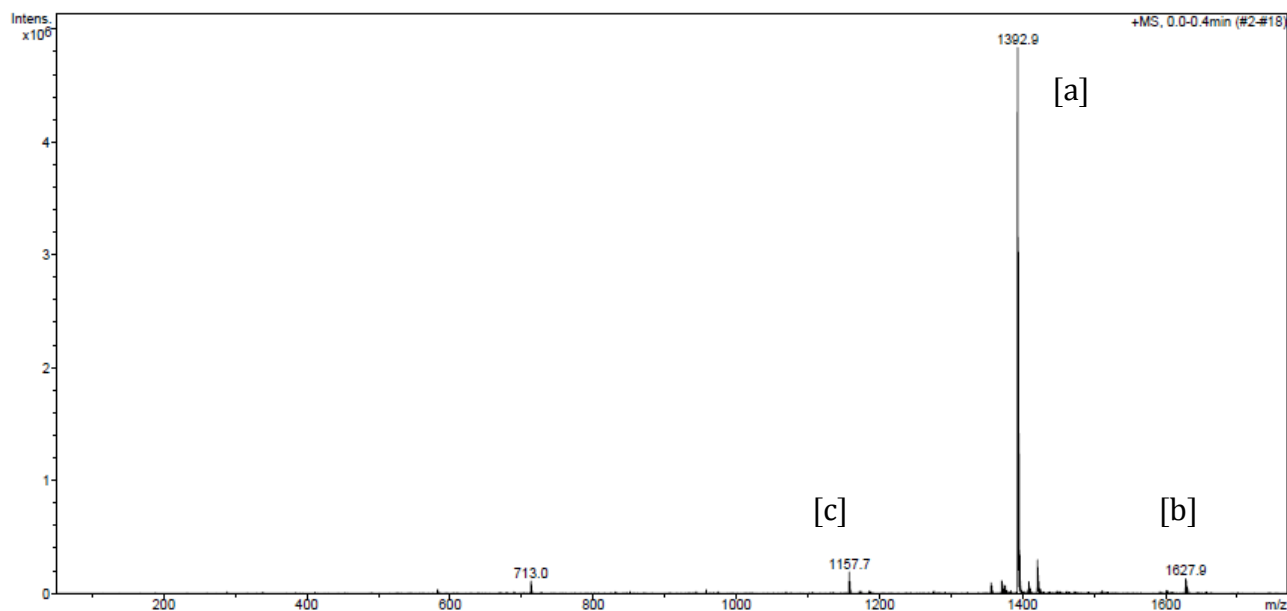


Figure 49: ESI Mass of Mono 6 – (TEMPO) 6 – deoxy  $\beta$  cyclodextrin

ESI-Mass:

- a)  $m/z = 1392.9$  (Mono 6 – (TEMPO) 6 – deoxy  $\beta$  cyclodextrin +  $\text{Na}^+$ )
- b)  $m/z = 1627.9$  (Di 6 – (TEMPO) 6 – deoxy  $\beta$  cyclodextrin +  $\text{Na}^+$ )
- c)  $m/z = 1157.7$  ( $\beta$  cyclodextrin +  $\text{Na}^+$ )

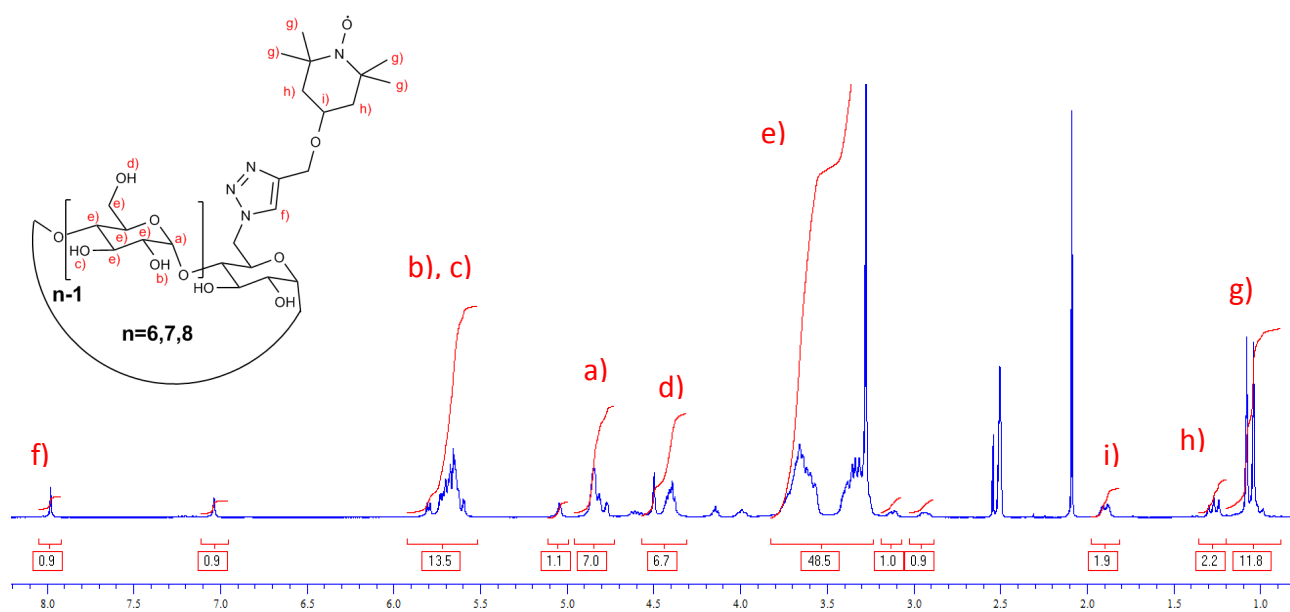


Figure 50: NMR spectrum of Mono 6 – (TEMPO) 6 – deoxy  $\beta$  cyclodextrin

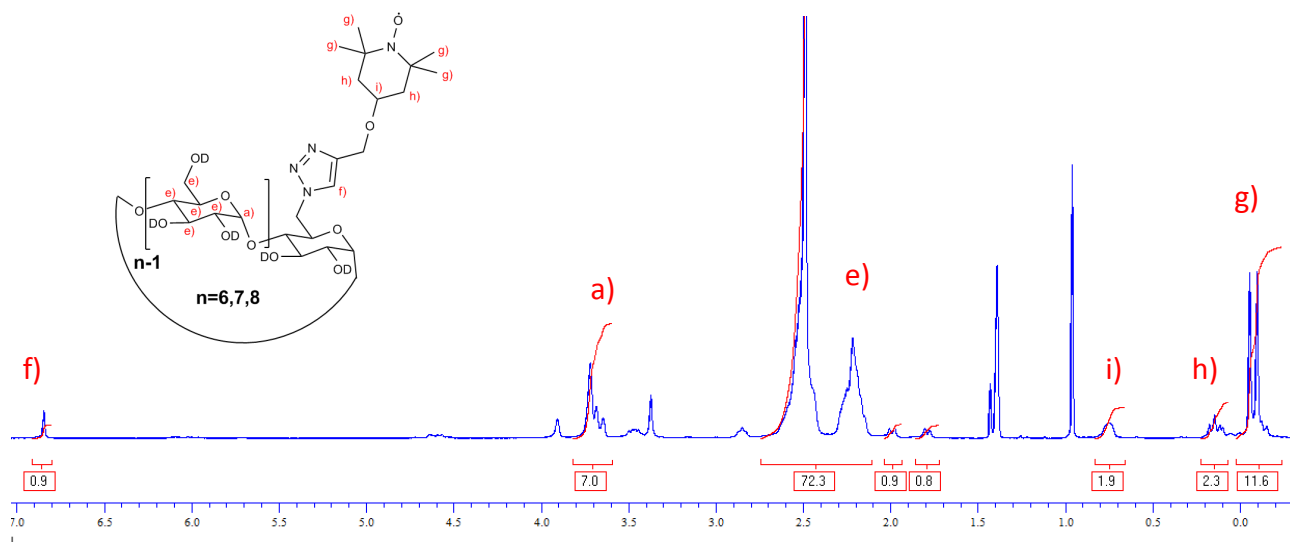


Figure 51: NMR spectrum of Mono 6 - (TEMPO) 6 - deoxy β cyclodextrin treated with D<sub>2</sub>O

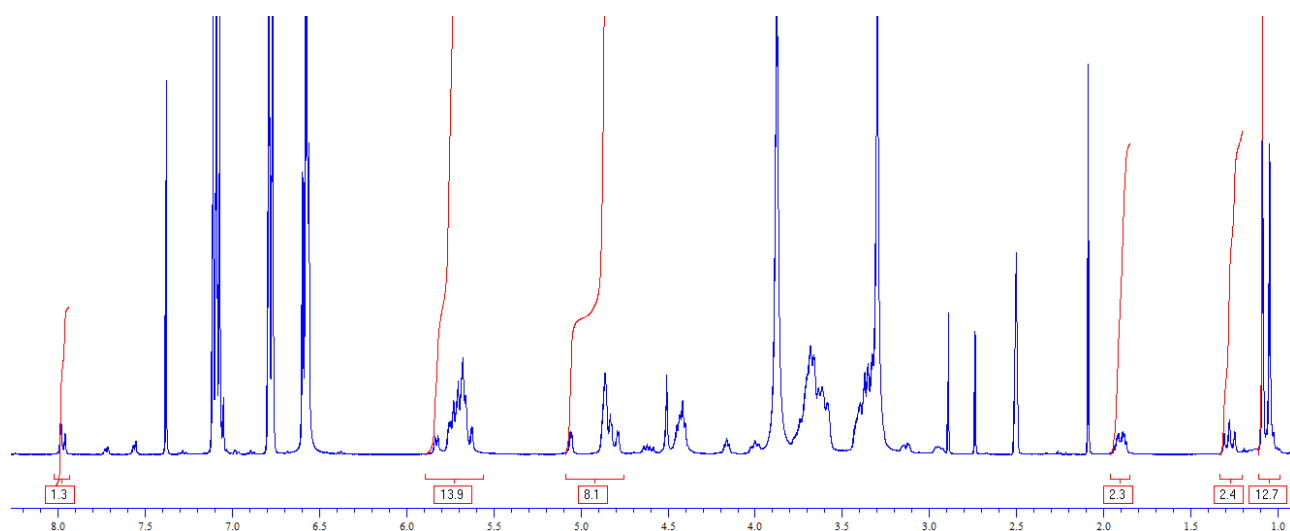
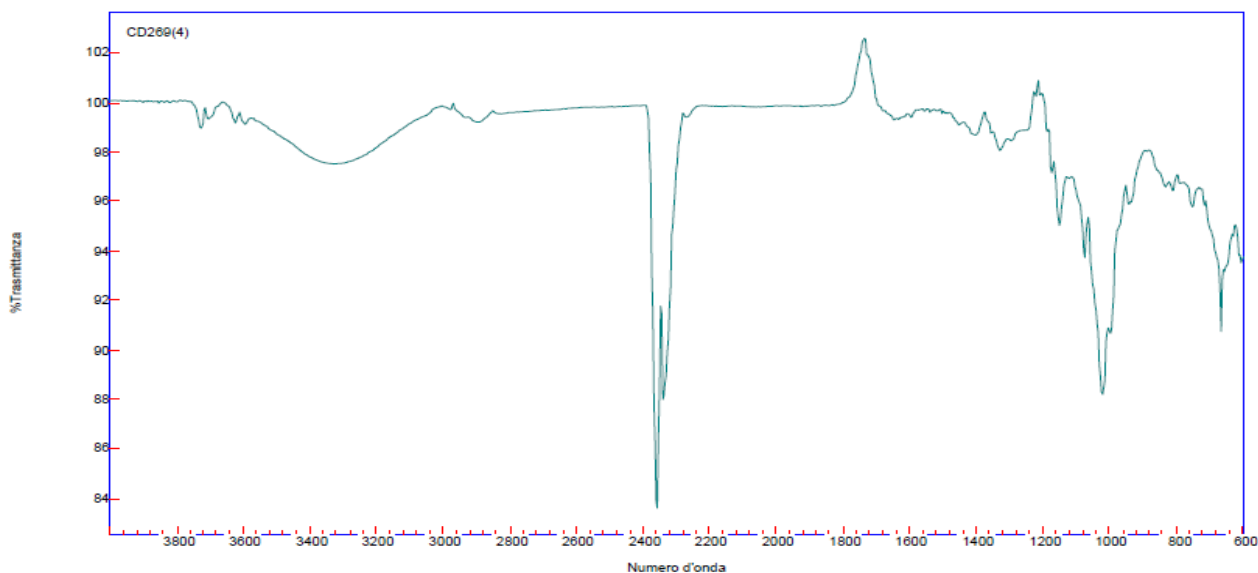


Figure 52: NMR spectrum of Mono 6 - (TEMPO) 6 - deoxy β cyclodextrin treated with D<sub>2</sub>O and phenylhydrazine

Because the Mono 6 (TEMPO) 6 deoxy β cyclodextrin contains a paramagnetic group, this aspect can influence the NMR measurement. In order to obtain a more definite spectrum, the product, as said, was treated with phenylhydrazine, able to quench the radical of the TEMPO. The count of the area is in agreement with the first spectrum: the peaks at 6.6, 6.8 and 7.4 are related to the hydrogens of the phenylhydrazine while the heavy peak at 7.1 is the hydroxyl group of TEMPO radical.



**Figure 53: IR spectrum of Mono 6 – (TEMPO) 6 – deoxy  $\beta$  cyclodextrin**

FT-IR analysis shows no peaks at 2100: this means the total absence of azide groups and, hence, their total conversion to TEMPO group.

#### 4.8.2. Mono 6 Tempo 6 deoxy $\beta$ Cyclodextrins – based nanosponges

Obtained paramagnetic cyclodextrins is possible finally synthetize corresponding nanosponges. For this step are involved two different crosslink agent in order to define two different nanosponge system: EDTA and PMA.

##### 4.8.2.1. Synthesis Mono 6 Tempo 6 deoxy $\beta$ Cyclodextrins – based nanosponges with PMA

In a one-neck flask (50 ml), Mono 6 Tempo 6 deoxy  $\beta$ cyclodextrins (274 mg, 0.2 mmol) was dissolved in DMSO (800  $\mu$ l). Then Et<sub>3</sub>N (6 drops), was dropped into the flask. The mixture was left under magnetic stirring until complete dissolution of Et<sub>3</sub>N and cyclodextrins into the solvent medium. At occurred dissolution, PMA (178 mg, 0.2 mmol, molar ratio 4:1 with CD) was added into the flask. A red hard solid is obtained after 30 minutes. This solid was minced using mortar. Finally the minced product was washed in a soxhlet with acetone in order to remove solvent and catalyst. The washed powder was dried in an oven at 100 °C for 4-5 hours.

#### 4.8.2.2. Synthesis Mono 6 Tempo 6 deoxy $\beta$ Cyclodextrins – based nanosponges with EDTA

In a flask (50 ml), Mono 6 Tempo 6 deoxy  $\beta$ cyclodextrins (274 mg, 0.2 mmol) was dissolved in DMSO (800  $\mu$ l). Then Et<sub>3</sub>N (6 drops), was dropped into the flask. The mixture was allowed to stirring until complete dissolution of Et<sub>3</sub>N and cyclodextrins into the solvent medium. At occurred dissolution, EDTA (204 mg, 0.8 mmol, molar ratio 4:1 with CD) was added into the flask. A red hard solid is obtained after 6 hours. This solid was minced using mortar. Finally the minced product was washed in a soxhlet with acetone in order to remove solvent and catalyst. The washed powder was allowed in an oven at 100 °C for 4-5 hours.

#### 4.8.3. Second approach: Hepta functionalization of $\beta$ CD with nitroxyl radical

This second synthesis approach is finalized to replace each  $\beta$ CD primary C6 alcohol present, with a paramagnetic group using TEMPO through again a click reaction. In order to obtain a selective substitution, it is necessary to carry out a different synthesis approach. Unlike mono or random functionalization of  $\beta$ CD, that provide the initial substitution of primary alcohol with a tosyl group, the first synthesis step provides the selective replacement of all primary hydroxyl group of a cyclodextrin with iodine atom, obtaining a hepta-iodo  $\beta$ CD. The opportunity for the symmetric derivation of  $\beta$ CD was found in a important reaction reported by Defaye and Gadelle. Next each iodine group of hepta-iodo  $\beta$ CD was replaced with an azide group in order to allow the click reaction with propargil-TEMPO.

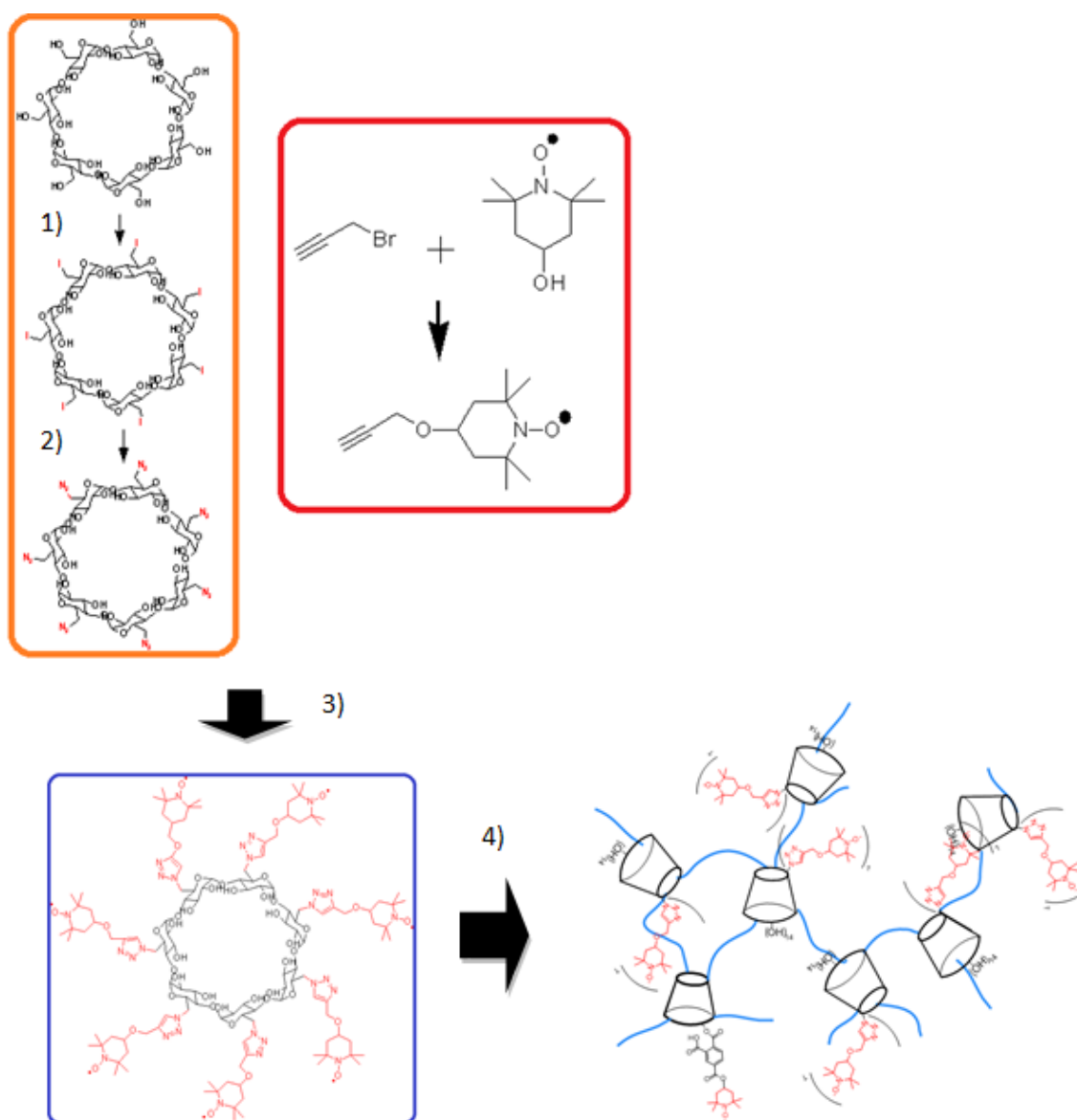


Figura 54: Synthesis scheme of Heptafunctionalized cyclodextrin - based nanosponges

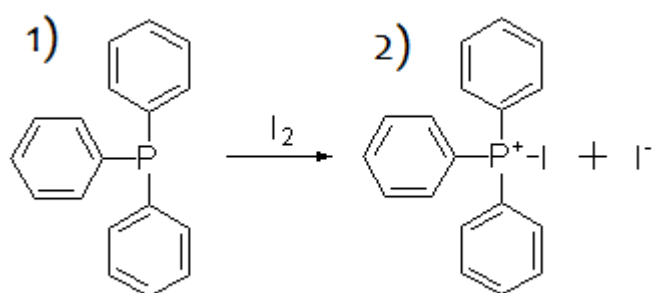


#### 4.8.3.1. Second approach: Hepta 6 (iodo) 6 deoxy $\beta$ cyclodextrin (CD4)

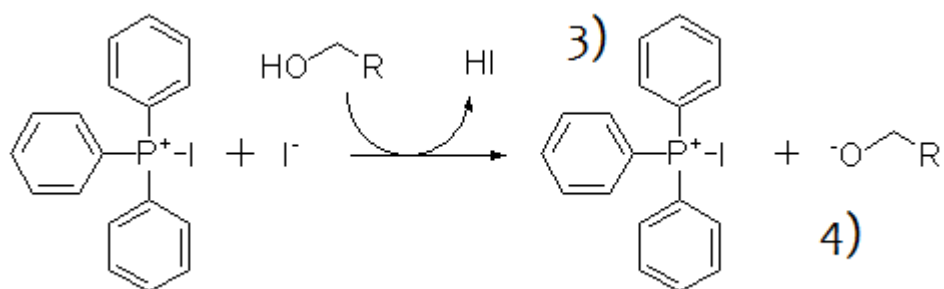
The iodo substitution of each primary alcohol occurs through an Appel reaction. The Appel reaction is an organic reaction that converts an alcohol into an alkyl chloride or iodide using triphenylphosphine and carbon tetrachloride or iodine.

The use of carbon tetrabromide or bromine as a halide source yields alkyl bromides, whereas using methyl iodide or iodine gives alkyl iodides.

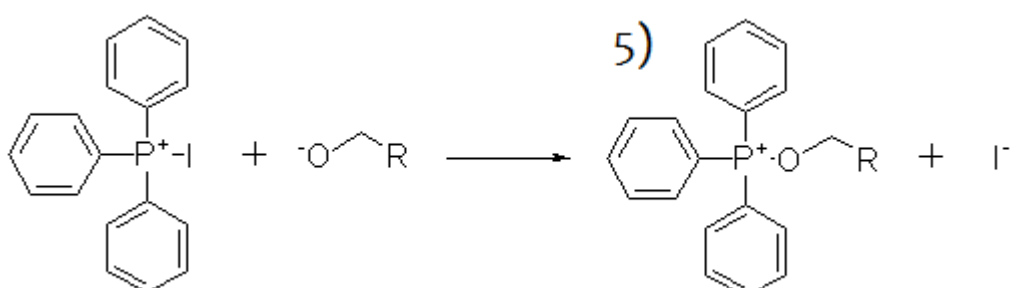
The Appel reaction begins with the formation of the phosphonium salt (2).



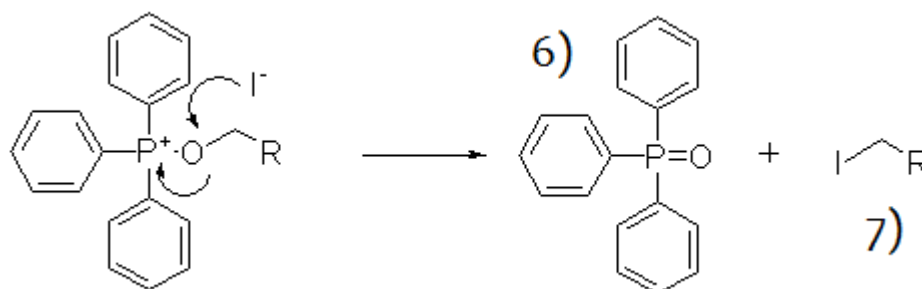
Deprotonation of the alcohol, forming HI (3), yields an alkoxide ion pair (4).



The nucleophilic displacement of the chloride by the alkoxide yields intermediate (5).



With primary and secondary alcohols, the halide reacts in a  $S_N2$  mechanism forming the alkyl halide (6) and triphenylphosphine oxide (7). Tertiary alcohols form the products (6) and (7) via a  $S_N1$  mechanism.



The driving force behind this and similar reactions is the formation of the strong PO double bond. The reaction is somewhat similar to the Mitsunobu Reaction, where the combination of an organophosphine as an oxide acceptor, a diazo compound as a hydrogen acceptor reagent, and a nucleophile are used to convert alcohols to esters and other similar applications.

#### 4.8.3.1.1. Synthesis Hepta 6 deoxy 6 iodo $\beta$ Cyclodextrins

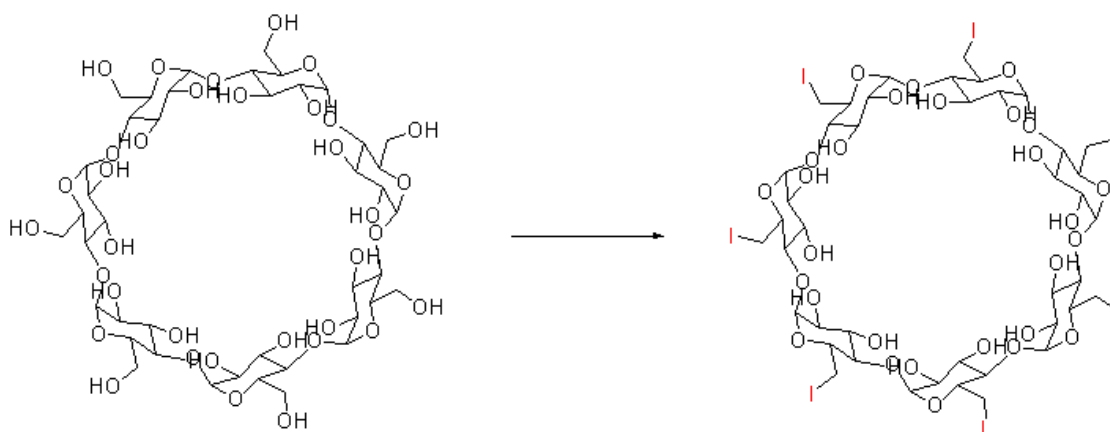


**Figure 55: Symmetric Iodination of  $\beta$ -CD**

In a two-necked flask (100 ml), Triphenylphosphine ( $PPh_3$ ) (7.78 gr, 29.6 mmol) was dissolved in DMF under vigorous stirring and under  $N_2$  atmosphere. Then Iodine (8.2 gr, 32 mmol) was added slowly into flask, paying attention to the exothermicity of the reaction: the solution appears dark purple. Dry  $\beta$ cyclodextrin (2.27 gr, 2 mmol) was added into the solution and the system was allowed to stirring for 18 hours. Subsequently the flask was placed under vacuum through Rotavapor. While the solvent was being removed from the flask, in another flask (125 ml), Sodium

Methoxide (NaOMe) (9.5 gr, 179 mmol) was dissolved in Methanol (30 ml). This solution was added into the first flask at 0 °C in order to neutralize acids through NaOMe and allowed to stirring for 30 minuts. Then the product was precipitated in Methanol obtaining a brown solid, subsequently separated by filtration and washed with MeOH. So the product was dried with air flow and put in a baker with acetone and acid chloride to remove bases. Finally the solid was washed with acetone. Obtaining pure with a yield of 82%. (3.14 gr, 1.65 mmol)

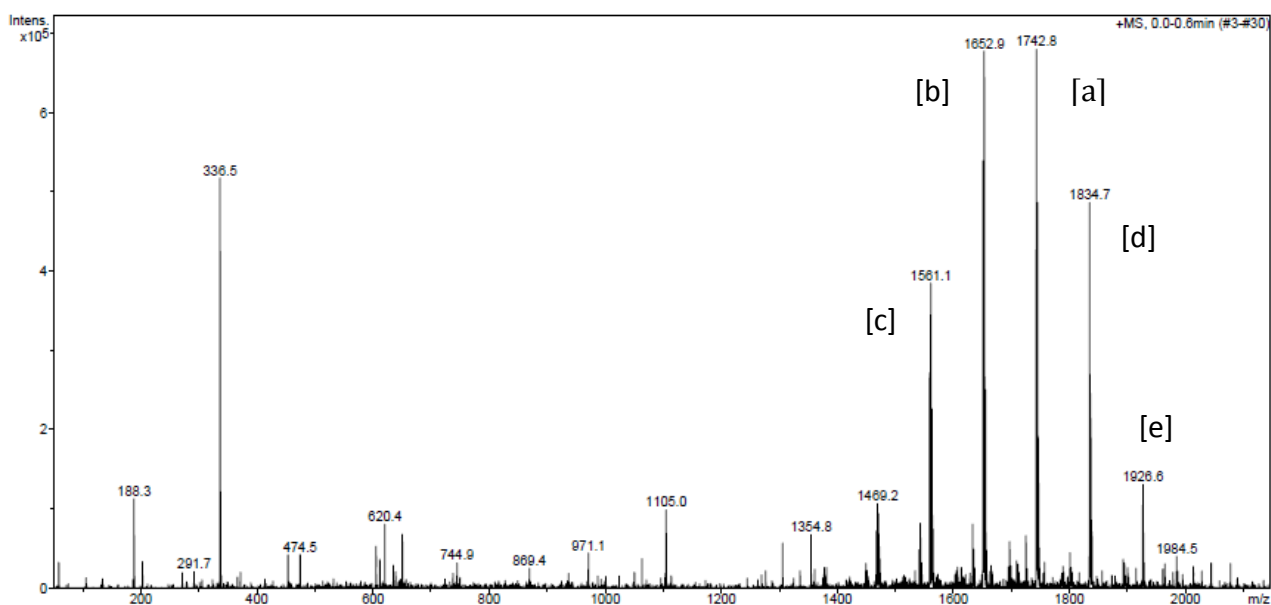


Figure 56: ESI Mass of Hepta 6 deoxy 6 iodo  $\beta$ Cyclodextrins

ESI – Mass:

- a)  $m/z = 1742.8$  (Hepta 6 (Iodine) 6 (deoxy)  $\beta$ cyclodextrin – 2 I + 2 Cl + Na<sup>+</sup>)
- b)  $m/z = 1652.9$  (Hepta 6 (Iodine) 6 (deoxy)  $\beta$ cyclodextrin – 3 I + 3 Cl + Na<sup>+</sup>)
- c)  $m/z = 1561.1$  (Hepta 6 (Iodine) 6 (deoxy)  $\beta$ cyclodextrin – 4 I + 4 Cl + Na<sup>+</sup>)
- d)  $m/z = 1834.7$  (Hepta 6 (Iodine) 6 (deoxy)  $\beta$ cyclodextrin – 1 I + 1 Cl + Na<sup>+</sup>)
- e)  $m/z = 1926.6$  (Hepta 6 (Iodine) 6 (deoxy)  $\beta$ cyclodextrin + Na<sup>+</sup>)

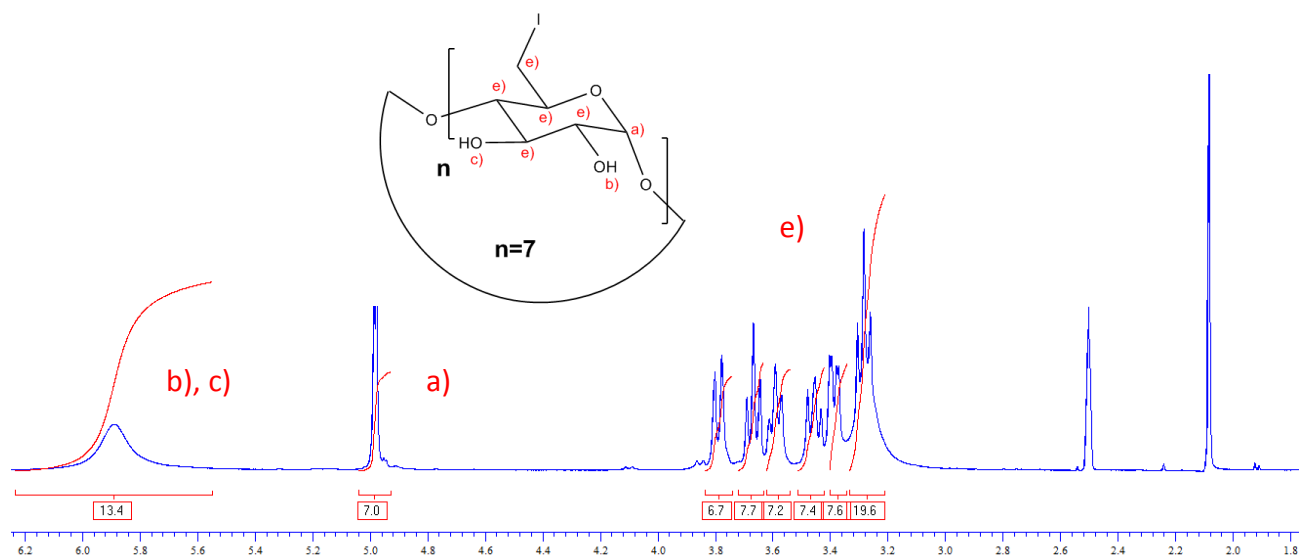


Figure 57: NMR spectrum of Hepta 6 deoxy 6 iodo  $\beta$ Cyclodextrins

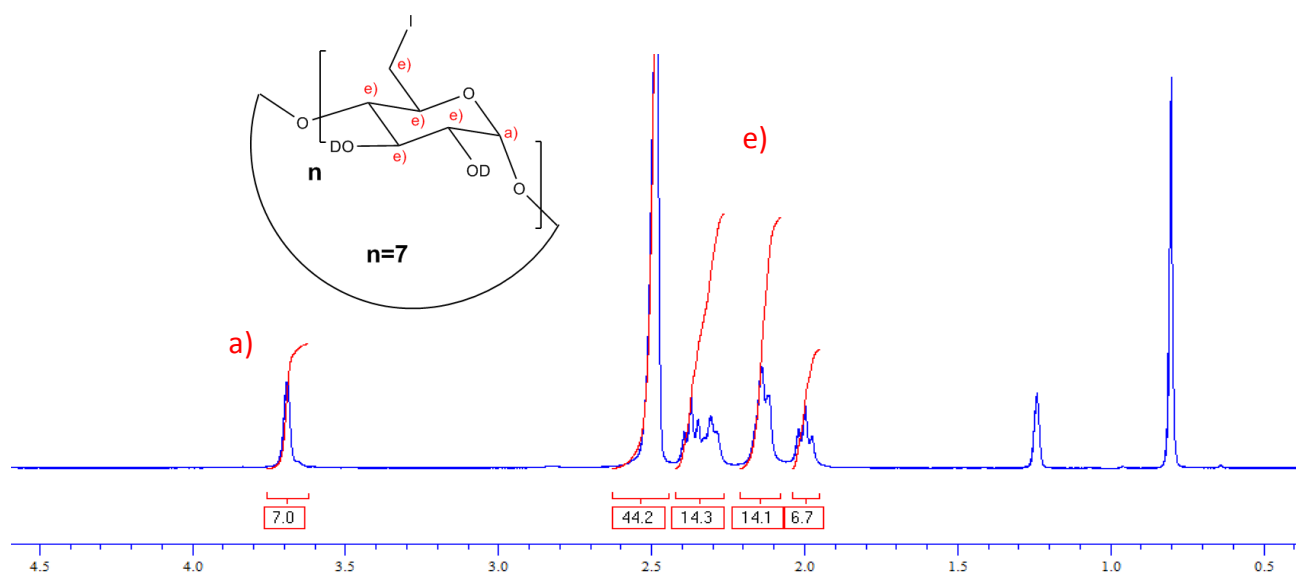


Figure 58: NMR spectrum of Hepta 6 deoxy 6 iodo  $\beta$ Cyclodextrins treated with  $D_2O$

Treating the product with  $D_2O$ , the hypothesis were confirmed: in fact the hump found at 5.85 ppm disappear, inasmuch as the hydroxyl group at C2, C3 position exchanged their hydrogens with the deuterium atoms of  $D_2O$ , becoming invisible at NMR spectrum.

#### 4.8.3.2. Second approach: Hepta 6 (azido) 6 deoxy $\beta$ cyclodextrin (CD5)

The next step provide the same mechanism seen during the synthesis of Mono 6-azido-6-deoxy- $\beta$ Cyclodextrins, with the substitution of azide groups at Iodine position.

#### 4.8.3.2.1. Synthesis of Hepta 6 (azido) 6 deoxy $\beta$ cyclodextrin

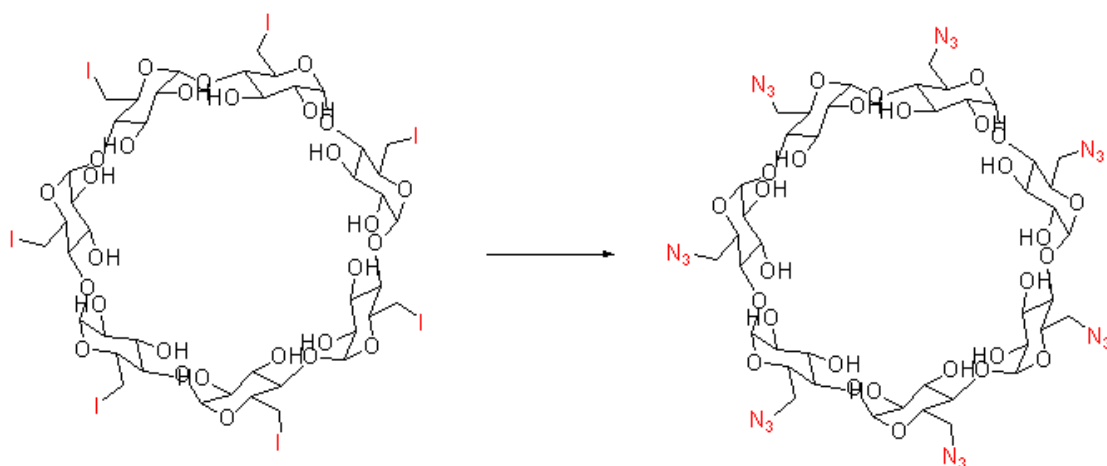


Figure 59: Substitution of iodine groups by azide groups

In a flask of 50 ml, Hepta 6 (Iodine) 6 (deoxy)  $\beta$  cyclodextrin (1.94 gr, 1 mmol) was dissolved under stirring in DMSO (10 ml) obtaining a reddish solution, that show the presence of residual iodine. Then the flask was placed into an oil bath at 80 °C using a relaps. The Sodium Azide (900 mgr, 13.85 mmol) was added into the flask and the solution was allowed to stir for 8 hours. The product was precipitated in water obtaining white pure solid with a yield of 78% (950 mgr, 0.71 mmol)

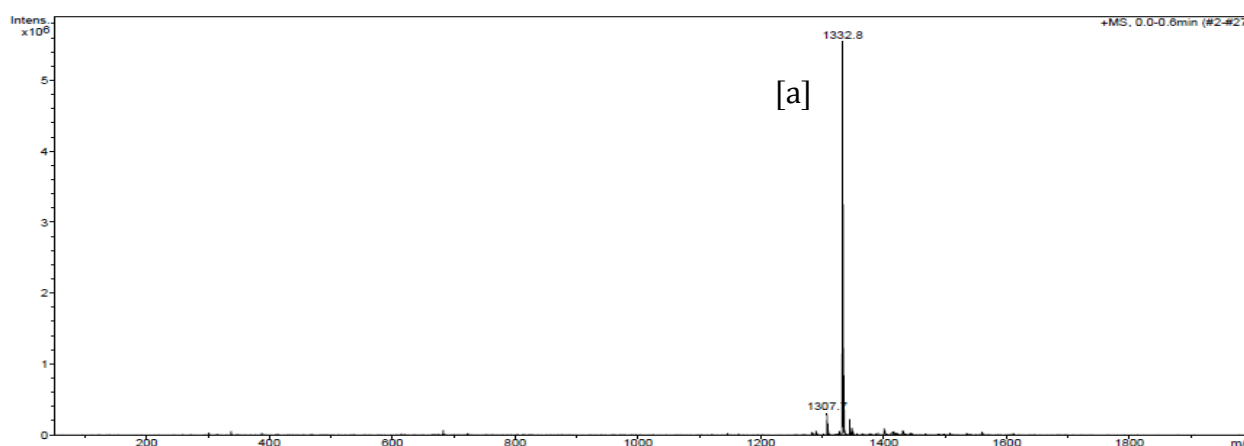


Figure 60: ESI Mass of Hepta 6 - (azide) 6 - deoxy  $\beta$  cyclodextrin

ESI – Mass:

a)  $m/z = 1332.8$  (Hepta 6 (Azide) 6 (deoxy)  $\beta$  cyclodextrin + Na<sup>+</sup>)

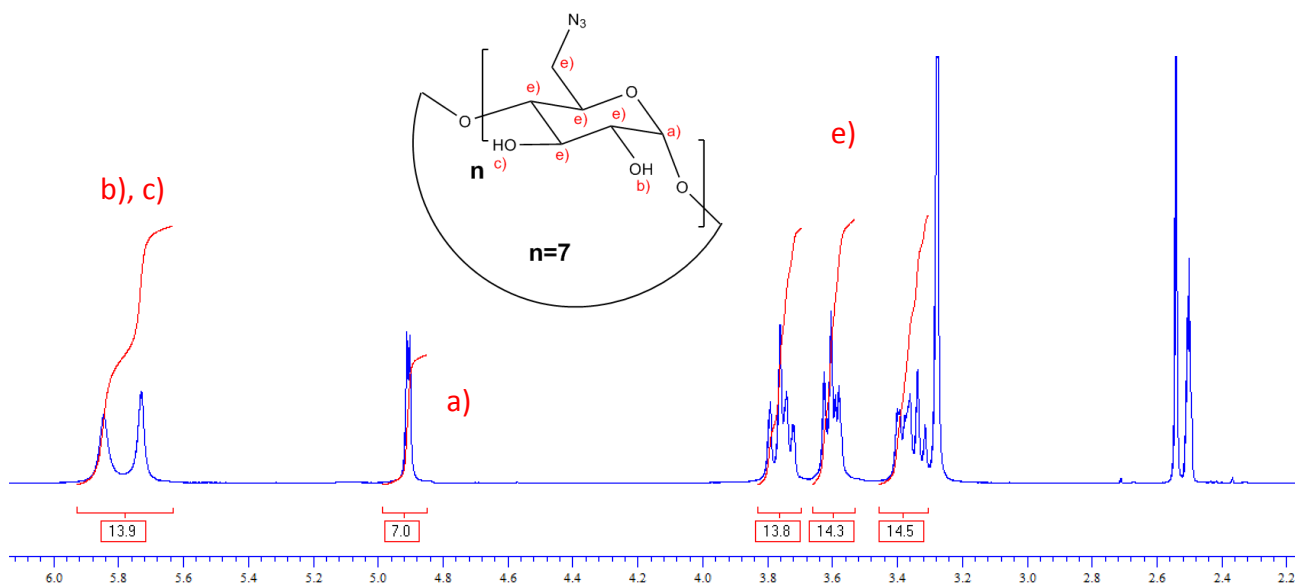


Figure 61: NMR spectrum of Hepta 6 - (azide) 6 - deoxy  $\beta$  cyclodextrin

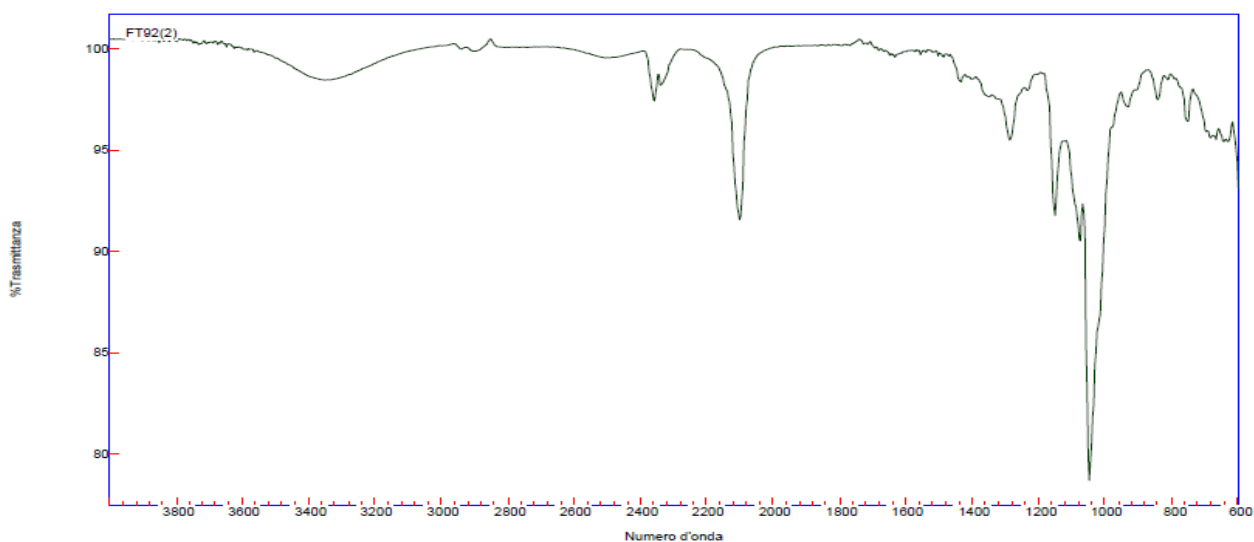


Figure 62: IR spectrum of Hepta 6 - (azide) 6 - deoxy  $\beta$  cyclodextrin

Through an IR analysis, the presence of the azide was confirmed: in fact the peak at 2100  $\text{cm}^{-1}$ , as wave number, identify the stretching of the azide group: note how the azide peak was more pronounced than the Mono 6 (azide) 6 deoxy  $\beta$  cyclodextrin due to higher concentration of  $\text{N}_3$  for each CD.

#### 4.8.3.3. Second approach: Hepta 6 (TEMPO) 6 deoxy $\beta$ cyclodextrin (CD6)

The last step of this synthesis, as the synthesis of Hepta 6 (azide) 6 (deoxy)  $\beta$  cyclodextrin, provide the same mechanism of the mono functionalization seen before, a Huygens cycloaddiction.

##### 4.8.3.3.1. Synthesis of Hepta 6 (TEMPO) 6 deoxy $\beta$ cyclodextrin

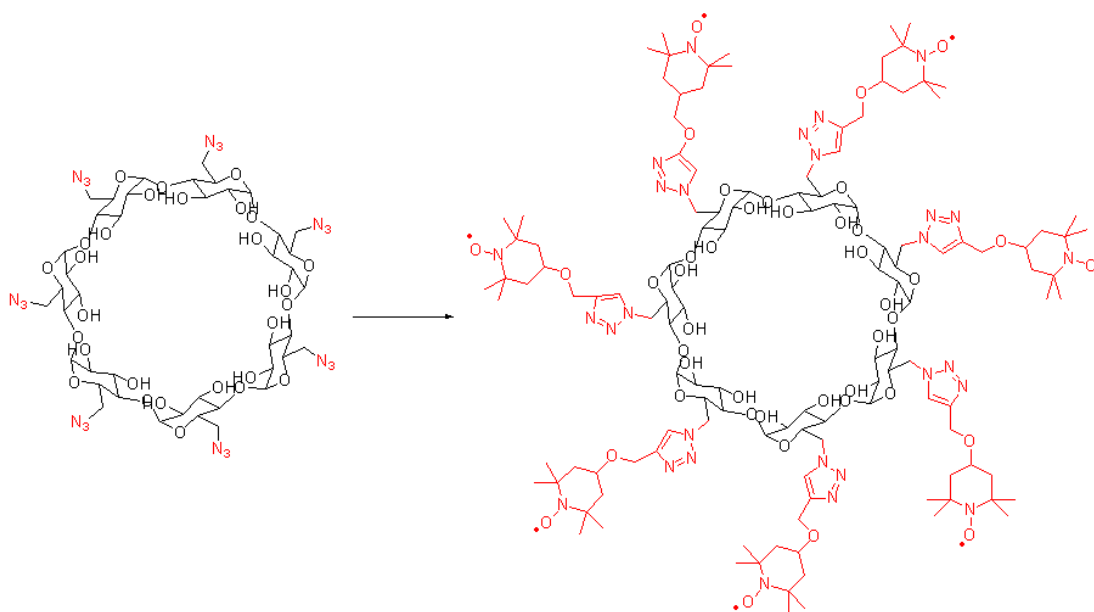


**Figure 63: Click reaction on Hepta 6 – (azide) 6 – deoxy  $\beta$  cyclodextrin**

In a two necked flask of 50 ml, Hepta 6 (azide) 6 (deoxy)  $\beta$  cyclodextrin (350 mg, 0.27 mmol) was dissolved in dimethylformamide (DMF) (2ml). Then Et<sub>3</sub>N was added to the solution (3 drops) . Under N<sub>2</sub> atmosphere, CuI was added into the flask. After 10 minutes, the flask was placed into a oil bath at 50 °C and the Propargil Tempo was added to the solution. The system was allowed to vigorous stirring overnight under N<sub>2</sub>. Unlike the Mono 6 (TEMPO) 6 deoxy )  $\beta$  cyclodextrin, the product doesn't precipitate in acetone, so the product was precipitated in H<sub>2</sub>O and filtrated obtaining a bright red solid with a quantitative yield.

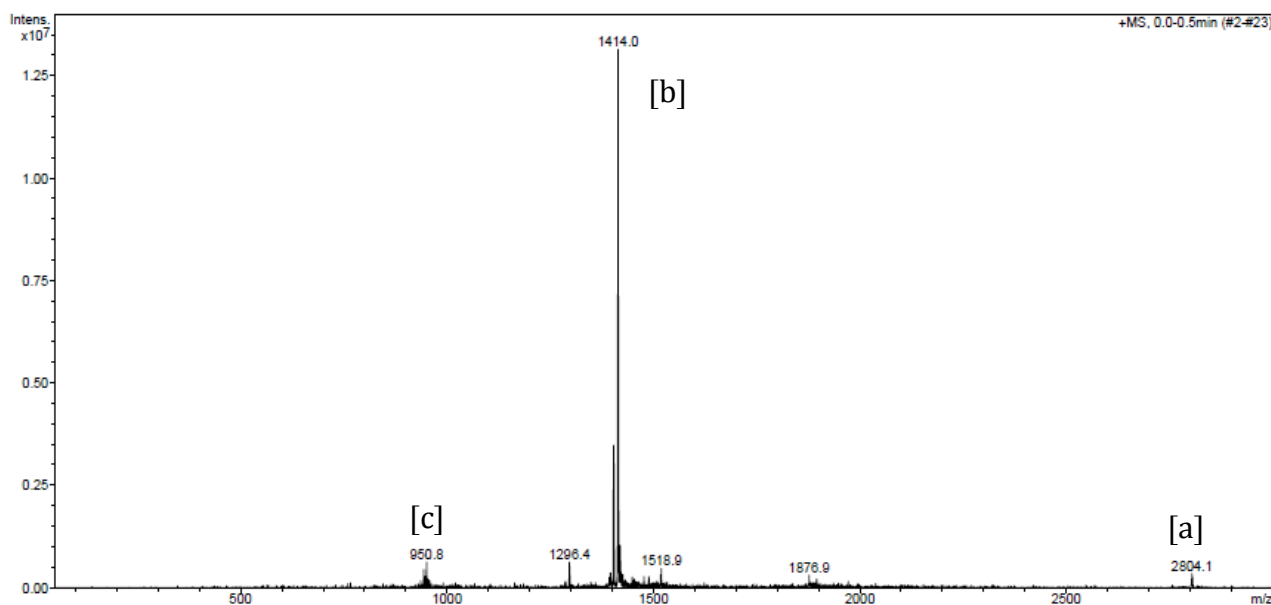


Figure 64: ESI Mass of Hepta 6 - (TEMPO) 6 - deoxy  $\beta$  cyclodextrin

ESI – Mass:

- a)  $m/z = 2804.1$  (Hepta 6 - (TEMPO) 6 - deoxy  $\beta$  cyclodextrin +  $\text{Na}^+$ )
- b)  $m/z = 1414.0$  (Hepta 6 - (TEMPO) 6 - deoxy  $\beta$  cyclodextrin +  $2\text{Na}^+$ )
- c)  $m/z = 950.8$  (Hepta 6 - (TEMPO) 6 - deoxy  $\beta$  cyclodextrin +  $3\text{Na}^+$ )

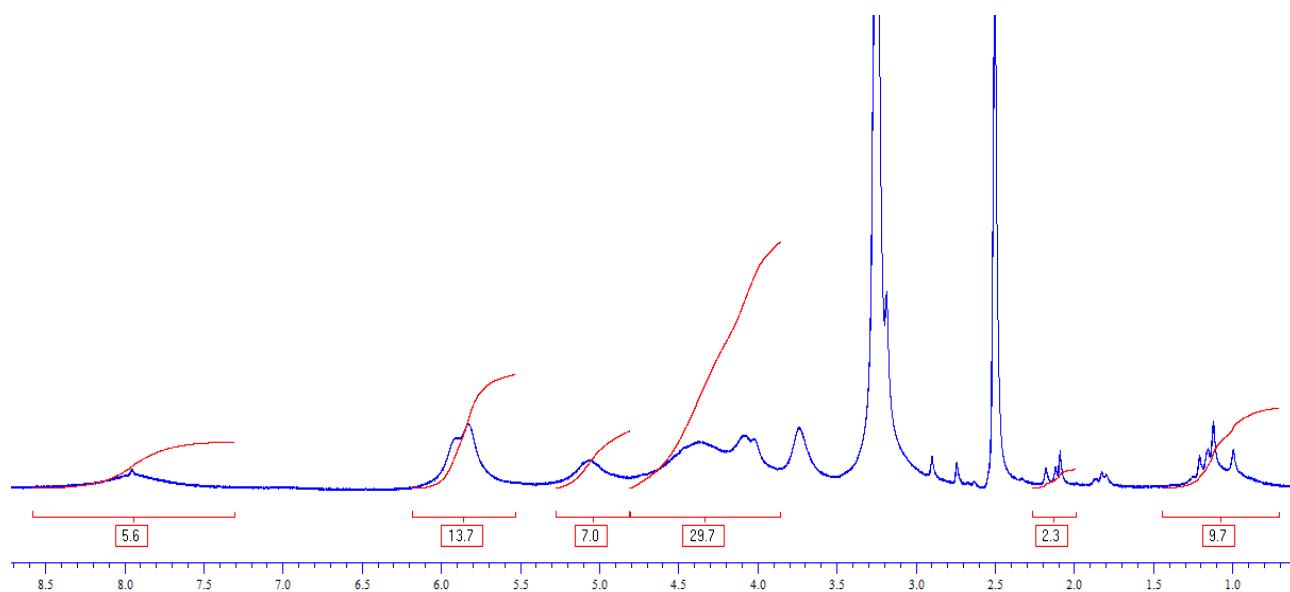
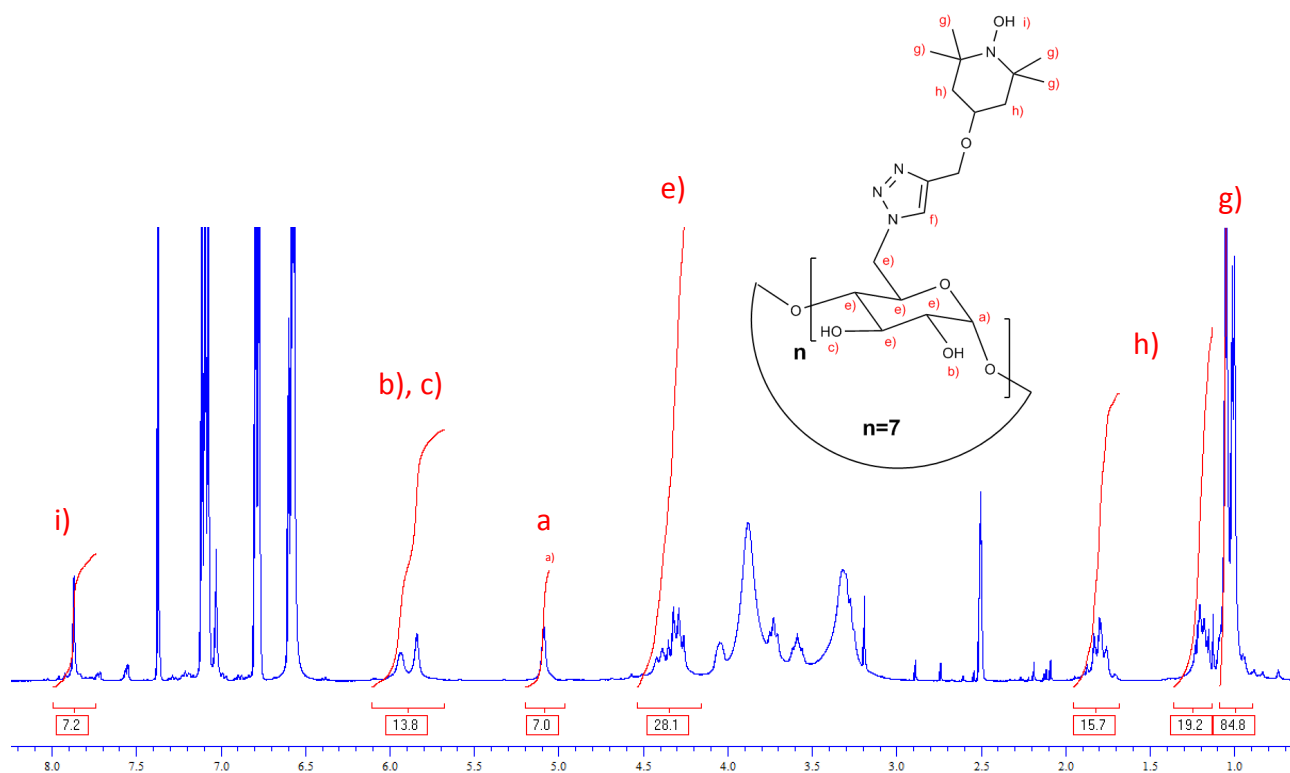


Figure 65: NMR spectrum of Hepta 6 - (TEMPO) 6 - deoxy  $\beta$  cyclodextrin





**Figure 66: NMR spectrum of Hepta 6 – (TEMPO) 6 – deoxy  $\beta$  cyclodextrin treated with phenylhydrazine**

In order to obtain a clearer spectrum was necessary treat the product with phenylidrazine.

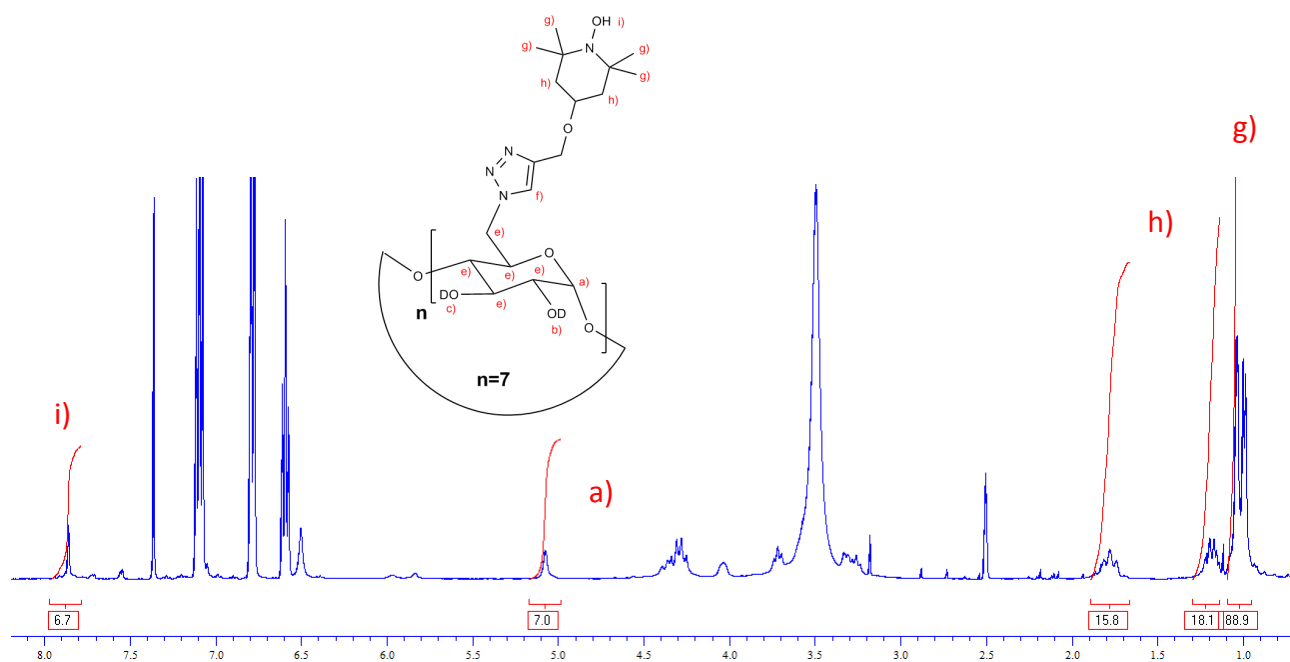


**Figure 67: NMR spectrum of Hepta 6 – (TEMPO) 6 – deoxy  $\beta$  cyclodextrin treated with phenylhydrazine and  $D_2O$**

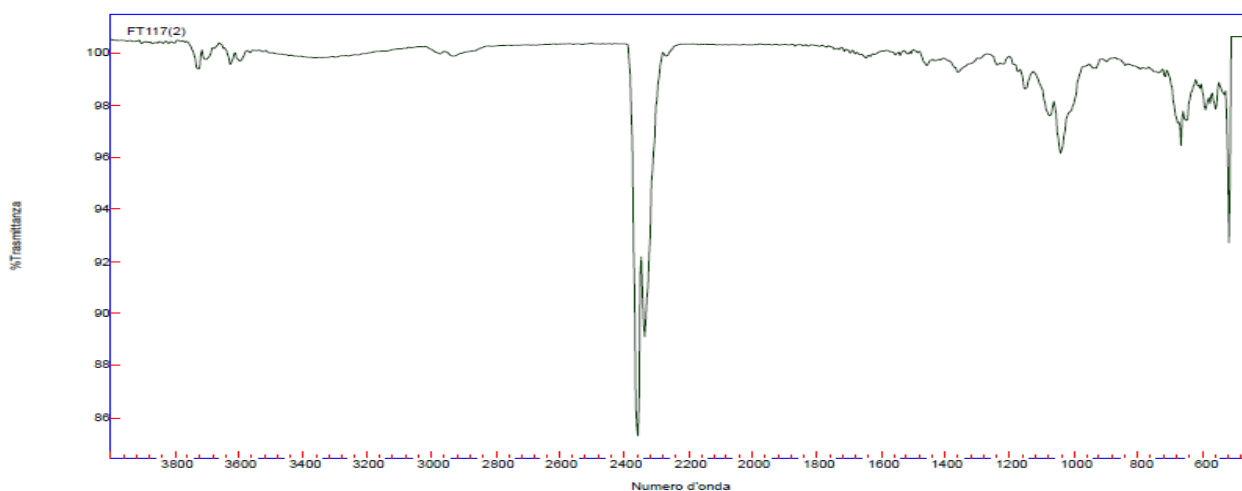


**Figure 68: IR spectrum of NMR Hepta 6 – (TEMPO) 6 – deoxy  $\beta$  cyclodextrin**

FT-IR analysis shows no peaks at 2100: this means the total absence of azide groups and, hence, their total conversion to TEMPO group.

#### 4.8.4. Synthesis Hepta 6 Tempo 6 deoxy $\beta$ Cyclodextrins – based nanosponges with PMA

In a flask of 50 ml, dry Hepta 6 Tempo 6 deoxy  $\beta$ cyclodextrins (100 mg, 0.0359 mmol) was dissolved in DMSO (400  $\mu$ l). Then Et<sub>3</sub>N (3 drops), was dropped into the flask. The mixture was allowed to stirring until complete dissolution of Et<sub>3</sub>N and cyclodextrins into the solvent medium. At occurred dissolution, PMA (31.36 mg, 0.1437 mmol, in molar ratio 4:1 with CD) was added into the flask. After 8 hours the system remained liquid without crosslinking, so the solution was allowed to stirring overnight. Neither with long time of reaction the polymerization occurred, hence the crosslink agent amount was increased (62.68 mg, 0.298 mmol, in molar ratio 8:1 with CD) without any result.

The likely explanation for this phenomenon is the following: having substituted every hydroxyl group at C6 position with a TEMPO group, only the hydroxyl group at C2 and C3 position remained available for the polymerization, but being secondary alcohol were much less reactive than the primary at C6 and they didn't give rise to the crosslink.

#### 4.9. Paramagnetic analysis

In order to check and analyze the paramagnetic characteristic of PMCDNS, magnetic measurements were carried out.

The magnetic property of systems is one of the fundamental properties in solid state physics. Using SQUID (superconducting quantum interference device) magnetometer, it is possible to easily and exactly measure the magnetization and magnetic susceptibility of many systems (one-, two-, and three-dimensional magnets) as a function of temperature and magnetic field.

If posed in an external magnetic field, the materials in which all the electrons are coupled are rejected by this one. The orbital plans are slightly inclined generating a little orbital magnetic moment, hence induced magnetic dipoles. These ones are oriented in opposition to the applied magnetic field (diamagnetism), regardless the temperature. Any material give a diamagnetic contribution because they hold coupled electrons in their orbitals.

On the contrary, these materials which hold unpaired electrons, are attracted by external magnetic field, generating magnetic dipoles that:

- Can be oriented in a casual way (paramagnetism), depending by temperature: isolated magnetic dipoles without interaction
- Interacting each other, can be totally parallel aligned (ferromagnetism, cooperative magnetism)
- Interacting each other, can be totally un-parallel aligned (antiferromagnetism)
- Interacting each other, can be anti-parallel aligned with a resulting moment not null

It is important to distinguish the orbital magnetic moment from the single spin magnetic moment: the first one is about the orbital movement of the electron with its angular orbital moment, while the second one in about the orbital movement of the spin with its angular orbital moment.

In diamagnetic materials, the electrons generate a weak magnetic field in opposition to the external one: the induced magnetic dipoles do not exist without an external magnetic field.

In paramagnetic materials, the magnetic moment is not null: the intrinsic magnetic dipoles tend to orient following the force lines of the field.

An increase of the temperature reduce this alignment, hence the paramagnetism.

The magnetic moment in physic is expressed in erg/Gauss or J/T, while in chemistry is expressed as the ratio between the magnetic moment of the materials and the Bohr's magneton, a fundamental physical constant that represents the quantum magnetic moment.

#### 4.9.1. Magnetization for the spin 1/2 system

It is necessary to introduce some simplifying hypothesis. The system consists of many spins ( $N_A$ ; Avogadro number) and, above all, there is no interaction between any two spins. The magnetic moment of spin ( $S = 1/2$ ) is given by equation 1:

$$\hat{\mu}_z = \frac{-2\mu_B * \hat{S}_z}{\hbar} = -\mu_B \hat{\sigma}_z \quad (1)$$

where  $\hat{\sigma}_z$  is a Pauli spin operator along the z axis,  $\hbar = h/2\pi$  with h defined as Planck's constant value and  $\mu_B$  is the Bohr magneton, a physical constant that describes the magnetic moment of the electron. The spin Hamiltonian (Zeeman energy) is described by eq. 2

$$\hat{H} = -\hat{\mu}_z B = -\mu_B \hat{\sigma}_z \quad (2)$$

in the presence of a magnetic field  $B$  along the z axis, where the Bohr magneton  $\mu_B$  is given by

$$\mu_B = -\frac{e\hbar}{2mc} \quad (3)$$

And it is equal to  $9.274 \cdot 10^{-24} \pm 3.1 \cdot 10^{-30} \left[ \frac{J}{T} \right]$ , where e is the elementary charge of the electron ( $e = -1.60 \cdot 10^{-19}$  [C])

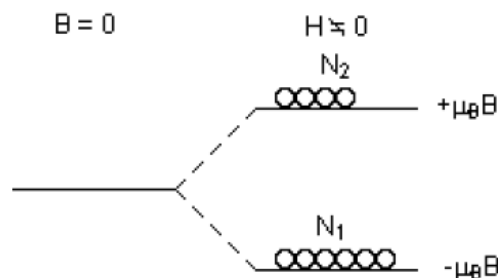


Figure 69: Zeeman splitting of the degenerate state under the application of magnetic field B

The doublet state (degenerate) is split into two states:

1. lower energy level ( $-\mu_B B$ ): state - ;  $\mu_B$  (magnetic moment)
2. upper energy state ( $\mu_B B$ ): state + ;  $-\mu_B$  (magnetic moment)

The probability of finding the system in the lower state is given by the equation 4 where  $x = \frac{\mu_B B}{k_B T}$

$$\frac{N_1}{N_A} = \frac{e^x}{e^x - e^{-x}} \quad (4)$$

The probability of finding the system in the upper state is

$$\frac{N_2}{N_A} = \frac{e^{-x}}{e^x - e^{-x}} \quad (5)$$

The total magnetization M is:

$$M = \mu_B (N_1 - N_2) = N_A \mu_B \left( \frac{e^x - e^{-x}}{e^x + e^{-x}} \right) = N_A \mu_B \tanh(x) \quad (6)$$

- For  $x \ll 1$ ,  $\tanh(x) \sim x$ , then:

$$M = N_A \mu_B \frac{\mu_B B}{k_B T} = N_A B \frac{\mu_B^2}{k_B T} \quad (7)$$

The magnetic susceptibility (molar) is a dimensionless proportionality constant that indicates the degree of magnetization of a material in response to an applied magnetic field and it is defined as

$$\chi_M = \frac{M}{B} = N_A \frac{\mu_B^2}{k_B T} = N_A \frac{\mu_B^2}{3k_B T} g^2 S(S+1) \quad (8)$$

Where g is the Landè g-factor: for an electron with both spin and orbital angular momenta. It is a proportionality constant that connect the magnetic moment  $\mu$  to the quantic number of the total angular momentum ( $J=L+S$ ) and to a fundamental magnetic unit, for example the Bohr's magneton. In this case  $g=2$  for  $S=1/2$ . It is possible introduce, from wave mechanics, the effective magnetic moment (spin only) of a single electron in Bohr's magnetons  $\mu_{eff}$ :

$$\mu_{eff} = \sqrt{S(S+1)} \mu_B \quad (9)$$

where S is spin quantic number (1/2) and directly the effective magnetic moment of a single electron in erg/Gauss  $P_{eff} = g\mu_{eff}$

$$P_{eff} = g\sqrt{S(S+1)} \mu_B \quad (10)$$

The susceptibility obeys to the Curie law: if the material is heated, the direct proportionality between the magnetization of the material and the applied magnetic field, is reduced:

$$\chi_M = \frac{C_M}{T} \quad (11)$$

Where  $C_M$  is the Curie constant and, expressing  $\chi_M$ , is defined by

$$C_M = N_A \frac{\mu_B^2}{3k_B} P_{eff}^2 = 0.125 P_{eff}^2 \sim P_{eff}^2 / 8 \quad (12)$$

- For  $x \gg 1$ ,  $\tanh(x) \sim 1$ , so the saturation magnetization  $M_s$  is obtained:

$$M_s = N_A \mu_B g S = N_A \mu_B = 5.5849 \cdot 10^3 [emu] \quad (13)$$

Where  $\mu_B$  is expressed in emu:  $\mu_B 9.274 \cdot 10^{-21} emu$  (1 emu = erg/Gauss)

#### 4.9.2. Brillouin function

Moving to analyze the magnetization in general case (J), the magnetic moment is given by

$$\hat{\mu}_z = -g_J \mu_B \hat{J}_z \quad (14)$$

Where  $\hat{J}_z$  is the (dimensionless) angular momentum ( $J_z = J, J-1, \dots, -J$ ) and  $g_J$  is the Landè g-factor.

Then the spin hamiltonian (Zeeman energy) is described by

$$\hat{H} = -\hat{\mu}_z B = -(-g_J \mu_B \hat{J}_z) B = g_J \mu_B \hat{J}_z B \quad (15)$$

In the presence of a magnetic field B. Under the magnetic field, the degenerate ground state is split into (2J+1) states. The energy level and the magnetic moment for each state are described by

$$\varepsilon(J_z) = g \mu_B \hat{J}_z B \text{ and } \mu(J_z) = -g_J \mu_B \hat{J}_z \quad (16)$$

The magnetization M at T is given by

$$M = N_A \langle \mu(J_z) \rangle = N_A g_J \mu_B \langle J_z \rangle = N_A g_J \mu_B \frac{\sum_{J_z=-J}^J (-J_z) e^{-\beta \varepsilon(J_z)}}{\sum_{J_z=-J}^J e^{-\beta \varepsilon(J_z)}} \quad (17)$$

Where  $\beta = 1/(k_B T)$ . For simplicity:

$$x = \frac{g_J \mu_B J B}{k_B T} \quad (18)$$

Then:

$$M = N_A g_J \mu_B \frac{\sum_{J_z=-J}^J (-J_z) e^{-x/J_z}}{\sum_{J_z=-J}^J e^{-x/J_z}} = N_A g_J \mu_B J \frac{d}{dx} \ln \left( \sum_{J_z=-J}^J e^{-x/J_z} \right) = N_A g_J \mu_B J B_J(x) \quad (19)$$

where  $B_J(x)$  is the Brillouin function and is defined by

$$B_J(x) = \frac{2J+1}{2J} \coth \left( \frac{2J+1}{2J} x \right) - \frac{1}{2J} \coth \left( \frac{1}{2J} x \right) \quad (20)$$

And its properties are:

$$\lim_{J \rightarrow \infty} B_J(x) = L(x) = \coth(x) - \frac{1}{x}; \text{ where } L(x) \text{ is the Langevin function;}$$

$$\lim_{x \rightarrow 0} B_J(x) = \frac{J+1}{3J} x;$$

$$\lim_{x \rightarrow \infty} B_J(x) = 1.$$

- For  $x \ll 1$ ,

$$M = N_A g_J \mu_B J B_J(x) = \frac{N_A g_J^2 \mu_B^2}{3k_B T} J(J+1) B \quad (21)$$

The susceptibility (molar) is given by

$$\chi = \frac{M}{B} = N_A \frac{\mu_B^2}{3k_B T} g_J^2 J(J+1) = \frac{C_M}{T} \quad (22)$$

Where  $C_M$  is the Curie's constant and is defined by, using the expression of effective magnetic moment (dimensionless):

$$C_M = N_A \frac{\mu_B^2}{3k_B} g_J^2 J(J+1) = N_A \frac{\mu_B^2}{3k_B} P_{eff}^2 \sim \frac{P_{eff}^2}{8} \quad (23)$$

Knowing the Curie's constant, it is possible to express this latter in relation with the effective magnetic moment (spin only)  $\mu_{eff}$ :

$$\mu_{eff} = 2.84C_M^{1/2} \quad (24)$$

It is important to define that some materials (ferromagnetic and antiferromagnetic) do not obey the Curie's law, but rather the Curie-Weiss' law:

$$\chi = \frac{C_M}{(T - \vartheta)} \quad (25)$$

Where  $\vartheta$  is a temperature and it is expressed as Weiss' constant.

The Curie-Weiss' law describes:

- Paramagnetic materials that tend to a ferromagnetic order under a particular temperature: Curie's ferromagnetic temperature
  - Paramagnetic materials that tend to a antiferromagnetic order under a particular temperature: Neel's ferromagnetic temperature
- For  $x \rightarrow \infty$ , the saturation magnetization  $M_s$  is defined

$$M_s = N_A g_J \mu_B J \quad (26)$$

#### 4.9.3. Calculation of M vs B/T

The Landè g-factor  $g_J$  is defined by

$$g_J = \frac{3}{2} + \frac{S(S+1) - L(L+1)}{2J(J+1)} \quad (27)$$

Where L and S are orbital and spin angular moment, respectively. The magnetization per units atom is defined as

$$\tilde{M} = \frac{M}{N_A \mu_B} = g_J J B_J(x) \quad (28)$$

With  $x = \frac{g_J \mu_B J B}{k_B T}$

Theoretically  $g_J$  is equal to 2 and for convenience it is usually used the notation g and S for J (S follows the Hund rule). The value of g in real system is not equal to 2.

Now, knowing Brillouin's formula it is possible to express the relation between magnetization and B/T (magnetic induction/temperature)



$$\tilde{M} = \frac{M}{N_A \mu_B} = g_J J B_J(x)$$

$$B_J(x) = \frac{2J+1}{2J} \coth\left(\frac{2J+1}{2J} x\right) - \frac{1}{2J} \coth\left(\frac{1}{2J} x\right)$$

$$\tilde{M} = g \left( \frac{2J+1}{2} \coth\left(\frac{2J+1}{2J} x\right) - \frac{1}{2} \coth\left(\frac{1}{2J} x\right) \right) \quad (29)$$

Expressing x and rearranging the above formula:

$$\tilde{M} = g \left( (J+0.5) \coth\left(\frac{2J+1}{2J} \frac{g\mu_B J B}{k_B T}\right) - 0.5 \coth\left(\frac{1}{2J} \frac{g\mu_B J B}{k_B T}\right) \right)$$

$$= g \left( (J+0.5) \coth\left((J+0.5) \frac{g\mu_B B}{k_B T}\right) - 0.5 \coth\left(0.5 \frac{g\mu_B B}{k_B T}\right) \right) \quad (30)$$

Being  $\coth(x) = 1/\tanh(x)$

$$\tilde{M} = g \left( \frac{(J+0.5)}{\tanh\left((J+0.5) \frac{g\mu_B B}{k_B T}\right)} - \frac{0.5}{\tanh\left(0.5 \frac{g\mu_B B}{k_B T}\right)} \right) \quad (31)$$

Finally, defining the following factor

$$b = \frac{\mu_B}{k_B} = 0.672 [K/T];$$

$$\tilde{x} = \frac{B}{T} = \frac{\mu_0 H}{T};$$

The relation between M and B/T is obtained:

$$\tilde{M} = g \left( \frac{(J+0.5)}{\tanh((J+0.5)gb\tilde{x})} - \frac{0.5}{\tanh(0.5gb\tilde{x})} \right) \quad (32)$$

#### 4.9.6. Random grafted TEMPO cyclodextrin based nanosponge.

The isotherm magnetization for random grafted TEMPO cyclodextrin based nanosponge shows a spin quantum number equal to  $\frac{1}{2}$ , in fact the fit of the experimental data meet a Brillouin function with  $J = 1/2$ , hence only a radical. The curve (red line) was obtained by the difference between nanosponge and the TEMPO unit minus the sponge contribute:

$$M(H, 2K, TEMPO + sponge) - M(H, 2K, sponge)$$

and it was expressed as magnetization per gram and normalized to  $M_{sat}$  (saturation magnetization), where

$$M_{sat} = \frac{N_A \mu_B}{M_{mole}}$$

with  $M_{mole} = 346,26 \text{ g}$

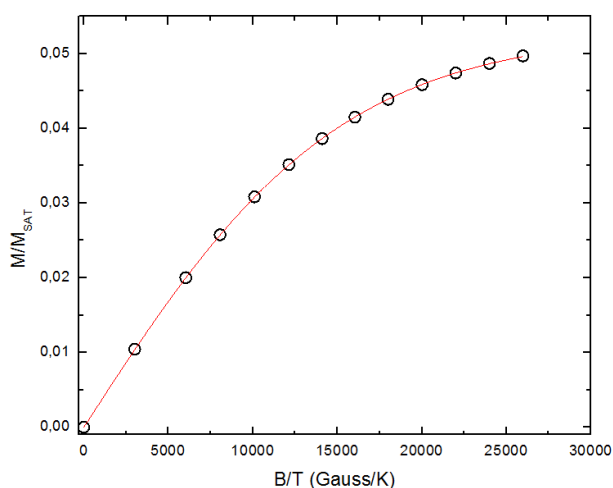


**Figure 70: Graphic Magnetization Vs B/T of random grafted TEMPO cyclodextrin based nanosponge**

From the fit results that in the sample  $52,97 \pm 0.03 \text{ mg}$  of TEMPO unit per material gram are present in the sample.

Through the Curie-Weiss' law, valued with a magnetic induction equal to 500 Oe, it was possible identify a Weiss constant minor than 0 ( $\vartheta = -4.3 \text{ K}$ ), implying antiferromagnetic interaction between the TEMPO units into the nanosponge.

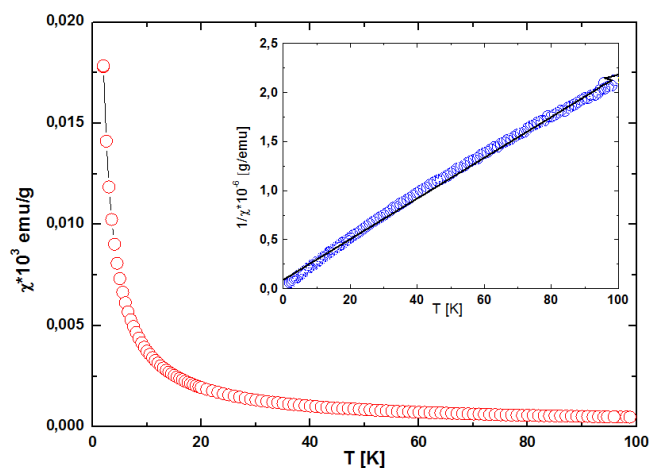


Figure 71: Curie-Weiss' law of random grafted TEMPO cyclodextrin based nanosponge

The  $\chi T$  curve, depending on  $T$ , confirms the antiferromagnetic interactions: in fact for a system that do not expect any interaction, the product susceptibility for temperature must be constant with the temperature. Positive deviation (upward) indicate ferromagnetic interactions, while negative (downward) antiferromagnetic.

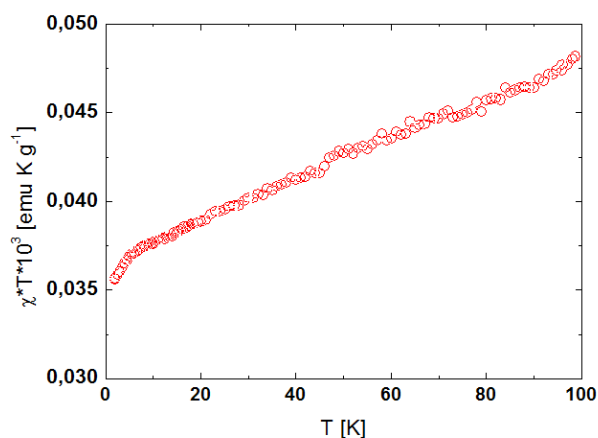


Figure 72: Graphic Magnetization\*Temperature Vs Temperature of random grafted TEMPO cyclodextrin based nanosponge

#### 4.9.4. Magnetic measurements of Mono – 6 – (TEMPO) – 6 (deoxy) – $\beta$ cyclodextrin

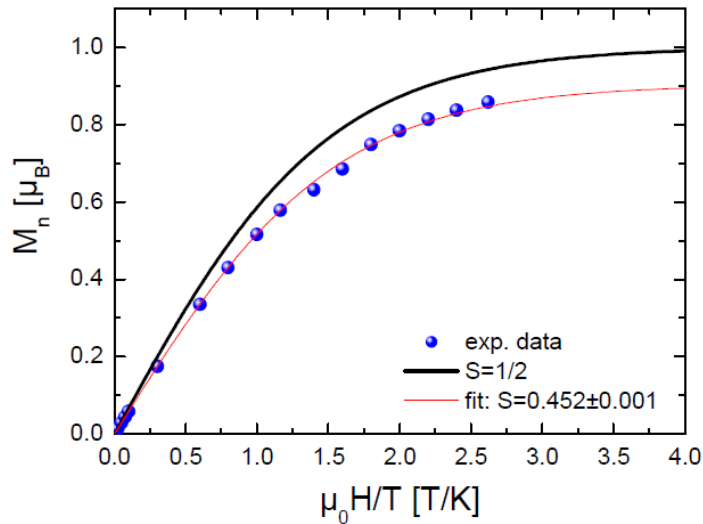


Figure 73: Graphic Magnetization Vs B/T of Mono 6 – (TEMPO) 6 – deoxy  $\beta$  cyclodextrin

The above graphic shows the behavior of the Mono – 6 – (TEMPO) – 6 – (deoxy) -  $\beta$  cyclodextrin, varying the magnetic induction at constant temperature (2 K).

The black line represent the equation 32

$$\tilde{M} = g \left( \frac{(J + 0.5)}{\tanh((J + 0.5)gb\tilde{x})} - \frac{0.5}{\tanh(0.5gb\tilde{x})} \right)$$

where J, the spin quantic number, is equal to  $\frac{1}{2}$ . It represent the ideal behavior assuming no spin interaction ( $g = 2$ ).

The experimental data are represented by the blue rounds, which are well fitted ( $R^2=0.99938$ ) by the same equation used before. The fit, however, shows a spin quantic number different from  $\frac{1}{2}$  but equal to  $0.452 \pm 0.001$ . This result implies a different value for the effective magnetic moment  $\mu_{eff}$ : Equal to  $1.62 \mu_B$ , instead of  $1.73 \mu_B$ : the expected one.

$$\mu_{eff} = \sqrt{S(S + 1)}\mu_B$$

This outcome is compatible with what it get through a fit with a Curie-Weiss' law on experimental data of susceptibility as a function of temperature at a magnetic field of 0.05 T. The fit is reasonable ( $R^2=0.9993$ ) provided an enough great offset ( $x_0$ ) was introduced.

$$\chi = \frac{C_M}{(T - \vartheta)} + x_0$$

where  $x_0$  is equal to 0.00215.

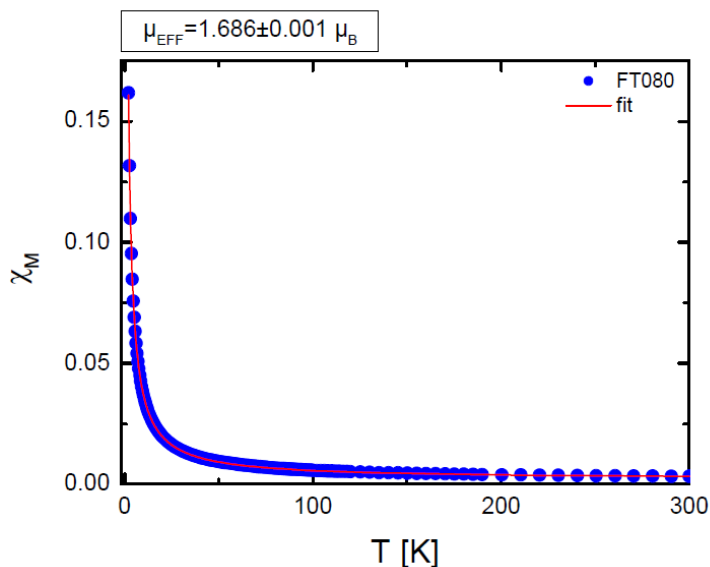


Figure 74: Curie-Weiss' curve of Mono 6 - (TEMPO) 6 - deoxy  $\beta$  cyclodextrin

Experimental data including the Pascal's correction.

The represented curve identifies a paramagnetic behavior and a Weiss' constant minor than zero Kelvin ( $\vartheta = -0,24077 \pm 0.00418$  K), which shows an anti-ferromagnetic trend: the paramagnetic species that tend to an anti-ferromagnetic order, in fact, have  $\chi$  value lower than a paramagnetic normal species. This shifts the Curie-Weiss' curve to lower temperatures and the Weiss' constant goes under 0 K.

From the same Curie-Weiss' law the obtained Curie's constant ( $C_M = 0.35581 \pm 0.00044$ ) offers a similar value for the effective magnetic moment  $\mu_{eff}$  to the one previously obtained ( $1.62 \mu_B$ ):

$$\mu_{eff} = 2.84C_M^{1/2} = 1.689 \mu_B$$

The spin quantum number obtained, minor than  $\frac{1}{2}$ , can be explained as follows: because the experimental data are under the theoretical black line, it can hypothesized the presence of a weak anti-ferromagnetic interaction between the free radicals. Another possible explanation should involve the combination between TEMPO radicals and cyclodextrins that should result in a little but not negligible fraction of electrons no more unpaired through a coupling of radicals.

#### 4.9.5. Magnetic measurements of Hepta – 6 – (TEMPO) – 6 (deoxy) – $\beta$ cyclodextrin

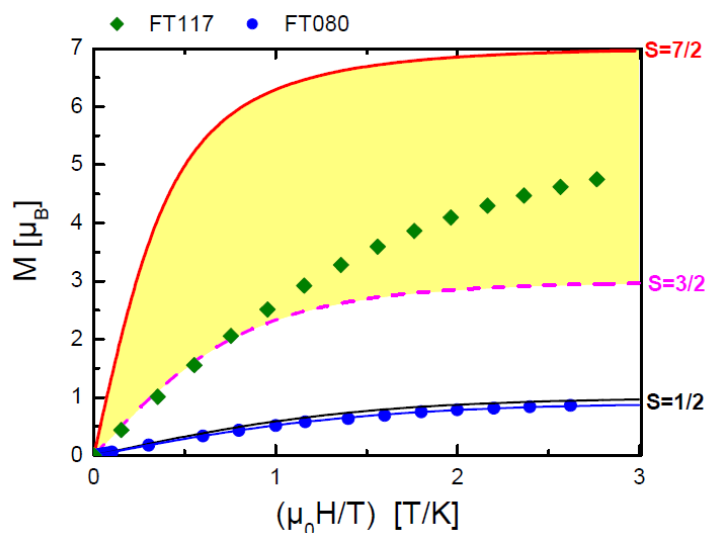


Figure 75: Graphic Magnetization Vs B/T of Hepta 6 – (TEMPO) 6 – deoxy  $\beta$  cyclodextrin

For the Hepta – 6 – (TEMPO) – 6 (deoxy) –  $\beta$  cyclodextrin is used the same formula that correlates the magnetization to B/T ( $\tilde{x}$ ):

$$\tilde{M} = g \left( \frac{(J + 0.5)}{\tanh((J + 0.5)gb\tilde{x})} - \frac{0.5}{\tanh(0.5gb\tilde{x})} \right)$$

The blue round represent the experimental data of Mono – 6 – (TEMPO) – 6 (deoxy) –  $\beta$  cyclodextrin and the similar behavior with  $J = \frac{1}{2}$ , while the green rhombus represent the experimental data of Hepta – 6 – (TEMPO) – 6 (deoxy) –  $\beta$  cyclodextrin. As shown the behavior of this latter do not fit with any curve (black, rose and red) that represent a spin quantum number equal to 1/2, 3/2 and 7/2 respectively. This result means that the hypothesis of non-interacting spins made primarily is no more valid: the spins of this molecule interact at solid state.

As proof that the system has spins strongly interacting the graphic M(H) at different temperatures is reported: the curves at different temperature do not shift with  $\mu_0H$ . The Hepta – 6 – (TEMPO) – 6 (deoxy)  $\beta$ -cyclodextrin has radicals that interact each other as much as the temperature decreases and the magnetic field is higher.

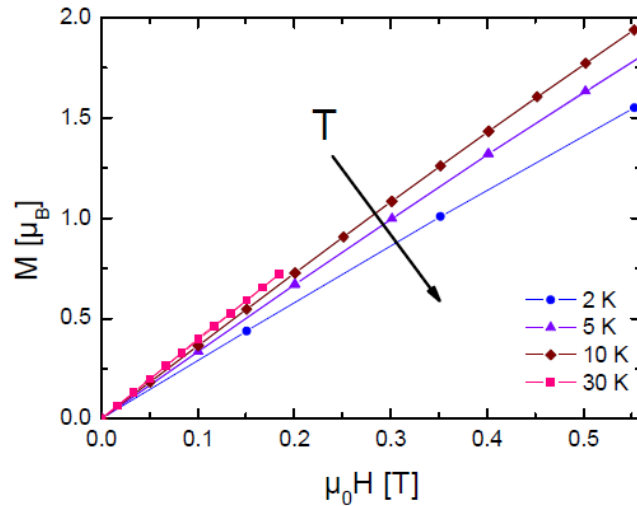


Figure 76: Graphic Magnetization Vs B of Hepta 6 - (TEMPO) 6 - deoxy  $\beta$  cyclodextrin

Finally the Curie-Weiss' law shows the presence of anti-ferromagnetic behavior, obtaining a Weiss' constant minor than zero at different magnetic fields ( $\vartheta = -0.71 \pm 0.07$  K at  $B = 0.05$  T and  $\vartheta = -1.24 \pm 0.02$  K at  $B = 3$  T). The Curie's constant obtained instead gives an effective magnetic moment  $\mu_{eff}$  equal to  $4.193 \pm 0.001 \mu_B$  at  $B = 0.05$  T and equal to  $4.235 \pm 0.001 \mu_B$  at  $B = 3$  T.

The  $\chi T$  curve has an offset and a trend the depend slightly by the applied diamagnetic correction: if the Pascal's correction is increased from  $7 \times 10^{-7}$  emu/Gauss to  $8 \times 10^{-7}$  emu/Gauss some improvements are noted.

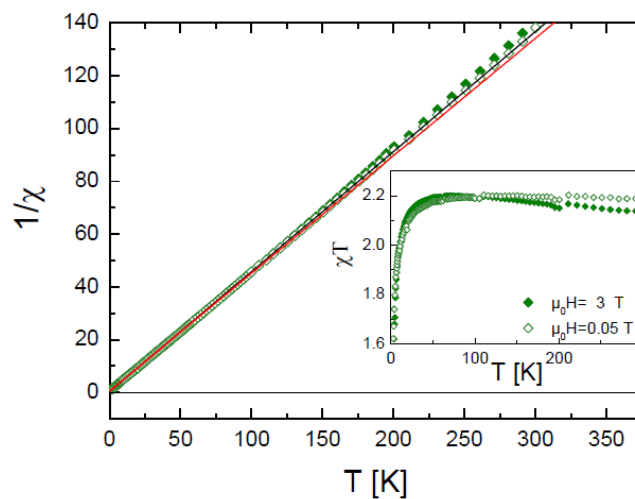


Figure 77: Curie-Weiss' law of Hepta 6 - (TEMPO) 6 - deoxy  $\beta$  cyclodextrin

From this analysis it is possible to conclude that the Hepta – 6 – (TEMPO) – 6 (deoxy)  $\beta$ -cyclodextrin has an actually free spin major than 3/2, hence has three free radicals: so certainly there are at least three TEMPO groups for each CD.

#### **4.10. EPR measurements**

##### Electron Paramagnetic Resonance

Electron Paramagnetic Resonance or Electron Spin Resonance, known as the EPR or ESR is a spectroscopic technique used to detect and analyze chemical species containing one or more unpaired electrons (named paramagnetic species). These species include free radicals, ions of transition metals, defects in crystals, molecules in the triplet electronic state of the fundamental (e.g. molecular oxygen) or induced for photoexcitation. The basic concepts of the EPR technique are similar to those of the nuclear magnetic resonance, but in this case are the electron spins to be excited instead of spins of atomic nuclei.

A electromagnetic radiation generator issues microwave in a very short frequency field. Through an electromagnet, it is possible to continuously modify the applied magnetic field and with a detector the extent of absorption suffered by electromagnetic radiation is measured and recorded as function of the magnetic field intensity.

An EPR analysis allowed to quantify the concentration of nitroxide in the synthesized molecules. Thanks to Marco Lucarini, from university of Bologna, EPR measurement are realized on the paramagnetic cyclodextrin-based nanosponges with two different crosslinkers (PMA and EDTA), on the random grafted TEMPO cyclodextrin nanosponges and on the Hepta – 6 – (TEMPO) – 6 deoxy  $\beta$ Cyclodextrin obtaining the following information.



#### 4.10.3. Random grafted TEMPO cyclodextrin based nanosponge

This nanosponge shows a concentration of nitroxide equal to 0.22 mmol/g

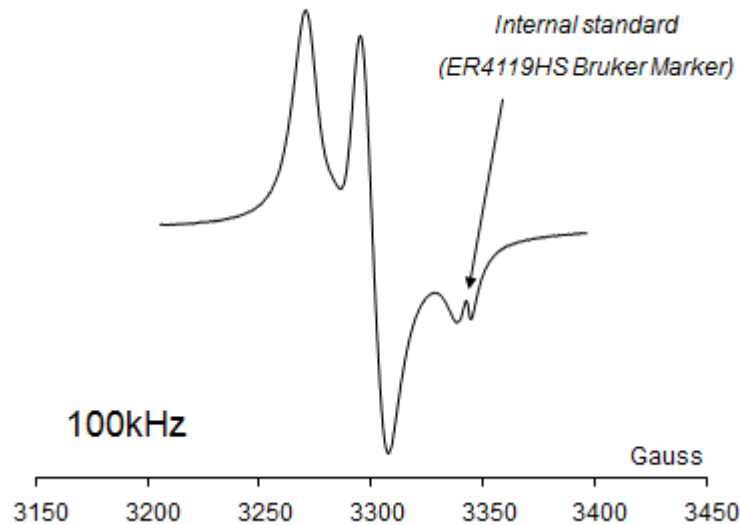


Figure 78: EPR spectrum of random grafted TEMPO cyclodextrin based nanosponge

#### 4.10.1. Mono 6 Tempo 6 deoxy βCyclodextrins – based nanosponges with PMA

This nanosponge shows, from a quantitative analysis, a concentration of nitroxide equal to 0.57 mmol/g. From this output it is possible to calculate the effective crosslinking degree of the nanosponge. In fact, in an ideal crosslinker-CD ratio 4:1, as expected, the concentration of nitroxide should be 0.446 mmol TEMPO/g: this value can be obtained weighing the single TEMPO unit of the expected molecular weight of the same nanosponge:

$$C_{nitroxide} = \frac{TEMPO \text{ unit}}{MW_{TEMPO-CD} + x \cdot MW_{CL}}$$

so:

$$\frac{1}{1,37 \left[ \frac{g}{mmol} \right] + 4 \cdot 0,218 \left[ \frac{g}{mmol} \right]} = 0,446 \left[ \frac{mmol \text{ TEMPO}}{g} \right]$$

Obtaining a nitroxide concentration equal to 0.57 mmol/g it is possible to extrapolate the crosslinker amount for each CD, the new variable:

$$\frac{1}{1,37 \left[ \frac{g}{mmol} \right] + x \cdot 0,218 \left[ \frac{g}{mmol} \right]} = 0,57 \left[ \frac{mmol \text{ TEMPO}}{g} \right]$$

The effective crosslinker/CD ratio is equal to 1.76, instead than 4.

Furthermore it was measured the behavior of the TEMPO radical during the transition from the solid (blocked) to the liquid (mobile) phase: three samples in water are considered over time (from 0 to 192 hours), with h (hydration ratio) equal to 3, 6 and 12 respectively. In each case, the “mobile” component increases over time, as shown by the EPR spectrum. The blocked one has a more marked transition in the first 50 hours, after that the amount of nitroxide remains constant. Passing from a h value of 3 to 6, a significant increase of “mobile” component is observed, while passing from 6 to 12 this difference is less marked.

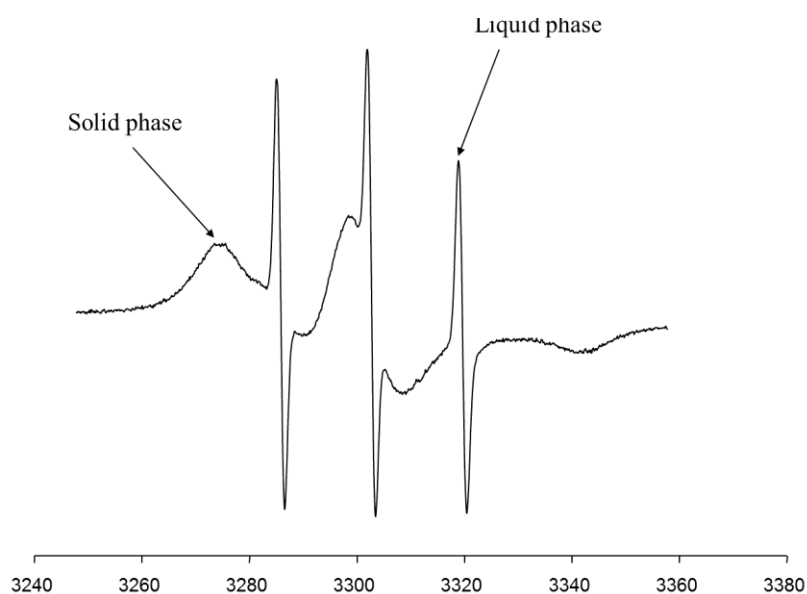


Figure 79: EPR spectrum of paramagnetic cyclodextrin based nanosponge with PMA as CL

#### 4.10.2. Mono 6 Tempo 6 deoxy $\beta$ Cyclodextrins – based nanosponges with EDTA

This nanosponge shows a concentration of nitroxide equal to 0.63 mmol/g, instead of 0.418 mmol/g (the expected value), that translates a crosslinker/CD ratio equal to 0.85, instead of 4, following the same formula used previously:

$$\frac{1}{1,37 \left[ \frac{g}{mmol} \right] + x \cdot 0,256 \left[ \frac{g}{mmol} \right]} = 0,63 \left[ \frac{mmol \text{ TEMPO}}{g} \right]$$

In order to analyze the transition behavior from the blocked to mobile phase, the same test was performed on this nanosponge. Three samples in water were considered over time (from 0 to 192 hours), with h (hydration ratio) equal to 3, 6 and 12 respectively. In each case, already from the beginning a significant amount of “mobile” component that remained constant over time (in the sample with h = 12, over time a slightly increasing of the “mobile” component is observed). In each case the amount of nitroxide remains constant. Passing from an h value of 3 to 6 and to 12 a slight direct dependencies of the mobile component with the dilution.

#### 4.10.4. Hepta – 6 – (TEMPO) – 6 – deoxy $\beta$ Cyclodextrins

The Hepta-6-(TEMPO)-6-(deoxy)  $\beta$ Cyclodextrin's spectrum is characterized by an only enlarged band, typical of a strong exchange interaction between electronic nitroxy units. Therefore the interaction between radicals is confirmed.

The measure of 82% (error  $\pm$  5%) indicates an quasi-quantitative presence of nitroxy units.

## Conclusions

The first part of this thesis project focused on the design and optimization of the synthetic procedure for the production of cyclodextrin-based nanosponges (CDNS), systems with peculiar absorption and release properties which can find application in medicine and environment.

CDNS were obtained by controlled cross-linking of cyclodextrins (CD) with different sources of cross-linkers (CL), especially di-anhydrides, with different CD:CL ratio and their behavior was in-depth investigated. The anhydrous state of reagents resulted crucial for a correct reticulation and optimized work-up allowed to remove most of the impurities included during the synthesis.

The optimization of the synthetic process allowed to carry on a detailed the IR and RAMAN analysis, obtaining information about the reticular structure of the system.

Important physical information was obtained, including rigidity and swelling ability in relation with the type of cross-linker and its amount and with the type of cyclodextrin. The sol-gel phase transition was also investigated.

Another objective of this thesis was the synthesis and the analysis of spin label nanosponges, finalized to obtain materials with paramagnetic and anti-oxidant proprieties.

Initially, random paramagnetic nanosponges were synthesized using TEMPO anhydride as grafting agent. The functionalization and the reticulation of the cyclodextrin were obtained in a one-pot reaction. However, SQUID and EPR measurements revealed a nitroxyl concentration lower than that expected one. For this reason, a second approach was considered, consisting in the synthesis of a paramagnetic cyclodextrin (pmCD) by anchoring a TEMPO unit to the cavitand via click reaction. This approach also ensured a bond strength higher than that in the ester moiety. Following this procedure, it was then possible to conduct cross-linking of pmCD, leading to the formation of pmCDNS. The presence of a single nitroxyl unit per CD allowed to determine the distribution of paramagnetic groups in the final nanosponge. The SQUID and EPR analysis revealed an increase of nitroxyl groups with respect to the random TEMPO nanosponges but, also, a slight interaction between radicals. This analysis allowed to identify an hypothetical reticulation degree, noting that the amount of cross-linkers was much lower than that expected. It is important to underline that this result was slightly influenced by the presence of the solvent and the catalyst entrapped into the CD unit.

Exploiting this information, the synthesis was targeted to increase the nitroxyl groups on each CD unit, obtaining a hepta-functionalization, hence a material more sensitive to magnetic field. SQUID results actually showed an increase of radical spins, but lower than that expected, suggesting a strong interaction between the radicals in the solid state, depending on the magnetic field. The concentration of nitroxyl groups determined by EPR technique in solution resulted almost quantitative.

Unfortunately it was not possible to synthesize the respective nanosponges probably due to the low reactivity of the secondary hydroxyl groups of the cyclodextrin unit.

# Bibliography – Chapter 1

- 1 Martin Del Valle, E. M. *Process Biochem.* **2004**, 39, 1033–1046.
- 2 Kurkov, S. V.; Loftsson, T. *Int. J. Pharm.* **2013**, 453(1),167-80.
- 3 Duchêne, D.; Ponchel, G.; Wouessidjewe, D. *Adv. Drug Delivery Rev.* **1999**, 29–40.
- 4 Li, D.; Ma, M. *Cyclodextrin polymer separation materials*, **1998**, WO 9822197.
- 5 Li, D.; Ma, M. *Clean Technol. Environ. Policy* **2000**, 2, 112–116.
- 6 Trotta, F.; *Cyclodextrin Nanosponges and Their Applications. In Cyclodextrins in Pharmaceutics, Cosmetics and Biomedicine: Current and Future Industrial Applications*; Bilensoy, E., Ed.; John Wiley & Sons: Hoboken, NJ, USA, **2011**, 323–342.
- 7 David, F. *Nanosponge drug delivery system more effective than direct injection*, **2011**.
- 8 Alongi, J.; Poskovic, M.; Frache, A.; Trotta, F. *Carbohydrate Polymers*, **2011**, 86, 127– 135.
- 9 Renuka, S.; Roderick, B.W.; Kamla, P. *Ind. J. Pharm. Edu. Res.*, **2011**; 45(1), 25-31.
- 10 Renuka, S.; Kamla, P. *Pharm. Dev. Technol.*, **2011**, 16(4),367-376.
- 11 Gilardi G, Trotta F, Cavalli R, Ferruti P, Ranucci E, Di Nardo G, Roggero C, Tumiatti V. *Cyclodextrin nanosponges as carrier for biocatalysts, and in the delivery and release of enzymes, proteins, vaccines and antibodies*, **2008**, WO/2009/149883.
- 12 Trotta, F.; Tumiatti, W. *Cross-linked polymers based on cyclodextrins for removing polluting agents*, **2009**, WO 03/085002 A1.
- 13 Wong, V.N.; Fernando, G.; Wagner, A.R.; Zhang, J.; Kinsel, G.R.; Zauscher, S.; Dyer, D.J. *Langmuir*, **2009**; 25(3), 1459-65.
- 14 Cavalli, R.; Akhter, A.K.; Bisazza, A.; Giustetto, P.; Trotta, F.; Vavia, P. *Int. J. Pharm.*, **2010**, 402(1-2), 254-257.
- 15 Longo, C.; Gambarà, G.; Espina V., Luchini, A., Bishop, B.; Patanarut, AS., Petricoin, EF. 3rd, Beretti, F.; Ferrari, B.; Garaci, E.; De Pol, A.; Pellacani, G.; Liotta, LA. *Exp. Dermatol.*, **2011**, 20(1), 29-34.
- 16 Castiglione, F.; Crupi, V.; Majolino, D.; Mele, A.; Panzeri, W.; Rossi, B.; Trotta, F.; Venuti, V. *J. Inclusion Phenom. Macrocyclic Chem.* **2013**, 75, 247-254.
- 17 Rossi, B.; Caponi, S.; Castiglione, F.; Corezzi, S.; Fontana, A.; Giarola, M.; Mariotto, G.; Mele, A.; Trotta, F.; Petrillo, C.; Villani, G. *J. Phys. Chem. B* **2012**, 116, 5323–5327.

18 Trotta, F.; Cavalli, R.; Tumiatti, W.; Zerbinati, O.; Roggero, C.; Vallero, R. *Ultrasound assisted synthesis of cyclodextrin based nanosponges*, 2008, WO2006002814.

## Bibliography – Chapter 2

- 1 Villiers, A. *Compt. Rend. Acad. Sci.* **1891**, 112, 536–538.
- 2 Eastburn, S.D.; Tao, B.Y. *Biotechnology Advances*, **1994**, 12, 2, 325-339
- 3 Szejtli, J. *Chemical Reviews*, July **1998**, 5, July 1998, 1743-1753
- 4 Schardinger, F. *Zeitschrift für Untersuchung der Nahrungs- und Genußmittel*, October **1903**, 6, 19, 865-880
- 5 Freudenberg, K.; Boppel, H.; Meyer-Delius, M. *Die Naturwissenschaften*, February **1938**, 26, 8, 123-124
- 6 Freudenberg, K. *Das Deutsche Gesundheitswesen*, **1948**, 3, 13, 400
- 7 Freudenberg, K. *Die Naturwissenschaften*, December **1939**, 27, 51, 850-853
- 8 Cramer, F.B. *Journal of the Franklin Institute*, January **1954**, 257, 1, 69–70
- 9 French, D.; Pulley, O.; Effenberger M., *Arch. Biochem. Biophys*, **1965**, 111, 153-160
- 10 Pulley, O.; French, D., *Biochemical and Biophysical Research communications*, 15 May **1961**, 5, 1, 11-15
- 11 Miyazawa, H.; Ueda, H.; Nagase, T.; Endo, T.; Kobayashi, S.; Nagai, T.; *Eur. J. Pharm. Sci.* **1995**, 3, 153–162
- 12 French, D. *Advances in Carbohydrate Chemistry*, **1957**, 12, C, 189-260
- 13 Oláh, J.; Cserháti, T.; Szejtli, J. *Water Research*, November **1988**, 22, 11, 1345-1351
- 14 Komiyama M.; Bender M. L., *J. Am. Chem. Soc.*, **1978**, 99, 2259
- 15 Sicard P. J.; Saniez M. H. *Cyclodextrins and their Industrial Uses* (Paris), **1987**
- 16 Loftsson, T.; Siguroardottir, A.M.; Frioriksdottir, H. *Proceedings of the Controlled Release Society*, **1996**, 23, 194-195
- 17 Larsen, K.L. *J. Incl. Phenom. Mol.*, **2002**, 43, 1-13.
- 18 Harata K.; Akasaka H.; Endo T.; Nagase H.; Ueda H. *Chem. Commun.*, 2002, 1968-1969
- 19 Loftsson T.; Ólafsdóttir B.J.; Friðriksdóttir H., *Eur. J. Pharm. Sci.*, **1993**, 1, 95-101
- 20 Casu, B.; Gallo, G. G.; Reggiani, M.; Vigevani A. *Stærke*, **1968**, 20, 387.
- 21 Casu B., *Chim. Ind. (Milan)* **1966**, 48, 921.
- 22 Szejtli, J.; Osa, T., Eds., *Comprehensive Supramolecular Chemistry*, Pergamon Elsevier (Oxford), **1996**, 3.



- 23 Tee, O. S.; Hoeven, J. J. *J. Am. Chem. Soc.*, **1989**, 111, 8318.
- 24 Tee, O. S. *Adv. Phys. Org. Chem.*, **1994**, 29, 1.
- 25 Demarco, P. V.; Thakkar, A. L. *J. Chem. Soc. D.* **1970**, 2.
- 26 Bender, M. L.; Komiyama, M. *Cyclodextrin Chemistry*; Springer (Berlin), **1978**.
- 27 Komiyama, M.; Bender, M. L. In *The Chemistry of Enzyme Action*; Page, M. J., Ed.; *Elsevier*: (Amsterdam), **1984**, 505
- 28 Demarco, P. V.; Thakkar, A. L. *J. Chem. Soc., Chem. Commun.*, **1970**, 2.
- 29 Duchene, D.; Ed. *New trends in cyclodextrins and derivatives*; Editions de Sante: Paris **1991**, 179 - 215
- 30 Martin, G.; Zetzker, A. S. *Two-Dimensional NMR Methods for Establishing Molecular Connectivity*; VCH: New York, **1988**.
- 31 Croasmun, W. R.; Carlson, R. M. K. *Two-Dimensional NMR Methods for Establishing Molecular Connectivity*; Eds. VCH: New York, **1994**.
- 32 Wood, D. J.; Hruska, F. E.; Saenger, W. J. *Am. Chem. Soc.*, **1977**, 99, 1735.
- 33 See Gagnaire, D.; Horton, D.; Taravel, F. R. *Carbohydr. Res.*, **1973**, 27, 363.
- 34 Casu, B.; Reggioni, M.; Gallo, G. G.; Vigevani, A. *Tetrahedron*, **1966**, 22, 3061.
- 35 Szejtli, J. In *Comprehensive Supramolecular Chemistry*; Szejtli, J., Osa, T., Eds.; *Pergamon Elsevier* (Oxford), **1996**, 3.
- 36 Vincedom, M. *Bull. Chem. Soc. Fr.* 1981, II, 129.
- 37 Casu, B.; Reggioni, M.; Gallo, G. G.; Vigevani, A. *Chem. Soc. (London)* 1968, Spec. Publ. No. 23, 217
- 38 Onda, M.; Yamamoto, Y.; Inoue, Y.; Chujo, R. *Bull. Chem. Soc. Jpn.* **1988**, 61, 4015.
- 39 Harata, K. *Bull. Chem. Soc. Jpn.* **1987**, 60, 2363.
- 40 Fraser, R. R.; Kaufman, M.; Morand, P.; Govil, G. *Can. J. Chem.* **1969**, 47, 403. For a parametrization specifically adapted to carbohydrates, see: Durette, P. L.; Horton, D. *Magn. Reson. Chem.* **1971**, 3, 417.
- 41 Botsi, A.; Yannakopoulou, K.; Hadjoudis, E.; Perly, B. *Magn. Reson. Chem.* **1996**, 34, 419.

## Bibliography – Chapter 3

- 1 Mele, A.; Castiglione F.; Malpezzi, L.; Ganazzoli, F.; Raffaini, G.; Trotta, F.; Rossi, B.; Fontana, A.; Giunchi, G. *J. Inclusion Phenom. Macrocyclic Chem.*, **2011**, 69, 403.
- 2 Castiglione, F.; Crupi, V.; Majolino, D.; Mele, A.; Rossi, B.; Trotta, F.; Venuti, V. *J. Raman Spectrosc.*, **2013**, 44 (10), 1463
- 3 K. Pal, K.; Banthia, K.; Majumdar, K. *Des. Monomers Polym.*, **2009**, 12, 197.
- 4 Langer, R.; Tirrell, D. A. *Nature*, **2004**, 428, 487.
- 5 Kloxin, A.M.; Kasko A. K.; Salinas, C.N.; Anseth, K.S. *Science*, **2009**, 324, 59.
- 6 Castiglione, F.; Crupi, V.; Majolino, D.; Mele, A.; Panzeri, W.; Rossi, B.; Trotta, F.; Venuti, V. *J. Inclusion Phenom. Macrocyclic Chem.*, **2013**, 75(3), 247.
- 7 Castiglione, F.; Crupi, V.; Majolino, D.; Mele, A.; Rossi, B.; Trotta, F.; Venuti, V. *J. Phys. Chem. B*, **2012**, 116(27),7952.
- 8 Hamley, W. *Introduction to Soft Matter*, Wiley & Sons, **2007**.
- 9 Whitesides, G.M.; Grzybowski, B.A. *Science*, **2002**, 295,2418.
- 10 Sakurada, K.; McDonald F.M.; Shimada, F. *Angew. Chem., Int. Ed.*, **2008**, 47, 5718.
- 11 Atala, A.; Lanza, R.P.; Thomson J.A.; Nerem, R.M. *Principles of regenerative medicine*, Academic Press,Burlington, MA, **2008**
- 12 B. V. Slaughter, S. S. Khurshid, O. Z. Fisher, A. Khademhosseini, N. A. Peppas, *Adv. Mater.*, **2009**, 21, 3307.
- 13 Castiglione, F.; Crupi, V.; Majolino, D.; Mele, A.; Rossi, B.; Trotta, F.; Venuti, V. *J. Phys. Chem. B*, **2012**, 116(43) ,13133.
- 14 Rossi, B.; Caponi, S.; Castiglione, F.; Corezzi, S.; Fontana, A.; Giarola, M.; Mariotto, G.; Mele, A.; Petrillo, C.; Trotta F.; Viliani, G. *J. Phys. Chem. B*, **2012**, 116 (17) , 5323.
- 15 Crupi, V.; Fontana, A.; Giarola, M.; Majolino, D.; Mariotto, G.; Mele, A.; Melone, L.; Punta, C.; Rossi, B.; Trotta F.; Venuti, V. *J. Raman Spectrosc.*, **2013**
- 16 Crupi, V.; Majolino, D.; Mele, A.; Rossi, B.; Trotta F.; Venuti, V. *Soft Matter*, **2013**, 9, 6457
- 17 Rubinstein, M.; Colby, R.H. *Polymer Physics*, Oxford University Press Inc., New York, **2003**.
- 18 Zaccarelli, E. *J. Phys.: Condens. Matter*, **2007**, 19, 323101.

- 19 Liang, W.; Yang, C.; Zhou, ; Haneoka, H.; Nishijima, M.; Fukuhara, G.; Mori, T.; Castiglione, F.; Mele, A.; Caldera, F.; Trotta F.; Inoue, Y. *Chem. Commun.*, **2013**, 49, 3510.
- 20 Trotta, F.; Tumiatti, W. *Cross-linked polymers based on cyclodextrin for removing polluting agents*; Patent **2003**, WO 03/085002.
- 21 Trotta, F.; Tumiatti, V.; Cavalli, R.; Rogero, C.; Mognetti B.; Berta, G. *Cyclodextrin-based nanosponges as a vehicle for antitumoral drugs*, **2009**, WO 09/003656 A1.
- 22 Crupi, V.; Longo, F.; Majolino D.; V. Venuti, V. *J. Phys.: Condens. Matt.*, **2006**, 18, 3563.
- 23 Kloxin, A.M.; Kasko, A. K.; Salinas, C.N.; Anseth, K.S. *Science*, **2009**, 324, 59.
- 24 Eaves, J.D.; Loparo, J.J.; Fecko, J.C.; Roberts, S.T.; Tokmakoff A.; Geissler, P.L. *Proc. Natl. Acad. Sci. U.S.A.*, **2005**, 102, 13019.
- 25 Schofield, D.P.; Lane J.R.; Kjaergaard, H.G. *J. Phys.Chem. A*, **2007**, 111, 567.
- 26 N. Goldman, N.; Saykally, R.J. *J. Chem. Phys.*, **2004**, 120, 4777.
- 27 Mallamace, F.; Broccio, M.; Corsaro, C.; Faraone, A.; Majolino, D.; Venuti, V.; Liu, L.; Mou C.Y.; Chen, S.H. *Proc. Natl. Acad. Sci. U.S.A.*, **2007**, 104, 424.
- 28 Brubach, J.B.; Mermet, A.; Filabozzi, A.; Gerschel, A.; Lairez D.; Krafft M.P. *J. Phys. Chem. B*, **2001**, 105, 430.
- 29 Stancanelli, R.; Ficarra, R.; Cannavà, C.; Guardo, M.; Calabrò, M.L.; Ficarra, P.; Ottanà, R.; Maccari, R.; Crupi, V.; Majolino D.; Venuti, V. *J. Pharm. Biomed. Anal.*, **2008**, 47, 704.
- 30 Bratu, I.; Veiga, F.; Fernandes, C.; Hernanz A.; Gavira, J.M. *Spectroscopy*, **2004**, 18, 459.
- 31 Crupi, V.; Interdonato, S.; Longo, F.; Majolino, D.; Migliardo P.; Venuti, V. *J. Raman Spectrosc.*, **2008**, 39, 244.
- 32 Giguère, P.A. *J. Chem. Phys.*, **1987**, 87, 4835.
- 33 Møller, K.B.; Rey R.; Hynes, J.T. *J. Phys. Chem. A*, **2004**, 108, 1275.
- 34 Lawrence, C.P.; Skinner, J. L. *Chem. Phys. Lett.*, **2003**, 369, 472.
- 35 Crupi, V.; Longo, F.; Majolino D.; Venuti, V. *Eur. Phys. J. 35 Special Topics*, **2007**, 141, 61.
- 36 Kob, W.; Binder, K. *Glassy Materials and Disordered Solids: An Introduction*, World Scientific, London, **2011**.
- 37 Benassi, P.; Fontana, A.; Frizzera, W.; Montagna, M.; Mazzacurati, V.; Signorelli, G. *Philos. Mag. B*, **1995**, 71, 761.
- 38 Sokolov, A.P.; Quitmann, D.; Duval, E.; *Phys. Rev. B*, **1993**, 48, 7692.
- 39 Fabiani, E.; Fontana, A.; Buchenau, U. *J. Chem. Phys.*, **2008**, 128, 244507.
- 40 Shuker, R.; Gammon, R.W. *Phys. Rev. Lett.* **1970**, 25, 222.

- 41 Niss, K.; Begen, B.; Frick, B.; Ollivier, J.; Beraud, A.; Sokolov, A.; Novikov, V.N.; Alba-Simionesco, C. *Phys. Rev. Lett.* **2007**, 99, 1.
- 42 Hong, L.; Begen, B.; Kisliuk, A.; Alba-Simionesco, C.; Novikov, V.N.; Sokolov, A.P. *Phys. Rev. B*, **2008**, 78, 134201.
- 43 Hong, L.; Gujrati, P.D.; Novikov, V.N.; Sokolov, A.P. *J. Chem. Phys.*, **2009**, 131, 1.
- 44 Zanatta, M.; Baldi, G.; Caponi, S.; Fontana, A.; Gilioli, E.; Krish, M.; Masciovecchio, C.; Monaco, G.; Orsingher, L.; Rossi, F.; Ruocco, G.; Verbeni, R. *Phys. Rev. B*, **2010**, 81, 212201.
- 45 Crupi, V.; Fontana, A.; Giarola, M.; Guella, G.; Majolino, D.; Mancini, I.; Mariotto, G.; Paciaroni, A.; Rossi, B.; Venuti, V. *J. Phys. Chem. B*, **2013**, 117, 3917.
- 46 Pilla, O.; Angelani, L.; Fontana, A.; Gonçalves, J.R.; Ruocco, G. *J. Phys. Condens. Matter*, **2003**, 15, S995.
- 47 Monaco, A.; Chumakov, A.I.; Monaco, G.; Crichton, W.A.; Meyer, A.; Comez, L.; Fioretto, D.; Korecki, J.; Ruffer, R.; *Phys. Rev. Lett.*, **2006**, 97, 135501.
- 48 Orsingher, L.; Fontana, A.; Gilioli, E.; Carini Jr., G.; Carini, G.; Tripodo, G.; Unruh, T.; Buchenau, U. *J. Chem. Phys.*, **2010**, 132, 124508.

## Bibliography - Chapter 4

- 1 Wilcox, C.S. *Pharmacology and Therapeutics* **2010**, 126, 2, Pages 119-145
- 2 Ikeda, Y.; Suzuki, R.; Yoshitomi, T.; Nagasaki, Y. *Macromolecular Bioscience* **2011**, 11, 3, 344–351, 2011]
- 3 Yoshitomi, T.; Hirayama, A.; Nagasaki, Y. *Biomaterials* **2011**, 32, 31, 8021-8028
- 4 Barriga, S. 2,2,6,6-Tetramethylpiperidine-1-oxyl (TEMPO) *Synlett* (4) **2011**, 563
- 5 Lebedev, O.L.; Kazarnovskii, S. N. Zhur. *Obshch. Khim.* **1960**, 30(5), 1631-1635.
- 6 Zanooco, A. L.; Canetem., A. Y.; Melendez, M. X. *Bol. Soc. Chil. Quím.* **2000**, 45, 123–129
- 7 Galli, C. "Nitroxyl radicals" in *Chemistry of Hydroxylamines, Oximes and Hydroxamic Acids* part. 2, John Wiley & Sons, Chichester 2009, 705-750.
- 8 Bauld, N. L. *Radicals. Ion Radicals, and Triplets: The Spin-Bearing Intermediates of Organic Chemistry* 1997, Wiley-VCH, Germany
- 9 Namazian, M.; Almodarresieh, H.A. *J. Mol. Struct.:THEOCHEM*, **2004**, 686, 97.
- 10 Alizadeh, K.; Shamsipur, M.J. *J. Mol. Struct.: THEOCHEM*, **2008**, 862, 39.
- 11 Nakahara, K.; Iwasa, S.; Satoh, M.; Morioka, Y.; Iriyama, J.; Suguro M.; Hasegawa, E. *Chem. Phys. Lett.*, **2002**, 359, 351.
- 12 Nakahara, K.; Iriyama, J.; Iwasa, S.; Suguro, M.; Satoh M.; Cairns, E.J. *J. Power Sources*, **2007**, 165, 398.
- 13 Oyaizu K.; Nishide H. *Adv. Mater.*, **2009**, 21, 2339.
- 14 G. Cittadini, G. *Diagnostica per immagini e radioterapia*, IV edizione, Genova, Edizioni culturali internazionali, **2002**
- 15 Quaia, E.; *Mezzi di contrasto in ecografia: applicazioni addominali*, Springer, **2007**
- 16 Matsumoto K.; Hyodo, F.; Matsumoto A.; Koretsky, A.P., Sowers A.L., Mitchell J.B. *Clin Cancer Res* **2006**, 12, 2445–62.
- 17 Hyodo, F.; Matsumoto, K.; Matsumoto, A.; Mitchell, J.B.; Krishna, M.C. *Cancer Res* **2006**, 66, 9921–8.
- 18 Sano, H.; Naruse, M.; Matsumoto, K.; Oi, T.; Utsumi, H. *Free Radic. Biol. Med.* **2000**, 28, 959–69.

- 19 Zhelev, Z.; Bakalova, R.; Aoki, I.; Matsumoto, K.; Gadjeva, V.; Anzai K.; Kanno I. *Chem. Commun.*, **2009**, 53-55
- 20 Taphoorn, M.J.B.; Van den Bent, M.J.; Mauer, M.E.L.; Coens, C.; Delattre, J-Y.; Brandes, A.A.; Smitt, P.A.E.; Besrnsen, H.J.J.A.; Frenay, M.; Tijssen, C.C.; Lacombe, D.; Allgeier A.; Bottomley, A. J. *Clin. Oncol.*, **2007**, 25, 5723.
- 21 N. Bodor N.; Buchwald P.; *Adv. Drug Delivery Rev.*, **1999**, 36, 229.
- 22 Zheleva A.M.; Gadjeva, V.G. *Int. J. Pharm.*, **2001**, 212, 257.
- 23 Gadjeva, V. *Eur. J. Med. Chem.*, **2002**, 37, 295.
- 24 Hyodo, F.; Matsumoto, S.; Devasahayam, N.; Dharmaraj, C.; Subramanian, S.; Mitchell, J. B.; Krishna, M.C. *Journal of Magnetic Resonance*, **2009**, 197, 181–185
- 25 Matsumoto, K.I.; Yakumaru, H.; Michiko Narazaki, M.; Hidehiko Nakagawad, H.; Anzai, K.; Ikehira, H.; Ikota, N. *Magnetic Resonance Imaging*, **2008**, 26, 117–121
- 26 Nakano, H.; Nakajima, A.H.; Sakon-Komazawa, S.; Piao, J.H.; Okumura, K. *Cell Death and Diff.* **2006**, 13, 730-737.
- 27 Verbon, E.H.; Post, J.A.; Boonstra, J. *Gene*, **2012**, 511, 1, 1-6
- 28 Garber, A.J. *Heart Failure Clinics*, **2012**, 8, 563-573
- 29 Benfeito, S.; Oliveira, C.; Soares, P.; Fernandes, C.; Silva, T.; Teixeira, J.; Borges, F. *Mitochondrion*, **2013**, 13, 5, 427-435
- 30 Samim, M.; Abdin, M.Z. ;Ahmed, F.J.; Maitra, A.N.; Prashant, C.K.; Dinda, A.K. *International Journal of Nanomedicine*, **2010**, 5 (1), 983-989
- 31 Hyodo, F.; Matsumoto, K. *Free Radical Biol. Med.* **2007**, 42, 1632–1650